Chapter 13

Mars Exploration Rover Pancam Multispectral Imaging of Rocks, Soils, and Dust at Gusev Crater and Meridiani Planum

J.F. Bell III, W.M. Calvin, W. Farrand, R. Greeley, J.R. Johnson, B. Jolliff, R.V. Morris, R.J. Sullivan, S. Thompson, A. Wang, C. Weitz & S.W. Squyres

Multispectral imaging from the Panoramic Camera (Pancam) instruments on the Mars Exploration Rovers Spirit and Opportunity has provided important new insights about the geology and geologic history of the rover landing sites and traverse locations in Gusev crater and Meridiani Planum. Pancam observations from near-UV to near-IR wavelengths provide limited compositional and mineralogic constraints on the presence abundance, and physical properties of ferric- and ferrous-iron bearing minerals in rocks, soils, and dust at both sites. High resolution and stereo morphologic observations have also helped to infer some aspects of the composition of these materials at both sites. Perhaps most importantly, Pancam observations were often efficiently and effectively used to discover and select the relatively small number of places where *in situ* measurements were performed by the rover instruments, thus supporting and enabling the much more quantitative mineralogic discoveries made using elemental chemistry and mineralogy data. This chapter summarizes the major compositionally- and mineralogically-relevant results at Gusev and Meridiani derived from Pancam observations. Classes of materials encountered in Gusev crater include outcrop rocks, float rocks, cobbles, clasts, soils, dust, rock grindings, rock coatings, windblown drift deposits, and exhumed whitish/yellowish salty soils. Materials studied in Meridiani Planum include sedimentary outcrop rocks, rock rinds, fracture fills, hematite spherules, cobbles, rock fragments, meteorites, soils, and windblown drift deposits. This chapter also previews the results of a number of coordinated observations between Pancam and other rover-based and Mars-orbital instruments that were designed to provide complementary new information and constraints on the mineralogy and physical properties of martian surface materials.

13.1. Introduction

Multispectral imaging has been an important remote sensing tool in Earth and planetary sciences for decades because of its ability to provide basic, essential information on geologic and/or atmospheric properties as well as its ability to provide secondary compositional or textural information that guides *in situ* analyses. Partly for this reason, multispectral imaging has been a key component of the scientific payloads of all five successful Mars surface lander/rover missions conducted to date. The cameras on the two Viking Landers (VL1: 1976-1982; VL2: 1976-1980; Huck *et al.,* 1975; Patterson *et al.,* 1977) acquired more than 1400 images of the detailed geomorphology, color, and photometric properties of surface soils and rocks and atmospheric aerosols, providing new information about the surface and atmosphere at the two landing sites (*e.g.,* Mutch *et al.,* 1976; Pollack *et al.,* 1979; Carr, 1981; Sharp and Malin, 1984; Adams *et al.,* 1986; Arvidson *et al.,* 1989; Christensen and Moore, 1992). The Imager for Mars Pathfinder (IMP) multispectral camera (Smith *et al.,* 1997a) on the Mars Pathfinder lander collected more than 16,000 CCD images of its landing site in Ares Valles. Like Viking,

Pathfinder acquired important new information on the nature of the martian surface via a combination of lander and rover imaging and other *in situ* elemental and meteorological measurements (*e.g.,* Smith *et al.,* 1997b; Golombek *et al.,* 1999). Much more information on the compositional and mineralogic implications of IMP multispectral imaging is discussed in Chapter 12 (Farrand *et al.*, 2007).

The most recent set of multispectral observations of the martian surface were obtained by the Panoramic Camera (Pancam) investigations on the Mars Exploration Rovers (MERs) Spirit at Gussev crater and Opportunity at Meridiani Planum. Pancam on each rover is a multispectral, panoramic, stereoscopic pair of 1024x1024 pixel CCD cameras separated by 30 cm and mounted on the rover mast 1.5 meters above the surface. Multispectral images are acquired through a rotating set of narrowband filters placed in front of the optics. Thirteen of the sixteen total filters between the two cameras were used to obtain images at eleven unique "geology" wavelengths between 430 and 1009 nm (Table 13.1). The other three filters provided the capabilities for broadband and direct solar imaging. Three of the "geology" wavelengths were chosen to be close to the peak red, green, and blue responses of the human color vision system, so that "true color" images of martian scenery could be generated (*e.g.,* Maki *et al.*, 1999; Bell *et al.,* 2006a). The other filters for Pancam were chosen to be sensitive to absorption features and the degree of crystallinity of several kinds of iron-bearing silicates and iron oxides/oxyhydroxides, and to be close to the filters used on the Pathfinder/IMP camera. Iron-bearing minerals had been known to be important components of the martian surface based on telescopic and spacecraft remote sensing studies (see, for example, reviews in Soderblom, 1992; Roush *et al.,* 1993; Bell, 1996; Morris *et al.*, 1985; 2000), and so Pancam filters were selected to sample the shape of the near-UV to visible ferric (Fe^{3+}) mineral absorption edge from ~440 to 750 nm, diagnostic crystalline ferric oxide absorption features centered near 650 nm and 860-900 nm (*e.g.,* Sherman *et al.,* 1982; Morris *et al.*, 1985), and the short wavelength wing of the "1 micron" absorption band in ferrous (Fe^{2+}) silicates like pyroxene and olivine (*e.g.,* Adams, 1974; Cloutis *et al.,* 1986). Finally, left and right pairs of identical red and blue filters provide multispectral stereo imaging capability, with the red pair optimized for stereo imaging Mars scenes with large albedo contrasts, and the blue pair optimized for scenes where topography and texture provide a larger source of scene contrast.

Table 13.1. Pancam Filter Characteristics

Name	λ_{eff}[a] (nm)	Bandpass (nm)	Comment
Left Camera			
L1	739	338	EMPTY
L2	753	20	Red Stereo L
L3	673	16	Geology
L4	601	17	Geology
L5	535	20	Geology
L6	482	30	Geology
L7	432	32	Blue Stereo L
L8	440	20	Solar ND5
Right Camera			

R1	436	37	Blue Stereo R
R2	754	20	Red Stereo R
R3	803	20	Geology
R4	864	17	Geology
R5	904	26	Geology
R6	934	25	Geology
R7	1009	38	Geology
R8	880	20	Solar ND5

[a]*Effective wavelength of the band center, assuming sunlight is the source of the illumination.*

Pancam represents an important advance in the progression of Mars surface imaging investigations, as it possesses excellent multispectral and dynamic range capabilities similar to those of the Pathfinder/IMP camera, and roughly three times better spatial resolution compared to Pathfinder and Viking Lander cameras. Pancam was in fact designed so that it would directly help to fulfill the overall MER mission objectives of exploring two sites on the martian surface where water may once have been present, and to assess past environmental conditions at those sites and their suitability for life (*e.g.,* Squyres *et al.,* 2003). Key Pancam investigation goals in support of these mission objectives included: (1) assessing the high resolution morphology, topography, and geologic context of each MER landing site; (2) obtaining color images to constrain the mineralogic, photometric, and physical properties of surface materials; and (3) determining dust and aerosol opacity and physical properties from direct imaging of the Sun and sky. In addition to directly addressing science goals of the MER mission, the Pancam investigation also provided supporting geology/albedo/color context measurements for Mini-TES infrared spectroscopy (see, *e.g.,* Chapter 14 by Ruff *et al.*) and chemical, mineralogic, and Microscopic Imager (MI) measurements acquired by the *in situ* instruments on the rover's arm (see, *e.g.,* Chapter 4 by Brückner *et al.*; Chapter 15 by Morris and Klingelhöfer; and Chapter 20 by Herkenhoff *et al.*). A much more detailed description of the objectives, design, testing, calibration, and pre-flight performance of the MER Pancams can be found in Bell *et al.* (2003), and details on the calibration and in-flight performance of the cameras on Mars can be found in Bell *et al.* (2006b).

The multispectral properties of the martian surface are influenced by a wide variety of factors, including the composition and mineralogy of rocks and soils as well as their physical properties (surface textures, grain sizes, presence and nature of coatings, etc.). In this chapter we describe some of the major martian surface multispectral and morphologic findings with relevance to composition and mineralogy that were obtained from MER/Pancam observations at both Gusev crater and Meridiani Planum. Discussed here are the visible to near-IR (440 to 1009 nm) spectral properties of dust, bright and dark soils, spherules, rocky cobbles and clasts, and whole rock surfaces (natural, as well as brushed and abraded by the Rock Abrasion Tool or RAT). We discuss the Pancam remote sensing findings in the broader context of surface and orbital remote sensing and *in situ* measurements of martian surface materials presented in detail in many of the other chapters in this book. While some Pancam results relevant to surface physical properties are described here, significantly more detail on that topic can be found in Chapter 19 by Johnson *et al.* and Chapter 20 by Herkenhoff *et al.*

13.2. Multispectral and morphologic properties of surface aterials at Gusev Crater

13.2.1. Overview

As of *Spirit's* martian day (sol) 810 (April 14, 2006), the rover had traversed roughly 6876 meters (odometry based on wheel turns) from her initial landing site (Figure 13.1). The traverse began in the Gusev cratered plains and included a visit to the rim and ejecta blanket of Bonneville crater, a ~3 km drive across the basaltic plains to the base of the Columbia Hills, a winter ascent of the West Spur and northwestern slopes of ~100 m high Husband Hill and a summertime descent down the southeast slope into the Southern Basin, leading finally to the exploration of a layered, roughly circular, 80-m wide feature known as Home Plate not far from the basin's topographic low point. Details about much of this traverse and its geologic goals can be found in Squyres *et al.* (2004a) and Arvidson *et al.* (2006a). Starting in April 2006, *Spirit* spent most of the rest of the year parked on a small ridge near Home Plate with her solar panels tilted towards the north in order to get enough solar power to survive her second martian winter. As of this writing (mission sol 1053), *Spirit* has survived the winter and is beginning to explore in more detail new science targets in the vicinity of Home Plate.

Here we describe the major classes of rocks, clasts, soils, and windblown drift deposits that were characterized by the Pancams along the Gusev crater traverse. Multispectral imaging can provide constraints on the composition and mineralogy of these materials that can be used to enhance, augment, or provide context for more diagnostic Mini-TES or *in situ* measurements of the composition and mineralogy. In some cases, though, even just monochromatic imaging at high resolution can provide constraints on the composition and origin of materials encountered, based on the geomorphology alone.

13.2.2. Outcrop rocks, float rocks, cobbles, and clasts

13.2.2.1. Geomorphology

A number of detailed studies of the geology and geomorphology of rocks and rocky materials the Gusev cratered plains and the Columbia Hills have been published (*e.g.,* Grant *et al.,* 2004; Squyres *et al.,* 2004a, 2006a; Crumpler *et al.,* 2005; Arvidson *et al.,* 2006a; Golombek *et al.,* 2006). While the details of the geology of the landing site presented in those papers are beyond the scope of this chapter, several kinds of morphologic features and properties have been observed during *Spirit's* traverse that can help to provide constraints on the composition and physical properties of Gusev crater rocky materials (Figure 13.2).

For example, many of the "float" rocks and clasts (pieces of rock that have been separated from their parent vein, strata, or outcrop by impact or weathering processes) observed in the Gusev plains were observed to be extremely hard, based on the high specific energies needed to grind into them with the RAT (Arvidson *et al.,* 2004). Their hardness, often angular to subangular appearance, and microscopic-scale textures (*e.g.,* Herkenhoff *et al.,* 2004; See also Chapter 20 by Herkenhoff *et al.*) are all consistent with their identification as basaltic lava rocks, an inference confirmed by detailed *in situ* chemical and mineralogic measurements made on many of these rocks (See Chapter 4 by Brückner *et al.* and Chapter 15 by Morris and Klingelhöfer for details). The relatively small number of rounded rocks observed on the plains

and elsewhere in Gusev crater are generally darker and display signs of wind erosion rather than any unambiguous indications of a fluvial origin.

Another example of a morphologic indicator of composition is the identification of what appeared to be much softer, more friable, and platy or layered rocks (*e.g.,* Bell *et al.,* 2004a; Arvidson *et al.,* 2006a). The first of these were seen in the West Spur of Husband Hill, where many rocks were found to be softer based on RAT grinding energies. Chemical and mineralogical measurements on some of these kinds of rocks subsequently showed an increased ferric to ferrous iron ratio, implying more altered compositions. Indeed, both hematite (□-Fe_2O_3) and goethite (□-FeOOH) were identified in some rocks, suggesting significant water-related alteration of parent basaltic compositions (*e.g.,* Morris *et al.,* 2006a; see also Chapter 23 by Ming *et al.*).

A final example of morphology providing compositional clues for Gusev rocks is the identification of some rocks that appear pitted or vesicular (*e.g.,* Bell *et al.,* 2004a; McSween *et al.,* 2004; Golombek *et al.,* 2006; see Figures 13.2e, 13.2g). The observed morphology of many of these rocks is consistent with outgassing of volatile-rich lavas (*e.g.,* Crumpler *et al.,* 2007), most likely with some expansion of the pits and vesicles by subsequent aeolian erosion. These rocks are dark (except where covered by airfall dust) and have a relatively low ratio of ferric iron to total iron (Fe^{3+}/Fe_T), suggesting little chemical alteration since their eruption/emplacement (Morris *et al.,* 2006a). Two of these pitted rocks, Allan Hills and Zhong Shan near Home Plate, appeared somewhat more rounded than typical; based on their distinctive Mini-TES spectra features they have been interpreted as possible meteorites (see Ruff (2007) and Chapter 14 for more details).

13.2.2.2. Multispectral Properties

Several distinct spectral classes of rocks have been identified from Pancam observations during *Spirit's* traverse. These spectral classes generally correspond to those defined from APXS measured elemental chemistry (*e.g.,* Gellert *et al.,* 2004; Squyres *et al.*, 2006a). There are more spectral classes than there are chemical classes, however, because some of the mineralogic variations (which Pancam is sensitive to) are apparently isochemical (see Chapter 23 by Ming *et al.*, Chapter 15 by Morris and Klingelhöfer, and Morris *et al.,* 2006a). For example, in some instances iron-bearing minerals have apparently changed from Fe^{2+}-bearing silicates like olivine and pyroxene to Fe^{3+}-bearing oxides and oxyhydroxides via weathering processes.

Farrand *et al.* (2006) made use of spectral mixture analysis techniques to identify the most spectrally "pure" rock surfaces; *i.e.,* those having the least contamination by dust. The spectral variability of the scenes that were examined was modeled as linear combinations of so-called endmember pixels (typically "rock", "soil", and "shade") chosen directly from the images (*e.g.,* Adams *et al.,* 1986). These simple 3-endmember models were valid for the vast majority of scenes imaged during *Spirit's* traverse across the Gusev crater plains. In the Columbia Hills, lithologic diversity was greater and some scenes were found to contain more than one rock endmember or more than one soil endmember. Figure 13.3 is an example Gusev crater scene showing distinct Pancam spectral classes.

The rock classes identified by Farrand *et al.* (2006) through Spirit sol 419 were: (1) Gusev plains basalts (equivalent to the Adirondack class of Squyres *et al.*, 2006a); (2) Lower West Spur rocks (exemplified by the rocks "Pot of Gold" and "Wooly Patch"); (3) West Spur or Clovis class; (4) Wishstone class; (5) Peace class; and (6) Watchtower class. Figure 13.4a shows representative spectra of these 6 spectral classes (Farrand *et al.*, 2006). These classes were defined on the basis of a set of spectral parameters, most notably the 535 nm band depth (the ratio of the reflectance at 535 nm to the "continuum" reflectance at nearby wavelengths; Clark and Roush, 1984) , the 904 nm band depth, the 803/904 nm ratio, the 754 to 864 spectral slope, and the 754 to 1009 nm spectral slope. The first of these parameters is a measure of the degree of oxidation and crystallinity of the iron-bearing minerals on the surface; the others are measures of the relative abundance of crystalline ferrous silicate and/or ferric oxide phases (*e.g.,* Morris *et al.,* 2000; Bell *et al.,* 2000; Farrand *et al.,* 2006).

Additional Pancam-based spectral classes of rocks have been identified since the initial study by Farrand *et al.* (2006). These new classes correspond to the Larry's Outcrop, Jibsheet, and Methuselah outcrop rocks near the summit of Husband Hill, to the olivine-rich "Algonquin class" rocks (*e.g.,* see Chapter 14 by Ruff *et al.*), which were observed at several outcrops on the eastern slopes of Husband Hill, and one or more classes associated with the circular "Home Plate" feature on the floor of the basin south of Husband Hill. Figure 13.4.b shows representative spectra of some of these more recent, distinctive spectral classes.

Rocks such as Watchtower are interpreted as being highly altered. They have positive 754 to 1009 nm ratios and significant 535 nm band depths. As seen in Figure 13.5, the 535 nm band depth correlates with high Fe^{3+}/Fe_T ratios as measured by *Spirit's* Mössbauer spectrometer (*e.g.,* Farrand *et al.,* 2006; Morris *et al.,* 2006a; Chapter 15 by Morris and Klingelhöfer). Apparently less altered rocks with lower 535 nm band depths and a significant long wavelength (ferrous?) absorption feature centered near 904 to 934 nm were examined *in situ* at the Methuselah outcrop near the Husband Hill summit. Rocks at the Jibsheet outcrop have properties intermediate between those of Watchtower and Methuselah. Some rocks examined on the eastern slope of Husband Hill, exemplified in Figure 13.4b by the Larry's Bench spectrum, show a low 535 nm band depth, a comparitively short relative reflectance maximum at 673 nm, and a near-IR reflectance decrease consistent with the presence of olivine. Pancam spectra alone cannot uniquely identify olivine, but in some cases the inferred presence of olivine from Pancam spectra has been confirmed by more definitive Mini-TES and Mössbauer mineralogical detections (see, *e.g.,* Chapter 14 by Ruff *et al.* and Chapter 15 by Morris and Klingelhöfer), thus validating the inferred presence of this mineral for regions not measured by Mini-TES or the rover's *in situ* instruments.

Pancam multispectral imaging of Home Plate outcrops (13.6) demonstrate that natural rock surfaces with minimal dust coatings and RAT-brushed rock surfaces have low albedo and exhibit ~930 nm band absorptions consistent with the presence of low-calcium pyroxene or possibly ferric oxyhydroxides. Such absorptions are similar to those observed in relatively clean (or RAT-cleaned) rock surfaces on the West Spur of Husband Hill (Farrand *et al.,* 2006). The spectral similarity of Home Plate and West Spur rocks was also noted in Mini-TES thermal infrared spectral observations (deconvolution of thermal infrared spectra indicated high glass abundances in both; *e.g.,* Chapter 14 by Ruff *et al.*). In Figure 13.6, redder, dustier surfaces

gradually lose the 930 nm absorption band and display deeper 535 nm absorptions, apparently indicating the presence of nanophase and/or relatively more crystalline ferric oxides present in the dust covering or coating these rocks (*e.g.,* Bell *et al.*, 2000, 2004a; Morris *et al.*, 2000; Farrand *et al.*, 2006). Reflectance spectra of nearby vesicular, dark (minimally dusty), "float" rocks are similar to the spectra of RAT-brushed Home Plate rocks. Portions of the brushed region on the float rock Posey at the base of the Home Plate rim also exhibit the 930 nm band, although the average spectra from the entire brushed region exhibit lower reflectance at 1009 nm than the brushed regions of the Home Plate outcrops (Figure 13.6). This is potentially the result of wavelength-dependent scattering effects such as enhanced specular reflections at the illumination/viewing geometry for Posey. Spectra of higher albedo portions of the Hilton Smith outcrop located on the northeastern rim of Home Plate exhibit a downturn towards 1009 nm that also was observed from the top of Husband Hill and found to be spatially distinctive across the eastern and southern Home Plate rims. While there is insufficient information for unambiguous determination, this surface may represent a different type of coating (perhaps older and/or more indurated) than normal airfall dust.

13.2.3. Soils and windblown drift deposits

13.2.3.1. Definitions

The term "soil" has become commonly used in planetary science to describe the fine-grained, porous, uppermost layers of a regolith, despite the common terrestrial soil science viewpoint that the term applies only to material formed by or in the presence of organic compounds (*e.g.,* Johnson, 1968; Markewitz, 1997). A useful generic definition of soil is "unconsolidated mineral matter that may differ chemically, physically, morphologically, or biologically from the material from which it is derived" (Soil Science Society of America, 1984). Martian soil in particular has been described as the excited "skin" of the part of the martian crust that is in direct contact with the (current or past) atmosphere (see Nikiforoff, 1959; Retallack, 1998; Bell *et al.,* 2000), a description that we use throughout this chapter and which also includes "soil" adhering to rock surfaces. In the grain-size scale used by soil scientists [modified from the originally-defined scheme of Wentworth (1922)], clay is the size fraction less than about 2 μm, silt is about 2 to 50 μm, and sand is about 50 μm to 2 mm. For Mars, planetary scientists typically define "dust" as the finest-grained component of the soil that easily can become airborne, and this component is known to be less than about 5 μm in diameter from Viking (Pollack *et al.,* 1979), Pathfinder (Markiewicz *et al.*, 1999; Morris *et al.,* 2001) and MER (Lemmon *et al.*, 2004; Morris *et al.,* 2006) observations. For simplicity, our usage of "sand" includes the sand size fraction used by soil scientists (50 μm to 2 mm) plus the 5-50 μm medium and coarse silt size fractions. Sand and dust that appear to have been concentrated into dunes, ripples, or other bedforms on the surface by the action of wind (Greeley and Iversen, 1985) are often called "drift" or "aeolian drift" (Aeolis was the Greek god of the wind). Collectively, these definitions of "soil", "dust", "drift", and "sand" are often gathered together into the term "fine grained materials." Examples of the variety of fine-grained materials studied using Pancam in Gusev crater are shown in Figure 13.7. Regardless of the formal definition or planet of interest, soil is formed by a combination of many influences, among them parent material composition and climate, and thus the soil provides a window into the past lithologic and environmental history of a planetary surface.

13.2.3.2. Geomorphology

The current surface of Mars is modified primarily by the action of wind (see, for example, Greeley and Iversen, 1985; Greeley *et al.,* 2004; Sullivan *et al.,* 2005) . Dust is carried aloft in suspension, can be transported long distances, and thus is likely to represent a globally homogenized component of the surface composition almost everywhere. Sand is transported on or near the ground, can be trapped in craters and dunes, and thus is likely to be more indicative of local and regional compositions. Fine-grained windblown material can also become "plastered" to the surface as soil, forming a thin coating and masking the intrinsic composition of the rock (to which it may or may not have a genetic relationship).

Spirit's traverse path on the floor of Gusev crater has been imaged repeatedly from orbit, allowing changes in surface albedo patterns to be tracked (*e.g.,* Greeley *et al.*, 2004; 2005). The most common features observed are dark linear and curvilinear features that appear, disappear, or change orientations with time. Long suspected to be the "tracks" left by the passage of dust devils, observations of active dust devils from *Spirit* confirm this hypothesis (*e.g.,* Lemmon *et al.,* 2004; Arvidson *et al.,* 2006a; Greeley *et al.,* 2006a,b). Vortexes in the atmosphere are capable of lifting dust, which is typically "bright," into the atmosphere, leaving coarser grained materials on the surface, which then appear comparatively dark. *Spirit* MI images show that soils within such a "dark" streak are relatively free of dust, whereas Mi images outside the streak appear dustier, confirming this model (Greeley *et al.*, 2005, 2006a).

Bright soils occur in organized deposits, including dunes and smaller ripples, and as unorganized patches. Most of these appear to be windblown sand, composed of grains smaller than a millimeter or so (*e.g.,* Herkenhoff *et al.,* 2004). In some areas, these deposits have a "lag" layer, or an "armoring," of coarser gains as large as a few millimeters, which has been interpreted to result from the removal of smaller grains by the wind (Herkenhoff *et al.,* 2004, 2006).

Dust is observed as mantles on the tops of many rocks and is incorporated in some soil deposits. Its incorporation within some sand dunes suggests that these dunes are not currently active (*e.g.,* Greeley *et al.,* 2006a). Over the first 400 to 420 sols of *Spirit's* mission, dust appears to have settled onto the rover's solar panels and the Pancam calibration target (*e.g.,* Bell *et al.,* 2006b). However, on sols 417 and 421, a marked increase in power output from the solar panels combined with images of "wind streaks" of dust on the rover deck indicated that the first of what became several "dust-clearing events" had occurred. This time period marked the initiation of active dust devils in Gusev crater, as seen from *Spirit* (*e.g.,* Greeley *et al.*, 2006b), and further emphasized the fact that dust must be treated as an active and variable component in remote sensing observations of Mars on all spatial scales.

13.2.3.3. Multispectral properties

Typical soils and dust

Pancam 11-color spectra of a variety of typical soils and rocks are shown in Figure 13.8a (Bell *et al.,* 2004a, 2006b). These spectra sample the diversity of visible to near-IR units encountered during the early part of *Spirit's* traverse, from the landing site to the ejecta blanket of Bonneville crater (Figure 13.1); however, they are also representative of typical Pancam spectra encountered along later parts of the traverse in and beyond the Columbia Hills. For comparison, average classical bright and dark region telescopic spectra (Bell *et al.,* 1990; Mustard and Bell, 1994), and average bright and dark region spectra from Mars Pathfinder IMP

observations (Bell *et al.,* 2000; see also Chapter 12 by Farrand *et al.*) are also plotted in Figure 13.8a.

Pancam spectra of typical bright and dark soils in Gusev crater are consistent with previous average bright and dark region telescopic spectra and IMP multispectral data. Similarity in the bright soil/dust spectra observed by Pancam and remote sensing signatures of bright/dusty surfaces at much wider spatial scales is not surprising. It has been known for decades that windblown dust is a globally-homogenized, ubiquitous component of the soil everywhere on Mars, and that its visible-wavelength spectral properties are dominated by the presence of fine-grained (nanophase to poorly crystalline) ferric oxides (see, for example, reviews in Soderblom, 1992; Roush *et al.,* 1993; and Chapter 2 by Calvin and Bell). Similarities between telescopic and orbital observations of dust and surface-derived measurements of high albedo soils and drift had also been noted previously at the Viking and Mars Pathfinder landing sites (*e.g.,* Adams *et al.,* 1986; Arvidson *et al.,* 1989; Bell *et al.,* 2000; Morris *et al.,* 2000).

Observations and modeling of the reflected radiances from the Pancam calibration targets on *Spirit* and *Opportunity*, which became dust-coated with time during the mission (*e.g.,* Bell *et al.,* 2006b), have allowed Kinch *et al.* (2006) to make a direct determination of the spectrum of airfall dust. The derived dust spectrum (Figure 13.9) is comparable to telescopic and IMP spectra of bright regions, and is similar at both landing sites, further confirming the globally-mixed nature of the martian airfall dust signature. In addition, the derived airfall dust spectrum shows little evidence for the kinds of absorption features (for example, from 800 to 1000 nm) and spectral inflections (for example, near 535 nm) that would indicate the presence of crystalline ferric (or ferrous) oxides or silicates in the dust, providing further supporting for nanophase (X-ray amorphous) ferric oxides dominating the dust's spectral behavior. A model of the spectral properties of the dust, combined with knowledge of the reflectance and photometric properties of the calibration target materials, was used to remove the dust contribution from the calibration target reflectance and allow tactical-timescale calibration of Pancam images even using dusty calibration target observations (*e.g.,* Bell *et al.,* 2006; Kinch *et al.,* 2006).

Inferences about the mineralogy of the dust derived from Pancam spectra are consistent with the thermal infrared spectra of the dust derived by Bandfield *et al.* (2003) from MGS Thermal Emission Spectrometer (TES) observations (see also Chapter 9 by Christensen *et al.*), which also revealed a mineralogy that must be dominated by extremely fine-grained silicates and only small percentages of well-crystalline phases. The nanophase ferric oxides or other fine-grained silicates may just be "chromophore" phases (pigmenting, color-giving, but not volumetrically important) in the dust, however, as Mössbauer measurements of the airfall dust on the rover's Magnetic Properties Experiment surfaces and Mössbauer measurements of bright, undisturbed surface dust have revealed the presence of well-crystalline magnetite, olivine, and perhaps even pyroxene within airfall dust grains (*e.g.,* Goetz *et al.*, 2005; Morris *et al.,* 2006b; see also Chapter 16 by Madsen *et al.* and Chapter 15 by Morris and Klingelhöfer). Dust grains appear to be composite particles composed of these minerals, nanophase ferric oxides, and some as-yet uncertain percentage of nonmagnetic phases like feldspars or carbonates.

"Gray" rock grindings and "white" rock coatings

Several new spectral classes unlike those previously seen have been discovered in the Pancam data from Gusev. For example, Pancam spectra of the dust/"soil" created by grinding into Gusev plains basalts like Adirondack, Humphrey, and Mazatzal are dark and remarkably flat, and the spectra of the corresponding RAT-ground rock surface are similarly gray (Figure 13.10a; *e.g.,* McSween *et al.,* 2004, 2006a). In fact, spectra like these are the grayest spectra ever acquired on Mars, and exhibit little to no indication of the presence of ferric iron. The implication from Pancam spectra, comparing them with derived multispectral parameters versus laboratory-derived parameters at comparable wavelengths from minerals and mineral mixtures (Figure 13.10b; *e.g.,* Morris *et al.,* 2000; Cloutis and Bell, 2003) is that the plains rocks in Gusev are ferrous silicate-bearing (olivine-, pyroxene-rich) basalts that have undergone extremely little oxidation and chemical weathering. The flat spectra of these rocks may also result from the presence of opaque magnetite in these rocks. These inferences have been confirmed by more definitive *in situ* APXS and Mössbauer chemistry and mineralogy measurements of these rocks (*e.g.,* McSween *et al.,* 2004, 2006a; see also Chapter 4 by Brueckner *et al.,* Chapter 15 by Morris and Klingelhöfer, and Chapter 23 by Ming *et al.*). Similarly pristine basaltic float rocks have also been discovered and characterized by Pancam and other instruments throughout *Spirit's* traverse, including at high elevations in the Columbia Hills (*e.g.,* McSween *et al.,* 2006b; Ruff *et al.,* 2006; see also Chapter 14 by Ruff *et al.*).

Another example of a new spectral class was found in Pancam spectra of the so-called "white" (actually quite reddish) rocks seen during the traverse to Bonneville crater (*e.g.,* Bell *et al.,* 2004a; Arvidson *et al.,* 2006a). These surfaces exhibit an anomalously-high reflectivity in the blue relative to typical bright reddish soils and dunes (Figure 13.8a). These surfaces also exhibit a negative near-IR spectral slope, which is also not typical of bright Gusev materials. Combined, the high blue reflectance, negative near-IR slope, and knowledge of the dark, grayish spectrum of typical "clean" Gusev plains basalts (*e.g.,* Figure 13.10) support a model of the bright reddish rock surfaces as a thin coating of possibly cemented or duricrusted dust and/or bright soil. In this model, at the shortest wavelengths (400 to 500 nm), photons appear to be able to penetrate to and interact with the relatively pristine substrate rock, which has more than a factor of two greater reflectivity than the dust, which is extremely dark in the blue (Figure 13.8a). At green, red, and short-wave near-IR wavelengths (about 500 to 800 nm), the dust is much more reflective, and so surface scattering appears to dominate over volumetric penetration and interaction with the substrate, yielding a more "dust like" reflectance spectrum at these wavelengths. At even longer wavelengths, the dust reflectivity remains relatively constant but because it is thin, the coating becomes more transparent to longer-wavelength photons and the spectrum slopes downward towards the much lower near-IR reflectance of the relatively pristine rocky substrate. If this model is valid, the coatings must be extremely thin, probably on the order of a few to less than 10 microns, comparable to only a few times the average grain size of typical martian dust particles. These kinds of spectral effects from thin bright dust coatings over lower albedo rocky or sandy substrates on Mars have also been inferred from previous orbital and Pathfinder remote sensing observations (*e.g.,* Fischer and Pieters, 1993; Johnson *et al.,* 1999; Bell *et al.,* 2000) and have been directly observed and modeled in laboratory simulations of Mars-like dust covering/coating Mars-like basaltic rocks and other substrates (*e.g.,* Johnson and Grundy, 2001; Johnson *et al.,* 2004, 2006; Kinch *et al.,* 2006; see also Chapter 19 by Johnson *et al.*).

Whitish/yellowish salty soils

Perhaps the most exciting new spectral class of fine-grained materials discovered by *Spirit* during the traverse within Gusev crater are a set of light-toned soils encountered in three different regions when the action of the rover's wheels excavated subsurface materials (Figure 13.11). The first occurrence of these soils was on the drive toward the summit of Husband Hill near a region named Paso Robles; the second was in the basin south of the Hills at a feature named Arad; and the third was near Home Plate in a region named Tyrone. Where least contaminated by contributions from typical reddish surface soils, these materials exhibited high albedo and white to yellow hues that varied over small length scales (Figure 13.11). Observations by the APXS instrument at Paso Robles and Arad showed high sulfur contents (up to 35 wt.% SO_3), and Mössbauer measurements at the same locations suggested that the soils were dominated by Fe^{3+}-bearing sulfates (Gellert *et al.,* 2006; Morris *et al.,* 2006a; Ming *et al.,* 2006). Mini-TES measurements of sulfur-rich soils in Gusev suggested the presence of a 6 μm bound water spectral feature, consistent with the presence of hydrated minerals, particularly for the Tyrone soils (see, for example, Chapter 14 by Ruff *et al.*). Mini-TES data for Paso Robles have also been shown to be consistent with the presence of Fe^{3+}-bearing sulfates (Lane *et al.,* 2006).

The chemical and mineralogic analyses/inferences from the visibly-distinct salt-rich soils in the three Columbia Hills/southern Basin regions noted above are consistent with and an extension of the high Fe^{3+}, Mg, S, Cl, and Br detected in subsurface soils within three shallow trenches dug by *Spirit's* wheels in the volcanic plains between the landing site and the Columbia Hills (Wang *et al.*, 2006). The sulfur-rich plains trench soils do not exhibit the dramatic Pancam (or Mini-TES) color/spectral differences of the Hills/Basin sulfur-rich soils, suggesting that a larger fraction of spectrally masking "normal" dust/soil is mixed with the high-S soils in the plains trenches than at Paso Robles, Arad, and Tyrone. Still, these trench wall and floor soils exhibit distinctive *in situ* chemical/mineralogic signatures. Wang *et al.* (2006) interpret the APXS and Mössbauer measurements within these trenches to indicate the presence of primarily Mg-rich sulfates, with minor amounts of Ca- and perhaps Fe-sulfates as well. However, Morris *et al.* (2006a) do not report ferric sulfates in the trench soils from their analysis of the Mössbauer data. Perhaps S-rich subsurface soils in the Gusev plains were formed by a similar, though less efficient or less concentrated process, as the more colorful but chemically similar soils from farther along the traverse.

Pancam spectra of the Paso Robles, Arad, and Tyrone materials were some of the most spectrally diverse of all the fine-grained materials encountered by *Spirit*. All of these whitish to yellowish soils exhibited distinctive reflectance maxima near 670 nm consistent with the presence of hydrated ferric sulfates (and distinct from jarosite and hematite; *e.g.,* Morris *et al.,* 1985; Crowley *et al.,* 2003; Cloutis *et al.,* 2006). Subtle absorptions and inflections near 480 nm (Parente *et al.,* 2007) and between 800-900 nm (Johnson *et al.,* 2007; Figure 13.12) were also observed in some regions within these soils; these features are consistent with the presence of some Fe^{3+}-bearing sulfate minerals. Analysis by Lane *et al.* (2007) of combined Pancam, Mini-TES, Mössbauer, and APXS data suggests that Fe-bearing phosphates may also be contributing to the observed characteristics of these whitish/yellowish soils.

To systematically model the potential minerals contributing to the observed Pancam spectra, Johnson *et al.* (2007) used a multiple end-member spectral mixture approach (MESMA) in combination with a spectral reference library composed of laboratory spectra of sulfate minerals plus two Pancam spectra of typical Gusev soil and darker (less dusty) soil (Figure 13.11). Linear mixing models such as MESMA cannot be used to provide absolute abundances of mineral components owing to non-linear effects induced by intimate mixing (*e.g.,* Clark and Roush, 1984; Mustard and Pieters, 1987; Poulet and Erard, 2004). This is especially a problem for the excavated, mixed, light-toned soils analyzed by Johnson *et al.* (2007). Nonetheless, such models can be used to provide first-order mineral detections. Johnson *et al.* (2007) ran the MESMA algorithm for six Pancam spectra extracted from the Paso Robles, Arad, and Tyrone soils (locations shown in Figure 13.11). The modeled spectra are overlain on the Pancam spectra in Figure 13.12, and Table 13.2 lists the major minerals detected by the model as well as the RMS errors. The MESMA results consistently modeled each Pancam spectrum with a large proportion (> 50%) of "undisturbed soil". The whiteish and yellowish colored soil spectra were modeled using various ferric sulfates hydrated to different degrees and possibly even subjected to NH_4^+-rich fluids and/or gas (*e.g.,* Kasting *et al.,* 1992; Bishop *et al.,* 2002). However, the endmember spectral library used by Johnson *et al.* (2007) to model the data may be inadequate, which could possibly lead to incorrect inferences about the mineralogy of the deposits. For example, there is no evidence for hydronium jarosite in the Arad soils from Mössbauer spectroscopy of these materials. Broader, multi-instrument perspectives on these deposits (*e.g.,* Lane *et al.,* 2007) may lead to a more accurate understanding of their mineralogy and origin.

Table 13.2. MESMA model results (percent major minerals and soil). From Johnson *et al.* (2007).

Mars Sample:	Arad "White"	Arad "Yellow"	Paso Robles "Gray"	Paso Robles "White"	Tyrone "White"	Tyrone "Yellow"
Mineral or Soil						
Copiapite (SPT138) $Fe^{2+}Fe^{3+}_4(SO_4)_6(OH)_2{\cdot}20(H_2O)$	--	--	--	1	6	--
Kieserite (SPT 141) $Mg(SO_4){\cdot}(H_2O)$	--	--	7	9	--	--
Kornelite (SPT 137) $Fe^{3+}_2(SO_4)_3{\cdot}7(H_2O)$	--	--	6	--	--	--
Boussingaultite (SPT 102) $(NH_4)_2Mg(SO_4)_2 \cdot 6(H_2O)$	--	--	9	12	18	--
Fibroferrite $Fe^{3+}(SO_4)(OH){\cdot}5(H_2O)$	4	15	--	--	--	--
Hydronium jarosite (STP 120) $(H_3O)Fe^{3+}_3(SO_4)_2(OH)_6$	21	28	--	--	--	5
Rhomboclase $HFe^{3+}(SO_4)_2 \cdot 4(H_2O)$	9	5	--	--	--	--
Synthetic (SPT 104) $Fe^{3+}NH_4(SO_4)_2H_2O$	--	--	--	--	--	10
Paso Robles soil	60	51	33	--	69	81

Arad basaltic soil	--	--	37	76	--	--
Model RMS:	*0.00709*	*0.00610*	*0.00232*	*0.00323*	*0.00907*	*0.00453*

Subsurface spectral "stratigraphy"

As shown above, multispectral imaging and *in situ* chemical/mineral measurements of soils "disturbed" by the action of the rover's wheels (normal driving, scrambling up hills or down craters, or intentionally digging shallow trenches) or by the landing system's airbags can provide information on the stratigraphy of the near-surface. For example, *Spirit's* wheels typically leave dark tracks after rolling over the relatively high-albedo terrain of the Gusev crater plains (Figure 13.13). The observed drop in approximate Lambert albedo derived from Pancam broadband L1 filter observations (Bell *et al.,* 2006) is roughly a factor of two, from typical dusty plains/hills albedo values of 0.20 to 0.30 down to values of 0.10 to 0.12. Multispectral observations of wheel tracks as well as of shallow trenches dug by the rover wheels (Figure 13.14) reveal that the uppermost surface of almost all Gusev plains soils is both brighter and redder than the immediate subsurface (*e.g.,* Bell *et al.,* 2004a; Farrand *et al.,* 2006; Wang *et al.,* 2006), implying an increased ferric mineral content–presumably from a thin layer of surface dust–in the uppermost surface compared to the subsurface. This inference was confirmed by Mössbauer observations in the floors and walls of several Gusev trenches which showed significantly lower Fe^{3+}/Fe_{total} in the shallow subsurface, consistent with less altered, more "basaltic" materials underlying a thin (few millimeters) dusty uppermost surface (*e.g.,* Morris *et al.,* 2006a; Wang *et al.* 2006).

The observed change in albedo between dusty plains (0.20 to 0.30) and dust devil tracks (about 0.20; Bell *et al.,* 2004a) is significantly less than the albedo change associated with plains wheel tracks and trenches. This observation suggests that the rover wheels "scour" and mix the surface and subsurface either more efficiently or more deeply than typical dust devils. There may also be a timescale issue involved, as both dust devil tracks and rover tracks have been observed to brighten with time from the "restorative" action of continual airfall dust deposition brightening these lower albedo surfaces (*e.g.,* Sullivan *et al.,* 2005).

The rover wheels sometimes dislodged materials and significantly scoured rock and soil surfaces while climbing the Columbia Hills. In general, there is less contrast between the wheel tracks and the undisturbed soils in the Hills compared to the plains, suggesting either less dust on Hills soils and/or less efficient surface/subsurface mixing of the soils by normal wheel interactions (perhaps reflecting a harder or more indurated nature to the Hills soils compared to the plains soils). In some places, small patches of brighter, bluer, more specularly-reflecting fine-grained materials were exposed or exhumed by the action of the wheels (*e.g.,* Figure 13.15). Until arriving at Paso Robles around sol 400 (Figure 13.11), exposures of this kind of material large enough to allow APXS and Mössbauer measurements had not been encountered. These scattered exposures of "shiny soil" may be smaller concentrations of the whiteish to yellowish sulfur-rich soils described above. For some of these disturbed soils, especially those looking sunward in forward-scattering geometries, the brightness increase may be a physical effect at least partially related to increased specular scattering associated with the compaction of the soils by the rover's wheels (Figure 13.15).

13.3. Multispectral and morphologic properties of surface materials at meridiani planum

13.3.1. Overview

As of *Opportunity* sol 810 (May 5, 2006), the second MER rover had traversed roughly 7575 meters (odometry based on wheel turns) from her initial landing site (Figure 13.16). The traverse began in the small (20 m diameter) crater called Eagle, where *Opportunity* spent nearly 60 sols investigating the soils and discovering several new classes of martian surface materials, including small spherules and outcrops of finely-laminated sulfur-rich sedimentary rocks. The rover then spent about 30 sols driving across the surface of Meridiani Planum to the larger (160 m diameter) Endurance crater. One goal of going to Endurance was to determine if the spherules and outcrop rocks were geographically extensive and if so, to use them to probe deeper into the layered sedimentary outcrop deposits. The exploration of Endurance proved that the deposits were indeed laterally extensive, and *Opportunity* was able to explore nearly 8 vertical meters of the layered stratigraphic section exposed within the walls of the crater. From Endurance, the rover began what would ultimately be a trek of more than two Earth years across the plains to the south, ultimately arriving at the even larger (800 m diameter) Victoria crater in September, 2006. As of this writing (mission sol 1075), *Opportunity* has discovered thick, exposed layers of what appear to be sedimentary outcrop rocks at Victoria, and is driving along the rim of the crater searching for a safe entrance and access to those layers. The results described here, however, cover only the part of the plains traverse from Endurance south past a number of plains impact craters and the large (300 m), sand-filled crater Erebus, to a point in the outcrop-rich plains about halfway between Erebus and Victoria (Figure 13.16).

As described in detail in a number of papers (*e.g.,* Squyres *et al.,* 2004b, 2006b; Grotzinger *et al.,* 2005, 2006; McLennan *et al.,* 2005; Morris *et al.,* 2006b; see also Chapter 15 by Morris and Klingelhöfer and Chapter 24 by McLennan and Grotzinger), the spherules discovered in Eagle crater and seen along most of *Opportunity's* traverse have been found to be hematite-rich and have been interpreted as concretions formed from reaction between ground water and minerals in the sediments. The outcrop rock first seen exposed in the walls of Eagle crater and in the shallow subsurface throughout the plains and studied more deeply at Endurance crater has been found to contain high concentrations of sulfur, chlorine, and bromine as well as the minerals hematite and jarosite (a ferric hydroxosulfate: $(K,Na,H_3O)(Fe,Al)_3(SO_4)_2(OH,Cl)_6$ where Fe > Al and OH > Cl). The composition and mineralogy of the outcrop, combined with several key sedimentary features associated with its fine-scale layering, have led to the interpretation that it is a sedimentary sandstone deposit composed of grains of aqueously-altered basaltic material and evaporitic sulfate salts, subsequently reworked by aeolian and additional aqueous processes. These features and processes are consistent with origins in a dune- and interdune-playa geologic setting. These interpretations are extremely exciting; if correct, they imply that there were water-saturated near-surface sediments, including some surface water-lain deposits, in this region of Mars early in the planet's history, and that by terrestrial standards, Mars may once have been "habitable" (see Knoll *et al.* (2005) and Chapter 26 by DesMarais *et al.* for additional discussion of the astrobiological implications). There have been initial alternate hypotheses for the formation of the materials observed at Meridiani, however, that do not necessarily involve abundant surface or near-surface liquid water (*e.g.,* McCollom and Hynek, 2005; Knauth *et al.,* 2005; Zolotov and Shock, 2005; see also Squyres *et al.,* 2006c).

This section of the chapter parallels the sections above for *Spirit* in that we describe the major classes of rocky and fine-grained materials that were characterized by the *Opportunity* Pancams along the Meridiani Planum traverse. Just like at Gusev, Pancam multispectral imaging provides constraints on the composition and mineralogy of these materials that can be used to

enhance, augment, or provide context for more diagnostic measurements from other rover and orbital VNIR instruments.

13.3.2. Outcrop rocks and fracture fill

13.3.2.1. Geomorphology

Pancam monochromatic and stereoscopic observations of rocks and rocky materials at Meridiani Planum, especially at low solar illumination angles, have played important roles in developing models of the geologic history of the region and in selecting specific targets for detailed *in situ* chemical, mineralogic, and Microscopic Imager investigations. Of particular importance for Meridiani outcrop rocks has been the use of the camera's highest spatial resolution near-UV stereo filter combination (the L7 and R1 filters, with effective wavelengths around 435 nm; Bell *et al.,* 2003), low solar illumination angle imaging conditions, and image dithering-enhancement techniques ("super resolution"; Bell *et al.,* 2006b) that all maximize the ability to discern and characterize fine textural detail on rocky surfaces.

For example, blue filter imaging observations within Eagle and Endurance craters and along the rim of Erebus crater have revealed spectacular detail within fine-scale (mm-to cm-thickness) laminated outcrop rocks and layered sedimentary deposits (Figure 13.17). The high resolution and textural detail have allowed specific sedimentological features and facies (different depositional environments or units within one or more related formations) to be identified and mapped, including high-angle, likely aeolian crossbed sets (Figure 13.17c; Grotzinger *et al.,* 2005) and trough (festoon) cross-lamination, likely generated by standing waves in shallow surface water (Figure 13.17e,f; Grotzinger *et al.*, 2006). As described in detail by Squyres *et al.* (2004b, 2006b), Grotzinger *et al.* (2005, 2006), and in Chapter 24 by McLennan and Grotzinger, these morphologic observations provide evidence for both aeolian and surface liquid-water processes having acted, perhaps episodically or rhythmically, in the near-surface environment at Meridiani Planum. They also provide morphologic indications of diagenetic processes (physical and/or chemical changes in sediments after their deposition) having acted at the site, a hypothesis that has been tested using carefully targeted *in situ* APXS and Mössbauer chemical and mineralogic measurements. High-resolution and multispectral Pancam images provide essential context for the *in situ* chemical and mineralogical measurements, including close-up views made with the Microscopic Imager.

A number of other examples of the usefulness of high-resolution morphologic observations in inferring or constraining the composition and/or origin of features have been encountered at Meridiani. For example, the presence of surfaces within Endurance crater that exhibit polygonal fractures (Figure 13.18) have been used to test hypotheses for the origin of these features as (for example) desiccation cracks or a type of "patterned ground" related to freeze-thaw cycling or ice wedging (*e.g.,* McLennan *et al.,* 2005; Jolliff and McLennan, 2006). Thin, apparently fragile rinds and fracture-filling vein-like materials have also been observed in some Meridiani outcrop rocks (Figure 13.19; also discussed below), and models are being developed to test between possible origins of this material from mobile, salt-rich solutions moving up from buried deposits into near-surface fractures in the rock, versus surface aeolian- or perhaps water-transported materials falling down into the fractures (*e.g.,* McLennan *et al.,* 2005; Knoll *et al.,* 2007).

13.3.2.2. Multispectral properties

Outcrop rocks in Eagle Crater and the Meridiani Plains

Pancam multispectral observations of rocks in Eagle crater and on the plains and in the rims of craters south of Endurance crater revealed two main color classes of outcrop rocks. In stretched RGB false color composites generated from Pancam's left eye red-infrared, green, and blue-UV filters (Table 13.1), these two color classes appear yellow to buff-colored and red to purple colored (*e.g.,* Figure 13.20). These kinds of false-color composites significantly enhance what are, in reality, only very subtle color differences when viewed in natural or approximate true color.

A distinctive spectral parameter that defines the difference between these two classes is the 482 to 535 nm spectral slope: the "buff-colored" (in false-color composites) surfaces have a higher 482 to 535 nm slope than the "purple-colored" rock surfaces. Thus, Farrand *et al.* (2006) referred to these classes as the high 482/535 slope (HFS; buff) and the low 482/535 slope (LFS; purple) classes. Representative spectra of these color units are shown in Figure 13.20d. The HFS surfaces are also generally characterized by a flat to convex near-infrared (NIR) spectrum and the LFS surfaces by a flat to concave (shallow absorption centered at 900 nm) NIR spectrum. LFS surfaces are most often associated with steeper faces (such as on the rock "Cathedral Dome" shown in Figure 13.20) and the distal portions of outcrop layers. HFS surfaces are most often flat-lying. Figure 13.20a,b shows an L357 composite and a Decorrelation Stretch (DCS: essentially a color composite generated from the top three principal components of variance in a data set; Gillespie *et al.,* 1987) version of the image sequence on Cathedral Dome in Eagle crater. The flat top of that rock, the lower angle lower portion, and vugs (small cavities) and other furrows or cracks in the rock are HFS-class materials and the steeper face is LFS-class material. One interpretation relies on the hypothesis that all of these outcrop rocks have an external veneer or rind of more weathered (more Fe^{3+}-rich) HFS-class minerals. The weathered veneer could be partially or wholly stripped away on steeper, wind-scoured LFS-class faces (which have been shown to be more resistant to RAT grinding and thus presumably more resistant to erosion than the weathered veneers; *e.g.,* Arvidson *et al.*, 2004). However, the veneers remain on more flat-lying surfaces and in sheltered vugs and furrows where they are less susceptible to wind-related erosion. Additionally, RAT brushing of some HFS surfaces has also revealed LFS surfaces beneath (Farrand *et al.,* 2006).

Despite the interpretation of the HFS surfaces as a weathering veneer, Pancam observations have revealed some inherent color differences in rock interiors as well. For example, the McKittrick and Guadalupe RAT hole interiors have distinctly different visible to NIR spectra (Figure 13.21). Some of this difference could be due to slightly differing degrees of brushing and "cleaning" of the RAT holes, however. Pancam spectra also reveal evidence of disseminated, fine-grained crystalline ("red") hematite within the outcrop, because cuttings from RAT grindings have spectral features indicative of fine-grained red hematite (*e.g.,* Figure 13.22; Bell *et al.,* 2004b; Farrand *et al.,* 2006). While grinding of larger gray-hematite bearing spherules (discussed below) could produce fine-grained red hematite in some RAT holes, Mössbauer measurements on a number of spherule-free RAT holes also show the presence of hematite not associated with spherules within the sulfate-rich rock (Morris *et al.*, 2006b).

Outcrop rocks in Endurance and Erebus Craters

The layers of the Karatepe stratigraphic sequence examined within Endurance crater also exhibited color differences on undisturbed rock surfaces and within RAT hole interiors. As described by Farrand *et al.* (2006), these differences can be related to subtle variations on the basic HFS and LFS color classes discussed above. Some of the more stark color differences observed between the upper and lower parts of the layered outcrop section exposed at Endurance crater were later determined to be caused largely by rougher textures in the lower part of the section (*e.g.,* Figure 13.23; Grotzinger *et al.,* 2005; Farrand *et al.,* 2006), which exhibited more shadowing and also appeared to preferentially trap dark basaltic sand. Still there were color differences observed among the undisturbed Karatepe units which, in association with textural differences noted in other Pancam and MI images, were used to establish the stratigraphy of these sedimentary units and to select targets for *in situ* examination.

For example, the series of RAT holes created during the entrance into Endurance Crater (Figure 13.24) were analyzed by all instruments to provide a suite of geochemical and mineralogical measurements along the stratigraphic sequence of outcrop rocks at Karatepe West (*e.g.,* McLennan *et al.,* 2005; Clark *et al.,* 2005; Morris *et al.,* 2006b). Pancam spectra demonstrated that the abraded and brushed surfaces of the RAT holes were quite similar in their overall high reflectances and weak 900 nm absorption features. RAT tailings exhibited slightly more pronounced absorptions, interpreted to reflect the presence of fine-grained hematite (Farrand *et al.,* 2006). Pancam spectra of the interior of spherules cut by the RAT were nearly identical to undisturbed spherules present on the surface, consistent with their lack of interior structure in Microscopic Imager images (Figure 13.23). Millimeter-scale nodules and overgrowths on spherules eroded from this section of the outcrop were interpreted by McLennan *et al.* (2005) to represent second generation cements. Pancam spectra of the overgrowths are nearly identical to those of the outcrop rocks.

Many Pancam images of Meridiani outcrop surfaces have sufficient spatial resolution (<10 mm) to allow detailed multispectral studies on individual sedimentary structures as well as erosional and possible secondary diagenetic features (*i.e.*, fracture fill and rind materials, discussed below). For example, Figure 13.25 shows the results of an analysis of fine laminations in outcrop rock near the rim of Erebus crater (Thompson *et al.,* 2006). Typically, from 10 to 30 pixels could be analyzed from individual laminations across approximately 10 cm of vertical stratigraphic section in this region. Nearly all laminations were exposed in direct sunlight, where image quality was sufficient for pixel selections in all bands, and where interfering physical effects, such as shadows or changing phase angles due to topography could be minimized. Example spectra from some of these laminations are also shown in Figure 13.25. Most outcrop spectra at this fine scale exhibit a steep positive slope in the visible region and subtle changes in the NIR (*e.g.,* flat, concave, or convex profiles in the 753 nm to 1009 nm region and weak absorption features in the 904 to 934 nm region). Reflectance maxima are typically in the 750-850 nm region but have been observed as low as 673 nm and as high as 1009 nm, with the latter usually related to the presence of the lower albedo materials (*i.e.*, spherules and basaltic sands). A major difference between the specific outcrop layers analyzed here is in the slope of the spectrum in the 934 to 1009 nm region. Positive slopes at these wavelengths are consistent with the presence of hematite, likely associated with the spherules (*e.g.,* Bell *et al.,* 2004b; Farrand *et al.* 2006). Interestingly, the higher albedo surfaces in Figure 13.25 tend to have the strongest

negative spectral slopes at the longest wavelengths. This could be an intrinsic characteristic of the outcrop material or could indicate the presence of a thin weathering rind or dust deposit on these surfaces (perhaps consistent with the observation and interpretation of the weathered HFS surfaces noted above and by Farrand *et al.*, 2006). Rarely, hematite-rich spectral signatures are present in one lamination and not in the adjacent layers. Occurrences like this could be the result of a single iron-rich primary sedimentary episode or a secondary process such as diagenetically related cementation or recrystallization, or could be associated with an invasive vein or fracture fill material. Additional study of these kinds of small-scale spectral variations thus could provide unique insights on the style and extent of the sedimentary depositional events that created the ubiquitous outcrop rocks studied by *Opportunity* in Meridiani Planum.

Rinds and fracture fills

As noted above, examples of rinds and fracture fill materials were encountered in Pancam observations, initially in Eagle crater, but also in Endurance crater and on the plains to the south. For example, during the ingress to Endurance Crater, fracture filling materials were observed coating the broken edges of some outcrop blocks (*e.g.,* Farrand *et al.,* 2006; Jolliff *et al,* 2006). Fracture fill materials appear to have color properties distinct from other parts of the outcrop. For example, in plots of spectral parameters such as the 535 nm band depth vs. 601 nm band depth (Figure 13.26), the rind and fracture fill materials plot between the outcrop and other components of the Meridiani surface layer (namely, basaltic sands, hematitic spherules, and dark cobbles). These materials can have variable spectral properties but are often characterized by higher reflectances at the shortest visible wavelengths and a discernable NIR absorption centered at 900 nm (*e.g.,* Figure 13.27; Farrand *et al.*, 2006). An excellent example was observed along the eastern-most extent of the Opportunity traverse, where fracture filling materials extended nearly orthogonally through the Burns Cliff formation (Figure 13.28). Decorrelation stretches of Pancam images showed the surface of these features to exhibit extreme (for Mars) color variations over small length scales, consistent with their inferred emplacement from the presence of intermittent aqueous solutions (*e.g.,* Knoll *et al.,* 2007).

13.3.3. Spherules

13.3.2.1. Morphology and occurrence

One of the most surprising and exciting findings from *Opportunity's* exploration of Meridiani Planum was the discovery that the surface, almost everywhere that the rover traversed, was covered by small (1-5 mm), dark, gray to reddish spherical grains (*e.g.,* Figure 13.29; Soderblom *et al.,* 2004; Weitz *et al.,* 2006). They were given the nickname "blueberries" by the MER science team partly because these spherules are less red than the surrounding soils and outcrop on which they lie (or are embedded), and partly because they light up as garishly blue or purple in false color Pancam RGB composite images generated using the near-UV (L7, 430 nm), green (L5, 535 nm), and near-IR (L2, 750 nm) filters.

The spherules are distinctly harder than the rock in which they occur, hence they stick out on weathered rock surfaces and accumulate as a resistant lag when the other components of the outcrop rocks weather away. They are remarkably spherical and form an “overdispersed” distribution, which is indicative of formation as concretions (*e.g.,* McLennan *et al.,* 2005; see also Chapter 24 by McLennan and Grotzinger). That is, they grow by chemical diffusion in an

aqueous medium, so they tend to be separated from each other and are not concentrated along primary sedimentary features such as bedding and laminations. This distribution provides strong evidence that the spherules formed in a diagenetic setting, that is, by a reaction after the sediments were buried. In some cases, spherules "inherit" a slight bulge or elongation where they directly intersect a lamination, again consistent with replacive growth after the sediments were buried. Spherules that have been cut by natural processes or ground by the RAT show uniform interiors and lack the concentric zonation commonly seen in terrestrial concretions.

13.3.2.2. Chemical and mineralogical properties

All of Opportunity's analytical instruments have been used to attempt to determine the mineral and chemical makeup of the spherules. For the IDD instruments and for the Mini-TES, the spherules are always part of a mixed target, either spherules plus rock or spherules plus soil, thus the spherule compositions must be inferred from analyses of the mixtures. Results of chemical analyses clearly reflect enrichment in ferric iron, and modelling the results and chemical trends in terms of mixtures of soil and rock components indicates that the spherules must have at least 50-60% by weight hematite, and possibly more (Gellert *et al.*, 2007; Schneider *et al.,* 2007; Jolliff *et al.,* 2005, 2007). Results from the Mössbauer spectrometer indicate that among the Fe-bearing phases, hematite is by far the dominant component of the spherules and that they contain no jarosite (Morris *et al.*, 2006b), thus during growth of the concretions all of the ferric sulfate is converted to hematite. Mini-TES spectra of fields of view dominated by spherules likewise are dominated by the spectral features of well-crystallized hematite (Christiansen *et al.*, 2004).

13.3.2.3. Multispectral properties

The soils of Meridiani Planum display a variety of visible and near infrared spectral properties. The upper lag surface of the soils is composed of basaltic sand, dust, millimeter-size hematite-rich spherules interpreted as concretions, spherule fragments, coated partially buried spherules, basalt fragments, sedimentary outcrop fragments, and cm-size loose rock fragments (Sullivan *et al.,* 2005; Weitz *et al.*, 2006). Beneath the lag deposit, the soils are dominated by finer-grained basalt sands and dust. The Pancam observations of any given soil patch reflect the variations in the kinds of grains that compose the soil. False-color composites and decorrelation stretches of Pancam soil observations are extremely useful for characterizing different spectral properties of millimeter-size and larger grains.

The hematite-rich spherules (Klingelhöfer *et al.,* 2004; Christensen *et al.,* 2004; Morris *et al.,* 2006b) have an absorption around 900 nm and a strong positive inflection from the Pancam's R6 to R7 filters (934 to 1009 nm). These features have been attributed to hematite in the blueberries (*e.g.,* Bell *et al.*, 2004b; Soderblom *et al.*, 2004). Not all spherules appear blue in Pancam false-color composites, however. Many of the partially buried spherules appear yellower, which is consistent with the presence of a dusty coating (Bell *et al.*, 2004b; Soderblom *et al.*, 2004). For example, the Eagle crater spherules shown in Figure 13.29, which have an average major axis of 3.15±1.2 mm, have both bluish and yellowish populations in false color views, suggesting variable degrees of dust covering/coating (Weitz *et al.,* 2006).

Examples of spectra extracted from small numbers of pixels on the various spherules in Figure 13.29 are shown in Figure 13.30. The spectrum of the RAT-ground spherules is an

average of two spectra from spherules that were still embedded in the Eagle crater outcrop but which had been ground down to about half their diameter by the RAT to expose a fresh interior. This fresh spherule interior has the strongest upturn between the 933 and 1009 nm filters and exhibits a strong inflection or "kink" in the spectrum around 535 nm. Both of these characteristics are consistent with the presence of hematite within the spherules (*cf.* Figure 13.22b). Several spherules perched on the soil also have a strong increase in reflectance between the 933 and 1009 nm filters, in addition to a near-IR absorption band centered around 900 nm and shallow spectral slope in the visible. In Figure 13.29, these perched spherules appear lighter blue in color. These spectral characteristics are consistent with the spherules being relatively "clean" (dust-free) and having a surface component of coarser-grained ("gray"), perhaps even specular hematite compared to the RAT-ground spherule interiors. Those spherules that are partially buried to varying degrees in the soil appear yellower in Figure 13.29 because of a reduced absorption around 900 nm and a steeper red spectral slope in the visible. These spectral characteristics are consistent with dust coating or adhering to the surfaces of these spherules to varying degrees. Even though spherules perched on the soil do not show the dust-like coating seen on the partially buried spherules, they still exhibit different spectra than the fresh RAT-exposed interiors of spherules embedded in the outcrop. One hypothesis is that once spherules erode out of the outcrop rocks in which they formed, they "weather" (either physically as a result of wind-driven sand-blasting, or chemically from interactions with minor water vapor) or become covered by fine-grained dust after they fall on the ground or are exposed to the atmosphere (*e.g.,* Weitz *et al.,* 2006).

13.3.4. Cobbles, rock fragments, and meteorites

13.3.4.1. Geomorphology

Loose, dark, rocky fragments and cobbles are also visible in Pancam observations of many soils. The fragments are generally just a few centimeters in size, but larger rocks have also been found. The rock fragments tend to concentrate in troughs between ripples and in association with outcrop exposures. There are several types of rocks and rock fragments that have been identified based upon both Pancam observations and geochemical analyses by the APXS and Mössbauer. Two of the best examples are shown in Figure 13.31. Bounce Rock (Figure 13.31a), so named because of its location next to an airbag bounce mark made just outside Eagle crater by the rover's landing system, was noticed from a distance to be distinctly different morphologically, texturally, and spectrally from other rocky materials in Meridiani Planum. Pancam, MI, and ultimately *in situ* chemical and mineralogical observations revealed this rock to be rich in pyroxene, and likely a piece of ejecta from a distant impact that sampled surface/subsurface materials not present at the surface where *Opportunity* has traversed (*e.g.,* Figure 13.8b; Rieder *et al.,* 2004; Bell *et al.,* 2004b; Christensen *et al.,* 2004; Klingelhöfer *et al.,* 2004; Morris *et al.,* 2006b). Mineralogical and chemical analyses showed this rock to be very similar in its makeup to one of the basaltic martian meteorites found previously on Earth (EETA79001 “Lithology B”; Rieder *et al.*, 2004).

Heat Shield Rock (Figure 13.31b), so named because it was discovered near the debris from the rover landing system's heat shield impact site on the plains south of Endurance crater, exhibits a heavily pitted/eroded morphology and a highly specular surface (Squyres *et al.,* 2006b). The morphology of this rock was immediately suggestive of meteoritic regmaglypts (thumbprint-like indentations), and the specular nature of the surface (in both the visible and the

infrared: see Chapter 14 by Ruff *et al.*) suggested a metallic composition. Pancam multispectral observations (discussed below) were also consistent with a metallic composition. Heat Shield Rock was ultimately shown to be an iron meteorite by APXS and Mössbauer measurements that detected high abundances of Fe and Ni as the meteoritic metallic mineral kamacite (Morris *et al.,* 2006b; Yen *et al.,* 2006). Kamacite has also been identified in the cobble named Barberton (Morris *et al.*, 2006b; Gellert *et al.*, 2007), implicating it as another possible meteorite near the rim of Endurance crater.

Other smaller rock fragments and cobbles, such as Lion Stone and Russet, have been interpreted as ejecta, but they have compositions that match the sulfate-rich outcrop rocks and so appear to be locally derived (*e.g.,* Jolliff *et al.,* 2006b). Another class of cobbles was found to be abundant near Erebus crater, and several were investigated with the rover's *in situ* arm instruments, including cobbles named Arkansas, Perseverance, and Antistasi (Figure 13.32). These cobbles have chemical compositions (in particular, sulfur contents) that are intermediate between those of the basaltic soils and the outcrop rocks, and they have heterogeneous surface textures that suggest they might be impact breccias or that they have unusual patchy coatings (see below).

13.3.4.2. Multispectral properties

Pancam and Microscopic Imager studies of cobbles and rocks in Meridiani reveal discontinuous lighter-toned patches across many of their surfaces, as discussed by Weitz *et al.* (2006). The cobbles named Arkansas, Perseverance (Figure 13.32), and Antistasi as well as hundreds of others resting on soil or low-lying outcrop, have very distinct visible and near infrared spectral properties (Figure 13.33) compared to the outcrop. Specifically, these cobbles exhibit low albedo and lower 535 nm and higher 904 nm band depths compared to the outcrop. Spectra extracted from the eight rocks mentioned by name in this section, as well as from numerous other rock fragments not analyzed geochemically with the rover arm instruments, show a great diversity of compositions, and hence potential origins (*e.g.,* Bell *et al.,* 2004b; Weitz *et al.,* 2006). In addition, several of the rock fragments exhibit apparent coatings, including examples of dust derived from the local outcrop that appears to have become deposited on the loose rock surfaces. As shown in Figure 13.33, Pancam spectra of the lighter-toned patches are more similar to outcrop rock, whereas the darker regions are more like spectra of basaltic materials. The strong tendency for rock fragments to occur on and near outcrop exposures suggests that many rock fragments are either impact ejecta derived from the sulfate-rich outcrop, are from underlying or formerly-overlying stratigraphic layers not currently analyzed *in situ* by the *Opportunity* rover, or some combination of both.

Heat Shield rock is one of most intriguing large rocks encountered by *Opportunity*. Figure 13.34 shows Heat Shield rock after the RAT brushed the surface and compares the spectra of brighter dust and darker soil that collected in small dimples (possibly regmaglypts) on the surface, as well as dusty and brushed surfaces of the meteorite that appeared coated with a "bluer" material compared to the majority of the surface. The brushed, uncoated material is quite similar to laboratory spectra of the Canyon Diablo meteorite (*e.g.,* Gaffey, 1976; Britt and Pieters, 1987). Heat Shield rock was subsequently determined to be an Fe-Ni meteorite based on APXS and Mössbauer measurements (*e.g.,* Morris *et al.,* 2006b; Yen *et al.,* 2006). Differences in brightness and spectral slope between the spectra of laboratory Fe-Ni meteorites and Heat Shield rock may be related to differences in surface roughness and/or nickel abundance.

13.3.5. Soils and windblown drift deposits

13.3.5.1. Geomorphology

Examples of different morphologic classes of fine-grained materials encountered during *Opportunity's* traverse in Meridiani Planum are shown in Figure 13.35.

Soils on the plains of Meridiani appear to be lag deposits that are generally mixtures of basaltic sand, dust, coated and uncoated spherules and their fragments, and fragments of other rocks such as those mentioned in the previous section (*e.g.,* Figure 13.36; Bell *et al.,* 2004b; Soderblom *et al.,* 2004; Weitz *et al.,* 2006; Morris *et al.,* 2006b). Plains soils appear to be more limited in the variety of soil grain sizes and compositions compared to the soils seen in Eagle and Endurance craters (Weitz *et al.*, 2006). Ripples cover the plains and are also seen inside craters. MI images taken on ripple crests along the plains show they are composed of rounded grains of similar size, with an average grain size smaller than typical spherules seen in Eagle crater (Herkenhoff *et al.*, 2004, 2006; Sullivan *et al.,* 2005; Weitz *et al.*, 2006).

13.3.5.2. Multispectral properties

Pancam spectra of typical bright "dusty" and dark "sandy" soils in Meridiani Planum are generally consistent with previous average bright and dark region telescopic spectra and IMP multispectral data (Figure 13.8b) and are similar to those observed in Gusev crater (Figure 13.37; Yen *et al.,* 2005). As discussed previously, bright, reddish spectra in Meridiani like those in Figure 13.37 are consistent with a ferric-iron rich composition dominated by nanophase, rather than crystalline, ferric oxides (*e.g.,* Morris *et al.,* 1989; Bell *et al.,* 1990). Differences in the absolute reflectivity of the bright, dusty soils between Meridiani (brighter) and Gusev (slightly darker) could result from slightly smaller dust grain sizes at Meridiani relative to Gusev, or to the presence of a locally-derived and slightly brighter component in the Meridiani dust (perhaps "outcrop dust"?) and/or the presence of a locally-derived and slightly darker component in the Gusev dust (perhaps "rock dust"?). Physical, rather than mineralogic or compositional differences are likely to be contributors to the difference because of the well-mixed and ubiquitous nature of the global dust. A particle size (or other physical) explanation is also supported by the fact that the iron-bearing mineralogy and chemical composition of the dusty soils at Gusev and Meridiani are quite similar (Morris *et al.,* 2006b). Howerver, the presence of a locally-derived dark but extremely fine-grained component at Gusev is supported by the identification of fine-grained "rock dust" component to the spectra of several locations at the Mars Pathfinder landing site (Bell *et al.,* 2002). Evidence for a possible "outcrop dust" component to the fine-grained dusty soils at Meridiani comes from the increased reflectance of Meridiani dust at the shortest wavelengths compared to Gusev dust, a spectral characteristic consistent with the most altered Meridiani outcrop surfaces (*e.g.,* the unit HFS spectra in Figure 13.20d and Farrand *et al.,* 2006).

The dark soils are extremely similar at Gusev and Meridiani (Figure 13.37), and are generally similar to Pathfinder and telescopic dark soil and low albedo region spectra (Figure 13.8b). MER dark soils exhibit a shallow and broad absorption centered near 900 nm and a negative 900 to 1000 nm spectral slope that likely results from the presence of ferrous-iron bearing silicates (*e.g.,* pyroxene, olivine). A similar or stronger band at the same position is seen in Pancam spectra of some of the "cleanest" rock surfaces at Gusev and in spectra of at least one

large basaltic rock at Meridiani: Bounce Rock (Figures 13.8 and 13.9). Thus, the dark soils at both MER sites contain a significant component of less altered mafic material, and, by analogy to the dust, this material may represent another "globally homogenized" spectral unit that could be expected to be widespread across the planet (*e.g.,* Yen *et al.,* 2005). Conversely, the global homogeneity of the dark material may simply be a manifestation of the widespread, global availability of basaltic, sand- and dust-sized materials on the planet (*e.g.,* Morris *et al.,* 2006a,b).

Figure 13.29b illustrates that the fine-grained, dark, sandy basaltic soils in Meridiani occur in two populations in false color composites: purplish or yellowish. The main spectral difference between the two soils is shown in Figure 13.30. The "yellower" dark soil appears slightly brighter and redder in Pancam spectra, and with a slightly deeper 535 nm "kink" in the spectrum; there are no significant differences in near-IR absorption bands between these populations. This suggests that the brightness differences may result from a fine dust coating on some of the soil grains. This hypothesis is supported by the observation that no morphologic differences can be seen in the associated MI images that correspond to these two soil colors (Soderblom *et al.,* 2004; Weitz *et al.,* 2006).

Pancam spectra of the Meridiani plains ripples have similar shapes to spectra of the spherules, although with a less-pronounced absorption around 900 nm. Mössbauer measurements on the ripple crest target named Aegean Crest and other ripple crests indicated the presence of hematitic soil, with an even higher concentration of hematite than in the plains soils (*e.g.,* Klingelhöfer *et al.*, 2004; Morris *et al.,* 2006b). These high hematite measurements, along with the Pancam spectral similarity to the spherule signature, support the hypothesis that the grains on the ripples are spherules and/or their broken fragments (*e.g.,* Herkenhoff *et al.,* 2004; Sullivan *et al.,* 2005).

13.4. Correlating and coordinating observations: implications for future surface and orbital remote sensing of Mars

Mars Exploration Rover observations and results in Gusev crater and Meridiani Planum provide valuable experience with complex, complementary science instrument payload elements (on the surface and in orbit) that can be applied to future surface or orbital remote sensing and *in situ* investigations of Mars. Whenever possible during both *Spirit's* and *Opportunity's* traverses, efforts have been made to try to bring as much of the full suite of each rover's science payload (Squyres *et al.,* 2003) to bear as possible for each target of interest, within the real-world constraints on power, data volume, and measurement duration imposed at any given time. In addition, a number of dedicated coordinated/simultaneous observation campaigns have been conducted between instruments on the rovers and those on the Mars Global Surveyor, Mars Odyssey, Mars Express, Mars Reconnaissance Orbiter, and even the Hubble Space Telescope (*e.g.,* Arvidson *et al.,* 2006a; see Chapter 21 Golombek *et al.* for details).

One example from rover observations comes from work by Calvin and Shoffner (2006) attempting to seek correlations and complementarity of results between Pancam visible to near-IR observations and Mini-TES thermal infrared observations of the same targets. Comparing data sets in these widely different spectral domains provides a way, for example, to test the hypothesis that the only contribution to the strong infrared signature of hematite detected in Meridiani Planum from orbit was from the small hematitic spherules found at the landing site

(*e.g.*, Christensen *et al.*, 2000, 2004). Analysis of the sulfate-dominated outcrop has shown that it has a detectable hematite signature in Pancam visible to near-IR measurements (see above and Bell *et al.*, 2004b; Farrand *et al.*, 2006) and it also exhibits a weak but identifiable feature of "coarse" hematite in Mini-TES spectra (Figure 13.38; Christensen *et al.*, 2004; see also Chapter 14 by Ruff *et al.*). This suggests that thermal infrared measurements may be sensitive to finer, distributed hematite in addition to the coarser-grained spherules.

Calvin and Shoffner (2006) performed an analysis of concurrent Pancam and Mini-TES observations of typical soils taken periodically in the traverse from Endurance crater south toward Victoria crater in order to explore the correlation between the hematite signature observed by Mini-TES and the amount of cover by spherules and their fragments as seen by Pancam. Sixty coordinated observations of soils in the near field were made between sols 70 and 800, and approximately 25 of these were found to have both good Pancam coverage (full 13 filter) and high signal to noise Mini-TES spectra. Typical examples of low and high spherule cover and weak and strong Mini-TES hematite signatures are shown in Figure 13.39. Coverage by spherules was determined using unsupervised classification and thresholding on whole-image color ratios or decorrelation stretches that enhance the appearance of "berries" against the background soils. Mini-TES band strength was determined using the feature near 550cm^{-1}, after correcting the spectra for contributions from downwelling sky radiance and dust on the instrument mirror (see Chapter 14 by Ruff *et al.* for details). Both berry cover and Mini-TES band strength vary strongly in the data set (Figure 13.40). Berry cover can vary because of local soil variations (Figure 13.39a), and/or the presence of outcrop, large cobbles, or other atypical "soil" materials present in the scene. Pancam area cover by spherules was estimated to be uncertain by approximately $\pm$ 5% because of shadowing and variable quality (bits/pixel) of the images, and the Mini-TES hematite index was estimated to be accurate to ~0.002. No systematic trend with time (a proxy for position along the traverse) was detected, showing that the Pancam-derived berry cover and the Mini-TES derived hematite index are sensitive to the heterogeneous nature of the local region where the systematic observations occurred. Although the size of the spherules was observed to decrease significantly in the vicinity of Erebus crater (Weitz *et al.*, 2006) the areal coverage and infrared hematite index do not show any correlated change.

Another example of coordinated observations involving Pancam are the frequent "albedo" observations acquired by both rovers during their respective traverses. Observations using Pancam's broadband L1 filter (739±338 nm), calibrated to radiance factor and then divided by the cosine of the average solar incidence angle at the time of the observation, have been shown to provide a reasonably accurate estimate of the Lambert albedo of the surface, based on comparisons with Viking IRTM and TES bolometric albedos from orbit (Bell *et al.*, 2004b, 2006b; Golombek *et al.*, 2005). Estimating the broadband albedo of the surface along the traverses provides a way to intercompare (and cross-calibrate) surface and orbital observations at a wide variety of spatial scales, and a way to monitor seasonal and inter-annual variations in albedo from a variety of platforms. Pancam albedo observations also provide key inputs for modeling of the thermal inertia of the surface from Mini-TES observations (*e.g.*, Fergason *et al.*, 2006).

A final example of coordinated Pancam observations is the study by Arvidson *et al.* (2006b), who compared orbital observations from the Mars Express OMEGA instrument (see

Chapter 7 by Bibring and Langevin) to surface measurements made at Meridiani Planum by the Opportunity rover. Of particular interest to this discussion is the comparison of the OMEGA spectra of the Meridiani plains to those collected by Opportunity's Pancam. Mars Express orbit 1183 passed directly over the Opportunity landing site. OMEGA data from this orbit had a spatial resolution of approximately 700 m along-track and 500 m cross-track. The OMEGA spectrum for the Opportunity landing site shows a red visible to infrared spectrum with a broad reflectance maximum near 1.5 μm and broad absorptions near 1 and 2 μm consistent with the presence of pyroxenes. More detailed comparisons were made over the terrain between Endurance and Erebus craters. Increases in albedo were observed in OMEGA data in regions where Opportunity observed greater fractions of outcrop exposed on the plains. Given the relatively large OMEGA pixel size, the OMEGA spectra over Opportunity's traverse path corresponded most closely to Pancam spectra of the ripple and inter-ripple trough features which dominate the plains. Arvidson *et al.* (2006b) also pointed out that results from Pancam, OMEGA, and Mini-TES spectra all indicate or are consistent with the presence of pyroxene, but not olivine, on the Meridiani plains, which contradicts results from the Mössbauer spectrometer which indicated that iron was approximately equivalently split between pyroxene and olivine. They attributed the lack of detection of the olivine signature to the predominance of pyroxene spectral features in non-linear spectral mixtures (*e.g.,* Singer, 1981) and to the spectral masking effects of nanophase ferric oxides. Chapter 21 by Golombek *et al.* provides additional details and examples on this and other Pancam/orbital data correlated observations.

Given the enormous number of imaging, spectroscopic, chemical, and mineralogic observations in hand from the rovers and the variety and coverage of orbital imaging, compositional, and physical properties data sets either acquired or planned for the near future, these kinds of coordination and correlations between and among surface and orbital measurements and investigations represents a fertile area of potential future study. For example, while hundreds of *in situ* MER APXS and Mössbauer measurements have been made on targets of high scientific interest in both Gusev and Meridiani, orders of magnitude more targets of potential interest could only be analyzed using Pancam or Mini-TES remote sensing observations. Might there be a way to correlate *in situ* chemistry and/or mineralogy from certain endmember areas with visible/near-IR or thermal-IR spectroscopic properties over broader regions, thus enabling the potential to "paint" the chemistry or mineralogy across targets that could not be directly measured *in situ*? As another example, it is possible to use surface Pancam and Mini-TES remote sensing observations to validate and refine the calibration of orbital visible/near-IR and thermal-IR remote sensing instruments (as has already been done for the Mars Odyssey THEMIS-VIS camera, for example; McConnochie *et al.,* 2006), as well as to constrain the spectroscopic and radiative properties of atmospheric aerosols by comparing simultaneous measurements acquired through different atmospheric pathlengths (*e.g.,* Wolff *et al.,* 2006). There is significant potential for these and other kinds of coordinated Pancam observation and analysis campaigns to yield new information on the composition, mineralogy, and physical properties of the martian surface.

13.5. A closing perspective

Pancam observations have provided some of the most dramatic and beautiful views of Mars yet obtained, but as described in this chapter and elsewhere in this book, they have also provided, augmented, or enabled important geologic, compositional, and mineralogic discoveries

about the surface of the Red Planet. The ability to obtain high spatial resolution (comparable to human vision), stereoscopic, multispectral images has been a critical factor in the operational successes and scientific discoveries achieved by the Mars rovers Spirit and Opportunity. In that vein, Pancam observations have provided an evolutionary step in martian robotic imaging campaigns, building on and expanding from the previous successes achieved by imaging systems on the Viking and Mars Pathfinder landers. Increased resolution is perhaps the single most important evolutionary step taken as part of the Pancam investigation (Bell *et al.,* 2003), but it is not the only one. Other examples of advances realized in the Pancam experience include enhanced onboard image acquisition and image processing software, including an extremely robust and efficient data compression scheme that allowed a substantial reduction in the number of bits downlinked to Earth without the introduction of excessive image artifacts (*e.g.,* Maki *et al.,* 2003); the ability of the rovers to transmit more than 90% of their data back to Earth through relay satellites like Mars Odyssey rather than Direct-to-Earth (DTE), increasing the total science data return (most of it Pancam data) by about an order of magnitude compared to a DTE mission; and the development and optimization of quick-look, tactical-timescale data calibration, mosaicking, and multispectral image analysis software and methods that enabled the best potential *in situ* instrument measurement sites to be selected from images that had often been acquired and downlinked less than one martian day before. Experience gained, lessons learned, and results obtained from the Pancam investigation are already feeding forward to motivate new evolutionary steps in surface imaging on future Mars lander and rover spacecraft. It is exciting to imagine what new discoveries await.

Acknowledgements. These spectacular observations of Mars from the *Spirit* and *Opportunity* Pancam instruments have been made possible by the hard work and dedication of a team of many hundreds of scientists, engineers, managers, and administrators at the Jet Propulsion Laboratory, Cornell University, and dozens of other universities, laboratories, and contractor facilities around the world. We owe them all our thanks. This work was supported by NASA Mars Exploration Rover program grants and contracts to Cornell University, JPL, University of Nevada, Space Science Institute, Arizona State University, U.S. Geological Survey, NASA/Johnson Space Flight Center, Washington University, and the Planetary Science Institute.

References

Adams, J. B. (1974). Visible and near-infrared diffuse reflectance spectra of pyroxenes as applied to remote sensing of solid objects in the solar system. *J. Geophys. Res.,* **79***,* 4829-4836.

Adams, J. B., Smith, M. O., and Johnson, P. E. (1986). Spectral mixture modeling: A new analysis of rock and soil types at the Viking Lander I site. *J. Geophys. Res*., **91**, 8098-8112.

Arvidson, R. E., Gooding, J. L., and Moore, H. J. (1989). The Martian surface as imaged, sampled, and analyzed by the Viking Landers. *Rev. Geophys.,* **27**, 39–60.

Arvidson, R.E., Anderson, R. C., Bartlett, P., *et al.* (2004). Localization and Physical Properties Experiments Conducted by Spirit at Gusev Crater. *Science,* **305***,* 821-824.

Arvidson, R. E., Squyres, S. W., Anderson, R. C., *et al.* (2006a). Overview of the *Spirit* Mars Exploration Rover mission to Gusev crater: Landing site to Backstay rock in the Columbia Hills. *J. Geophys. Res.,* **111**, E02S01, doi:10.1029/2005JE002499.

Arvidson, R. E., Poulet, F., Morris, R. V., *et al.* (2006b). Nature and origin of the hematite-bearing plains of Terra Meridiani based on analyses of orbital and Mars Exploration Rover data sets. *J. Geophys. Res.,* **111**, E12S08, doi:10.1029/2006JE002728.

Bandfield, J. L., Glotch, T. D., and Christensen, P. R. (2003). Spectroscopic Identification of Carbonate Minerals in the Martian Dust. *Science,* **301**, 1084-1087.

Bell III, J. F., Savransky, D., and Wolff, M. J. (2006a). Chromaticity of the martian sky as observed by the Mars Exploration Rover Pancam instruments. *J. Geophys. Res.,* **111**, E12S05, doi:10.1029/2006JE002687.

Bell III, J. F., Joseph, J., Sohl-Dickstein, J. N., *et al.* (2006b). In-flight calibration and performance of the Mars Exploration Rover Panoramic Camera (Pancam) Instruments. *J. Geophys. Res.,* **111**, E02S03, doi:10.1029/2005JE002444.

Bell III, J. F., McSween Jr., H. Y., Crisp, J. A., *et al.* (2000). Mineralogic and Compositional Properties of Martian Soil and Dust: Results From Mars Pathfinder. *J. Geophys. Res.,* **105**, 1721-1755.

Bell III, J. F. (1996). Iron, sulfate, carbonate, and hydrated minerals on Mars, in "Mineral Spectroscopy: A Tribute to Roger G. Burns." *Geochemical Society Special Publication 5*, eds. M. D. Dyar, C. McCammon, and M. W. Schaefer, 359-380.

Bell III, J. F., Squyres, S. W., Herkenhoff, K. E., *et al.* (2003). The Mars Exploration Rover Athena Panoramic Camera (Pancam) Investigation. *J. Geophys. Res*., **108** (E12), doi:10.1029/2003JE002070.

Bell III, J. F., Squyres, S. W., Arvidson, R. E., *et al.* (2004a). Pancam multispectral imaging results from the Spirit rover at Gusev crater. *Science,* **305**, 800-806.

Bell III, J. F., Squyres, S. W., Arvidson, R. E., *et al.* (2004b). Pancam multispectral imaging results from the Opportunity rover at Meridiani Planum. *Science,* **306**, 1703-1709.

Bell III, J. F., Farrand, W. H., Johnson, J. R., and Morris, R.V. (2002). Low abundance materials at the Mars Pathfinder landing site: An investigation using spectral mixture analysis and related techniques. *Icarus,* **158**, 56-71.

Bell III, J. F., McCord, T. B., and Owensby, P. D. (1990). Observational Evidence of crystalline iron oxides on Mars. *J. Geophys. Res.,* **95**, 14447-14461.

Bishop, J. L., Banin, A., Mancinelli, R. L., Klovstad, M. R. (2002). Detection of soluble and fixed NH4+ in clay minerals by DTA and IR reflectance spectroscopy: a potential tool for planetary surface exploration. *Planet. Space. Sci*., **50**, 11-10.

Britt, D. T., and Pieters, C. M. (1987). Effects of small-scale surface roughness on the bidirectional reflectance spectra of nickel-iron meteorites. *Lunar Plan. Sci. Conf. XVIII,* 131-132.

Brückner, J., Dreibus, G., Gellert, R., *et al.* (2007). Mars Exploration Rovers – Chemical Composition by the APXS, Chapter 4 in *The Martian Surface: Composition, Mineralogy, and Physical Properties*, ed. J. F. Bell III, Cambridge University Press, in press.

Calvin, W. M. and Shoffner, J. D. (2006). Hematite at Meridiani: Results From Mini-TES and Pancam, American Geophysical Union Fall Meeting, abstract #P41B-1281.

Carr, M. H. (1981). *The Surface of Mars*, 226 pp., Yale Univ. Press, New Haven, Conn.

Christensen, P. R. and Moore, H. J. (1992). The martian surface layer. In *Mars,* eds. H. H. Kieffer, B.M. Jakosky, C.W. Snyder, and M.S. Matthews, Univ. of Arizona Press, Tucson, pp. 686-729.

Christensen, P. R., Wyatt, M. B., Glotch, T. D., *et al.* (2004). Mineralogy at Meridiani Planum from the Mini-TES Experiment on the Opportunity Rover. *Science*, **306**, 1733- 1739.

Christensen, P. R., Bandfield, J. L., Clark, R. N., *et al.* (2000). Detection of crystalline hematite mineralization on Mars by the Thermal Emission Spectrometer: Evidence for near-surface water. *J. Geophys. Res.,* **105***, E4*, 9623-9642.

Clark, B. C., Morris, R. V., McLennan, S. M., *et al.* (2005). Chemistry and mineralogy of outcrops at Meridiani Planum. *Earth Plan. Sci. Lett.*, **240**, 73-94.

Clark, R. N. and Roush, T. L. (1984). Reflectance spectroscopy: Quantitative analysis techniques for remote sensing applications. *J. Geophys. Res.* **89***,* 6329-6340.

Cloutis, E. A. and Bell III, J. F. (2003). Mafic silicate mapping on Mars: Effects of palagonite, multiple mafic silicates, and spectral resolution. *Icarus,* **172***,* 233-254.

Cloutis, E. A., Hawthorne, F. C., Mertzman, S. A., *et al.* (2006). Detection and discrimination of sulfate minerals using reflectance spectroscopy. *Icarus,* **184***,* 121-157.

Cloutis, E. A., Gaffey, M. J., Jackowski, T. L., and Reed, K. L. (1986). Calibration of phase abundance, composition, and particle size distribution for olivine-orthopyroxene mixtures from reflectance spectra. *J. Geophys. Res.,* **91***,* 11641-11653.

Crowley, J. K., Williams, D. E., Hammarstrom, M. J., Piatak, N., I-Ming Chou, J.C. (2003). Mars, Spectral reflectance properties (0.4-2.5 μm) of secondary Fe-oxide, Fe-hydroxide, and Fe-sulphate-hydrate minerals associated with sulphide-bearing mine wastes. *Geochemistry: Exploration, Environment, Analysis*, **3**, 219-228.

Crumpler, L. S., Squyres, S. W., Arvidson, R. E., *et al.* (2005). Mars Exploration Rover Geologic traverse by the Spirit rover in the Plains of Gusev Crater, Mars. *Geology,* **33***,* 809–812.

Crumpler, L. S., McCoy, T., Schmidt, M., and the Athena Science Team (2007). Spirit: Observations of very vesicular basalts in the Columbia Hills, Mars and significance for primary lava textures, volatiles, and paleoenviroment (abstract)**.** *Lunar Planet. Sci.* **38**.

Farrand, W. F., Bell III, J. F., Johnson, J. R., *et al.* (2006). Visible and Near Infrared multispectral analysis of in situ and displaced rocks, Meridiani Planum, Mars by the Mars Exploration Rover Opportunity: Spectral properties and stratigraphy, in press, *J. Geophys. Res*.

Farrand, W. H., Bell III, J. F., Johnson, J. R., *et al.* (2006). Visible and Near Infrared multispectral analysis of rocks at Meridiani Planum, Mars by the Mars Exploration Rover Opportunity. *JGR Planets* Special Issue on MER Opportunity. Submitted June 2006.

Farrand, W. H., Bell III, J. F., Johnson, J. R., Bishop, J. L., and Morris, R. V. (2007). "Multispectral imaging from Mars Pathfinder." Chapter 12 in *The Martian Surface: Composition, Mineralogy, and Physical Properties*, ed. J. F. Bell III, Cambridge University Press, in press.

Farrand, W. H., Bell III, J. F., Johnson, J. R., Squyres, S. W., Soderblom, J., Ming, D. W. (2006). Spectral variability among rocks in visible and near infrared multispectral Pancam data collected at Gusev Crater: Examinations using spectral mixture analysis and related techniques. *J. Geophys. Res.: Planets*, **111**, E02S15, doi: 10.1029/2005JE002495.

Fergason, R. L., Christensen, P. R., Bell III, J. F., Golombek, M. P., Herkenhoff, K. E., and Kieffer, H. H. (2006). Physical properties of the Mars Exploration Rover landing sites as inferred from Mini-TES derived thermal inertia. *J. Geophys. Res.,* **111***,* E02S21, doi:10.1029/2005JE002583.

Fischer, E., and Pieters, C. (1993). The continuum slope of Mars: Bi-directional reflectance investigations and applications to Olympus Mons. *Icarus*, **102**, 185-202.

Gaffey, M. J. (1976). Spectral reflectance characteristics of the meteorite classes. *J. Geophys. Res., **81***, 905-920.

Gellert, R., Rieder, R., Anderson, R. C., *et al.* (2004). Chemistry of Rocks and Soils in Gusev Crater from the Alpha Particle X-ray Spectrometer. *Science,* **305***,* 829-832.

Gellert, R., Rieder, R., Brückner, J., *et al.* (2006). Alpha particle X-ray spectrometer (APXS): Results from Gusev crater and calibration report. *J. Geophys. Res.,* **111**, E02S05, doi:10.1029/2005JE002555.

Gellert *et al.*, (2007). JGR paper on Meridiani APXS results.

Gillespie, A., Kahle, A. and Walker, R. (1987). Color Enhancement of Highly Correlated Images. I. Decorrelation and HIS Contrast Enhancement. *Rem. Sens. Env.,* **20***,* 209-235.

Goetz, W., Bertelsen, P., Binau, C. S., *et al.* (2005). Chemistry and mineralogy of atmospheric dust at Gusev crater. Indication of dryer periods on Mars. *Nature*, **436**, 62-65.

Golombek, M.P, *et al.* (1999). Overview of the Mars Pathfinder mission: Launch through landing, surface operations, data sets, and science results. *J. Geophys. Res.,* **104***,* 8523-8554.

Golombek, M. P., Arvidson, R. E., Bell III, J. F., *et al.* (2005). Assessment of Mars Exploration Rover landing site predictions. *Nature,* **436***,* 44-48.

Golombek, M.P. *et al*. (2006). Geology of the Gusev cratered plains from the *Spirit* rover traverse. *J. Geophys. Res.,* **111***,* E02S07, doi:10.1029/2005JE002503.

Grant, J. A., Arvidson, R., Bell III, J. F., *et al.* (2004). Surficial Deposits at Gusev Crater Along Spirit Rover Traverses. *Science,* **305***,* 807-810.

Greeley, R. and Iversen, J. D. (1985). *Wind as a Geological Process,* 333 pp., Cambridge Univ. Press, New York.

Greeley, R., Arvidson, R. E., Barlett, P. W., *et al.* (2006a). Gusev crater: wind-related features and processes observed by the Mars Exploration Rover, *Spirit. J. Geophys. Res.,* **111**, doi:10.1029/2005JE002491.

Greeley, R., Whelley, P. L., Arvidson, R. E., *et al.* (2006b). Active dust devils in Gusev Crater, Mars: observations from the Mars Exploration Rover, *Spirit. J. Geophys. Res,* **111***,* E12S09, doi:10.1029/2006JE002743.

Greeley, R., Arvidson, R., Bell III, J. F., *et al.* (2005). Martian variable features: new insight from the Mars Express orbiter and the Mars Exploration Rover, Spirit. *J. Geophys. Res.,* **110***,* doi:10.1029/2005JE002403.

Greeley, R., Kuzmin, R. O., Rafkin, S. C. R., Michaels, T., and Haberle, R. M. (2003). Wind-related features in Gusev Crater, Mars. *J. Geophys. Res.,* **108**, doi:10.1029/2002JE002006.

Greeley, R., Squyres, S. W., Arvidson, R. E., *et al.* (2004). Wind-related processes detected by the Spirit Rover at Guzev Crater, Mars. *Science,* **305***,* 810-821.

Grotzinger, J., Bell III, J. F., Herkenhoff, K., *et al.* (2006). Sedimentary textures formed by aqueous processes, Erebus crater, Meridiani Planum, Mars. *Geology, **34***, 1085–1088; doi: 10.1130/G22985A.1.

Grotzinger, J. P., Bell III, J. F., Calvin, W., *et al.* (2005). Stratigraphy, Sedimentology and Depositional Environment of the Burns Formation, Meridiani Planum, Mars. *EPSL* **240**, 11-72.

Herkenhoff, K. E. *et al.* (2006). Overview of the Microscopic Imager investigation during *Spirit's* first 450 sols in Gusev crater. *J. Geophys. Res.,* **111**, E02S04, doi:10.1029/2005JE002574.

Herkenhoff, K. E., Golombek, M. P., Guinness, E. A., *et al.* (2007). *In-situ* observations of the physical properties of the martian surface. Chapter 20 in *The Martian Surface: Composition, Mineralogy, and Physical Properties*, ed. J. F. Bell III, Cambridge University Press, in press.

Herkenhoff, K. E., Squyres, S. W., Arvidson, R., *et al.* (2004). Textures of the Soils and Rocks at Gusev Crater from Spirit's Microscopic Imager. *Science,* **305**, 824-826.

Huck, F. O., Taylor, G. R., McCall, H. F., Patterson, W. R. (1975). The Viking Mars lander camera. *Space Science Instrumentation,* **1**, 189-241.

Johnson, D. L. (1968). Lunar soil: Should this term be used? *Science,* **160**, 1258.

Johnson, J. R. and Grundy, W. M. (2001).Visible/near-infrared spectra and two-layer modeling of palagonite-coated basalts. *Geophys. Res. Lett.*, **28**, 2101-2104.

Johnson, J. R., Staid, M., Bell III, J. F., *et al.* (2007). Mineralogic constraints on sulfur-rich soils from Pancam spectra at Gusev crater, Mars. Submitted *to Geophys. Res. Lett*.

Johnson, J. R., Sohl-Dickstein, J., Grundy, W. M., *et al.* (2006). Radiative transfer modeling of dust-coated Pancam calibration target materials: Laboratory visible/near-infrared spectrogoniometry. *J. Geophys. Res.,* **111**, E12S07, doi:10.1029/2005JE002658.

Johnson, J. R., Grundy, W. M., and Shepard, M. K. (2004). Visible/near-infrared spectrogoniometric observations and modeling of dust-coated rocks. *Icarus*, **171**, 546-556.

Johnson, J. R., Kirk, R., Soderblom, L. A., *et al.* (1999). Photometric properties of materials at the Sagan Memorial Station, Mars. *J. Geophys. Res.,* **104**, 8809-8830.

Jolliff, B. L. and the Athena Science Team (2005). Composition of Meridiani hematite-rich spherules: A mass-balance mixing-model approach. *Lunar Planet. Sci*., **36**, #2269.

Jolliff, B. L., and McLennan, S. M. (2006). Evidence for water at Meridiani. *Elements,* **2**, 163-167.

Jolliff, B., Knoll, A., Farrand, W., and Sullivan, R. (2006a). Rock Rinds at Meridiani and Surface Weathering Phenomena. American Geophysical Union Fall Meeting, abstract #P43A-03.

Jolliff, B. L., Farrand, W. H., Johnson, J. R., Schröder, C., and Weitz, C. M. (2006a). Origin of rocks and cobbles on the Meridiani plains as seen by Opportunity. *Lunar Planet. Sci*., **37**, #2401.

Jolliff B. L., Gellert, R., and Mittlefehldt, D. W. (2007). More on the possible composition of the Meridiani hematite-rich concretions. *Lunar Planet. Sci*., **38**, #2279.

Kasting, J. F., Brown, L. L., and Acord, J. M (1992). Was early Mars warmed by ammonia? Workshop on the Martian Surface and Atmosphere Through Time, p 84-85 (N92-28988 19-91).

Kinch, K. J., Sohl-Dickstein, J., Bell III, J. F., Johnson, J. R., and Goetz, W. (2006). Radiative transfer analysis of dust deposition on the Mars Exploration Rover Panoramic Camera (Pancam) calibration targets. *J. Geophys. Res.,* in press.

Klingelhöfer, G., and Morris, R. V. (2007). MER Mössbauer results. Chapter 15 in *The Martian Surface: Composition, Mineralogy, and Physical Properties*, ed. J.F. Bell III, Cambridge University Press, in press.

Klingelhöfer, G., Morris, R. V., Bernhardt, B., *et al.* (2004). Jarosite and hematite at Meridiani Planum from Opportunity's Mössbauer spectrometer. *Science*, **306**, 1740-1745.

Knauth, L. P., Burt, D. M., and Wohletz, K. H. (2005). Impact origin of sediments at the Opportunity landing site on Mars. *Nature*, **438**, 1123-1128.

Knoll, A. H., Carr, M., Clark, B., *et al.* (2005). An astrobiological perspective on Meridiani Planum. *Earth and Plan. Sci. Lett.,* **240**, 179-189.

Knoll, A. *et al.* (2007). Rinds and fracture fills at Meridiani Planum, Mars. In prepration for *J. Geophys. Res*.

Lane, M. D., Bishop, J. L., Parente, M., Dyar, M. D., King, P. L., and Cloutis, E. (2006). Determining the chemistry of the bright Paso Robles soils on Mars using multispectral data sets. Workshop on Martian Sulfates as Recorders of Atmospheric-Fluid-Rock Interactions, October 22-24, 2006 in Houston, Texas. LPI Contribution No. 1331,p.48.

Lane, M. D., Bishop, J. L., Dyar, M. D., Parente, M., King, P. L., and Hyde, B. C. (2007). Identifying the Phosphate and Ferric Sulfate Minerals in the Paso Robles Soils (Gusev Crater, Mars) Using an Integrated Spectral Approach. Lunar Planet. Sci. Conf. 38th, Abstract #1338.

Lemmon, M. T. Wolff, M. J., Smith, M. D., *et al.* (2004). Atmospheric Imaging Results from the Mars Exploration Rovers: Spirit and Opportunity. *Science,* **306**, 1753-1756.

Maki, J. N., Bell III, J. F., Herkenhoff, K. E., *et al.* (2003). The Mars Exploration Rover Engineering Cameras. *J. Geophys. Res.,* (E12), 12-1 to 12-24.

Markewitz, D., Soil without life? *Nature,* **389**, 435.

Markiewicz, W. J., Sablotny, R. M., Keller, H. U., Thomas, N., Titov, D., and Smith, P. (1999). Optical properties of the Martian aerosols derived from Imager for Mars Pathfinder midday sky brightness data. *J. Geophys. Res.*, **104**, 9009-9017.

McConnochie, T. H., Bell III, J. F., Savransky, D., *et al.* (2006). Calibration and In-Flight Performance of the Mars Odyssey THEMIS Visible Imaging Subsystem (VIS) Instrument. *J. Geophys. Res.,* **111**, E06018, doi:10.1029/2005JE002568.

McCollom, T. M. and Hynek, B. M. (2005). A volcanic environment for bedrock diagenesis at Meridiani Planum on Mars. *Nature*, **438**, doi:10.1038/nature04390, 1129-1131.

McLennan, S. M., Bell III, J. F., Calvin, W. M., *et al.* (2005). Provenance and diagenesis of the evaporite-bearing Burns formation, Meridiani Planum, Mars. *Earth Planet. Sci. Lett.,* **240**, 95-121, doi:10.1016/j.epsl.2005.09.041.

McSween, H. Y., Arvidson, R. E., Bell III, J. F., *et al.* (2004). Basaltic Rocks Analyzed by the Spirit Rover in Gusev Crater. *Science,* **305**, 842-845.

McSween, H.Y., Wyatt, M. B , Gellert, R., *et al.* (2006a). Characterization and petrologic interpretation of olivine-rich basalts at Gusev Crater, Mars. *J. Geophys. Res.,* **111**, E02S10, doi:10.1029/2005JE002477.

McSween, H.Y., Ruff, S. W., Morris, R. V., *et al.* (2006b). Alkaline volcanic rocks from the Columbia Hills, Gusev crater, Mars. *J. Geophys. Res.,* **111**, E09S91, doi:10.1029/2006JE002698.

Morris, R. V., Klingelhöfer, G., Schröder, C., *et al.* (2006a). Mössbauer mineralogy of rock, soil, and dust at Gusev crater, Mars: Spirit's journey through weakly altered olivine

basalt on the plains and pervasively altered basalt in the Columbia Hills. *J. Geophys. Res.,* **111**, E02S13, doi:10.1029/2005JE002584.
Morris, R.V., Klingelhöfer, G., Schröder, C., *et al.* (2006b). Mössbauer mineralogy of rock, soil, and dust at Meridiani Planum, Mars: Opportunity's journey across sulfate-rich outcrop, basaltic sand and dust, and hematite lag deposits. *J. Geophys. Res.,* **111**, E12S15, doi:10.1029/2006JE002791.
Morris, R. V., Golden, D. C., Ming, D. W., *et al.* (2001), Phyllosilicate-poor palagonitic dust form Mauna Kea Volcano (Hawaii): A mineralogical analogue for magnetic martian dust? *J. Geophys. Res.*, **106**, 5057-5083.
Morris, R. V., Golden, D. C., Bell III, J. F., *et al.* (2000). Possible products of hydrolytic, hydrochloric, and sulfuric weathering at the Mars Pathfinder landing site: Evidence from multispectral, elemental, and magnetic data on analogue and meteorite samples. *J. Geophys. Res.,* **105**, 1757-1817.
Morris R. V., Agresti, D. G., Lauer Jr., H. V., Newcomb, J. A., Shelfer, T. D., and Murali, A. V. (1989). Evidence for pigmentary hematite on Mars based on optical, magnetic, and Mössbauer studies of superparamagnetic (nanocrystalline) hematite. *J. Geophys. Res.,* **94**, 2760-2778.
Morris, R., Lauer, H., Lawson, C., Gibson, E., Nace, G., and Stewart, C. (1985). Spectral and other physiochemical properties of submicron powders of hematite (□Fe_2O_3), maghemite (□Fe_2O_3), magnetite (Fe_3O_4), goethite (□FeOOH), and lepidocroicite (□FeOOH). *J. Geophys. Res.*, **90**, 3126-3144.
Ming, D. W., Mittlefehldt, D. W., Morris, R. V., *et al.* (2006). Geochemical and mineralogical indicators for aqueous processes in the Columbia Hills of Gusev crater, Mars. *Geophys. Res.,* **111**, doi:10.1029/2005JE002560, E02S12, 10.1029/2005JE002560.
Mustard, J. F. and Bell III, J. F. (1994). New composite reflectance spectra of Mars from 0.4 to 3.14 μm. *Geophys. Res. Lett.,* **21**, 353-356.
Mustard, J. F. and Pieters, C. M. (1987). Quantitative abundance estimates from bidirectional reflectance measurements. *J. Geophys. Res*., **92**, E617-E626.
Mutch T. A., Arvidson, R. E., Head, J. W. III, Jones, K. L., and Saunders, R. S. (1976). *The Geology of Mars*. Princeton Univ. Press, Princeton, NJ, 400 pp.
Nikiforoff, C. C. (1959). Reappraisal of the soil. *Science,* **129**, 186-196.
Parente, M., Bishop, J. L., and Bell III, J. F. (2007). Spectral Unmixing for Sulfate Identification in Pancam Images. Lunar Planet. Sci. Conf. 38th, Abstract #1338.
Patterson III, W. R., Huck, F. O., Wall, S. D., and Wolf, M. R. (1997). Calibration and performance of the Viking lander cameras. *J. Geophys. Res.,* **82**, 4391-4400.
Pollack J. B., Colburn, D. S., Flaser, F. M., Kahn, R., Carlston, C. E., and Pidek, D. (1979). Properties and effects of dust particles suspended in the Martian atmosphere. *J. Geophys. Res., 84,* 2929-2945.
Poulet, F. and Erard, S. (2004). Nonlinear spectral mixing: Quantitative analysis of laboratory mineral mixtures. *J. Geophys. Res.,* **109**, E02009.
Retallack, G. J. (1998). Life, love and soil. *Nature,* **391**, 12.
Rieder, R., Gellert, R., Anderson, R. C., *et al.* (2004). Chemistry of Rocks and Soils at Meridiani Planum from the Alpha Particle X-ray Spectrometer. *Science*, **306**, 1746-1749.
Roush T. L., Blaney, D. L., and Singer, R. B. (1993). The surface composition of Mars as inferred from spectroscopic observations. In *Remote Geochemical Analysis: Elemental*

and Mineralogical Composition, ed. C. Pieters and P. Englert, pp. 367-393. Cambridge: Cambridge Univ. Press.
Ruff, S. W. (2006). Spirit's Home Run: More Mineralogical Diversity as Observed by Mini-TES on the Traverse to and Arrival at Home Plate in the Columbia Hills of Gusev Crater, Mars. Amer. Geophys. U. Fall Meeting, Abstract #P44A-04.
Ruff, S. W., Christensen, P. R., Blaney, D. L., *et al.* (2006). The rocks of Gusev crater as viewed by the Mini-TES instrument. *J. Geophys. Res.,* **111**, E12S18, doi:10.1029/2006JE002747.
Schneider A. L., Mittlefehldt, D. W., Gellert, R., and Jolliff, B. (2007). Compositional constraints on hematite-rich spherule (blueberry) formation at Meridiani Planum, Mars. *Lunar Planet. Sci*. **38**, #xxxx.
Sharp, R. P., and Malin, M. C. (1984). Surface geology from Viking landers on Mars: A second look. *Geol. Soc. Am. Bull.*, **95**, 1398-1412.
Sherman, D. M., Burns, R.G., and Burns, V.M. (1982). Spectral characteristics of the iron oxides with application to the martian bright region mineralogy. *J. Geophys. Res.,* **87**, 10169-10180.
Singer, R. B. (1981). Near-infrared spectral reflectance of mineral mixtures: Systematic combinations of pyroxenes, olivine, and iron oxides. *J. Geophys. Res.,* **86**, 7967-7982.
Smith, P. H., Bell III, J. F., Bridges, N. T., *et al.* (1997b). First results from the Pathfinder camera. *Science,* **278**, 1758-1765.
Smith, P. H., Tomasko, M. G., Britt, D., *et al.* (1997a). The Imager for Mars Pathfinder experiment, *J. Geophys. Res., 102,* 4003-4025.
Soderblom, L. A. (1992). The composition and mineralogy of the martian surface from spectroscopic observations: 0.3-50 μm. In *Mars*, ed. H. Kieffer *et al.*, pp. 557-593. Tucson: Univ. Arizona Press.
Soderblom, L. A., Anderson, R. C., Arvidson, R. E., *et al.* (2004). Soils of Eagle Crater and Meridiani Planum at the Opportunity Rover Landing Site. *Science,* **306**, 1723-1726.
Soil Science Society of America, *Glossary of Soil Science Terms*, Madison, Wisc., 1984.
Squyres, S. W., Arvidson, R. E., Blaney, D. L., *et al.* (2006a). Rocks of the Columbia Hills. *J. Geophys. Res.,* **111**, E02S11, doi:10.1029/2005JE002562.
Squyres, S. W., Grotzinger, J. P., Arvidson, R. E., *et al.* (2004b). In Situ Evidence for an Ancient Aqueous Environment at Meridiani Planum, Mars. *Science,* **306**, 1709-1714.
Squyres, S. W., Aharonson, O., Arvidson, R. E., *et al.* (2006c). Bedrock formation at Meridiani Planum. *Nature,* **443**, E1-E2.
Squyres, S. W., Arvidson, R. E., Baumgartner, E. T., *et al.* (2003). The Athena Mars Rover Science Investigation. *J. Geophys. Res.,* **108** (E12), 8062.
Squyres, S. W., Arvidson, R. E., Bell III, J. F., *et al.* (2004a). The Spirit Rover's Athena Science Investigation at Gusev Crater, Mars. *Science,* **305**, 794-799.
Squyres, S. W., Arvidson, R. E., Bollen, D., *et al.* (2006b). Overview of the Opportunity Mars Exploration Rover Mission to Meridiani Planum: Eagle Crater to Purgatory Ripple. *J. Geophys. Res., **111***, E12S12, doi:10.1029/2006JE002771.
Sullivan, R., Banfield, D., Bell III, J. F., *et al.* (2005). Aeolian processes at the Mars Exploration Rover Meridiani Planum landing site. *Nature,* **436**, 58-61.
Thompson, S. D., Calvin, W. M., Farrand, W. H., Johnson, J. R., Bell III, J. F., and the Athena Science Team (2006). Fine scale multispectral features of sedimentary bedrock structures of Meridiani Planum, Mars. *LPSC* **37**, Abstract #1938.

Wang, A., Haskin, L. A., Squyres, S. W., *et al.* (2006). Sulfate deposition in subsurface regolith in Gusev crater, Mars. *J. Geophys. Res.*, **111**, E02S17, doi:10.1029/2005JE002513.

Weitz, C. M., Anderson, R. C., Bell III, J. F., *et al.* (2006). Soil Grain Analyses at Meridiani Planum, Mars, Mars. *J. Geophys. Res.*,**111**, E12S04, doi:10.1029/2005JE002541.

Wentworth, C. K. (1922). A scale of grade and class terms for clastic sediments. *J. Geology*, **30**, 377-392.

Wolff, M. J., Smith, M. D., Clancy, R. T., *et al.* (2006). Constraints on dust aerosols from the Mars Exploration Rovers using MGS overflights and Mini-TES. *J. Geophys. Res.*, **111**, E12S17, doi:10.1029/2006JE002786.

Yen, A. S., Mittlefehldt, D. W., McLennan, S. M., *et al.* (2006). Nickel on Mars: Constraints on meteoritic material at the surface. *J. Geophys. Res.*, **111**, E12S11, doi:10.1029/2006JE002797.

Zolotov, M. Y. and Shock, E. L. (2005). Formation of jarosite-bearing deposits through aqueous oxidation of pyrite at Meridiani Planum, Mars. *Geophys. Res., Lett.*, **32**, L21203, doi:10.129/2005GL024253.

Figure Captions:

Figure 13.1. Spirit's traverse in Gusev crater as of sol 810 (April 14, 2006). Base map from MGS/MOC (NASA/JPL/MSSS). Traverse mapping by L. Crumpler, R. Li, and the MER/Athena Science Team.

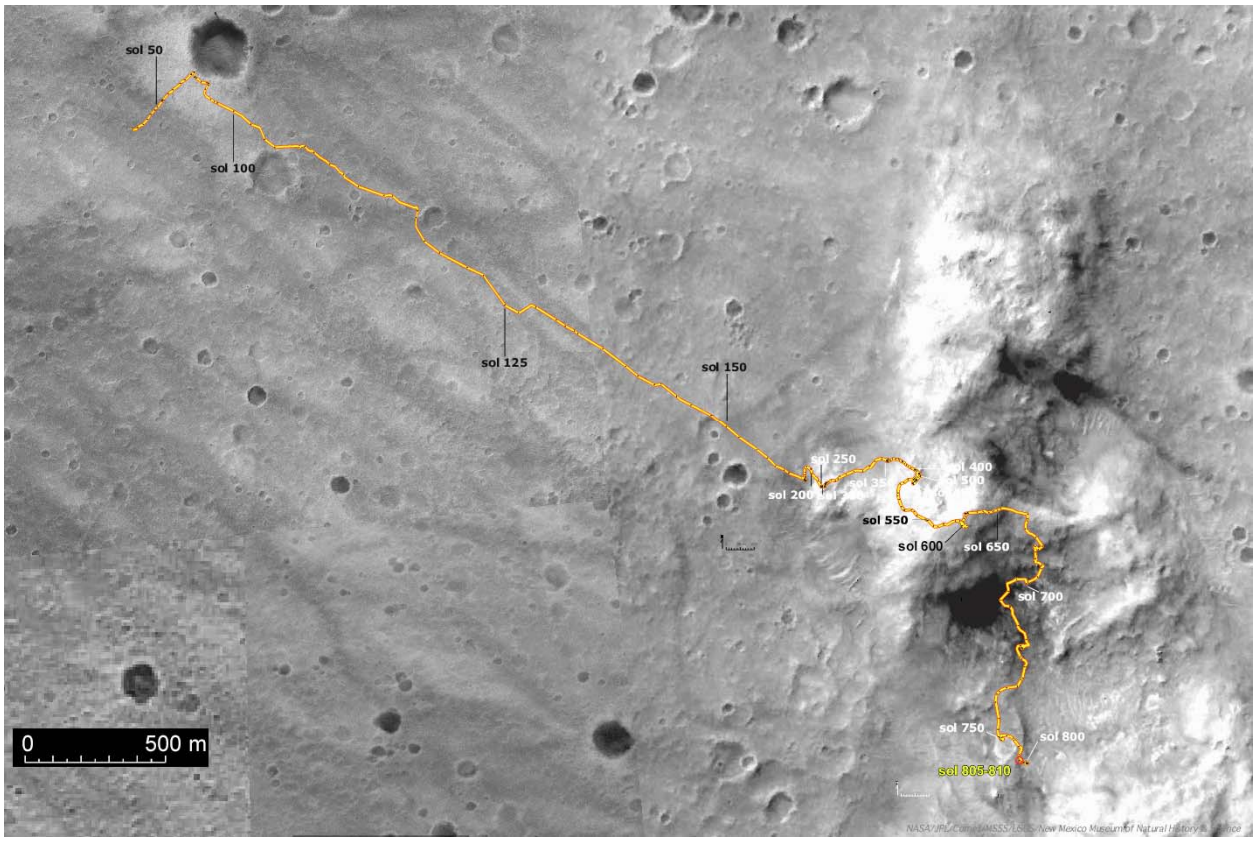

Figure 13.2. Examples of various morphologic classes/indicators that can be used to infer composition and/or physical properties of rocks at Gusev crater. (a) Angular Gusev plains rocks on the rim of Bonneville crater, subsequently identified as typical of the "Adirondack" class of hard, basaltic volcanic rocks that are ubiquitous on the plains. This is an approximate true color view of part of the sol 68-69 Pancam Bonneville crater panorama; (b) "Mimi," the first example of a friable, perhaps physically-weathered rock observed in the Gusev crater plains. Pancam sol 40 sequence P2598 approximate true color view; (c) Example of a deep RAT hole (left) and "brush flower" spot (right) on the rock Clovis in the West Spur of Husband Hill. Pancam sol 226 sequence P2569 approximate true color view. (d) The small West Spur rock Tetl, one of the first examples of layered rocks encountered in Gusev cater. Pancam sol 264 false color view from sequence P2598. (e) Examples of vesicular and platy rocks at the "Winter Haven" on Low Ridge, near Home Plate. The rock just left of center ("Allan Hills") may be an iron meteorite based on its morphology and extremely low Mini-TES infrared emissivity (see Ruff (2006) and Chapter 14 by Ruff *et al.*). Pancam sol 809 false color from sequence P2535. (f) Finely-layered outcrop rocks along the edge of Home Plate. Pancam sol 773 false color image from sequence P2456. (g) Pancam image of small, vesicular, wind-scoured rock ("Gong Gong") found near home plate. Approximate true color view from sol 736 sequence P2562.

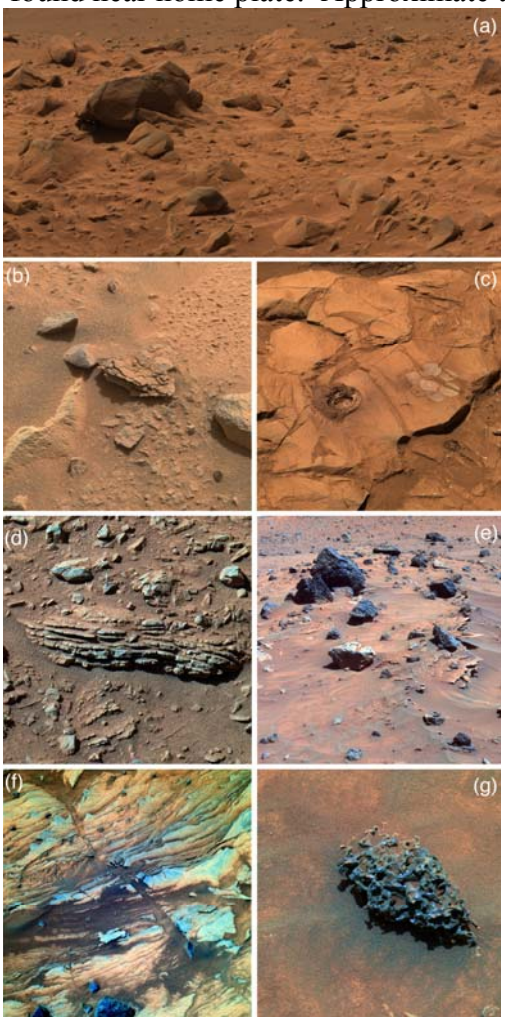

Figure 13.3. (Top). False color composite (red=673 nm, green=535 nm, blue=432 nm) of the sol 608 P2582 Whittaker/Bowline scene. **(Middle)** Composite of endmember fraction images of spectrally distinct rock and soil components (red=Bowline type rocks; green=Whittaker/Hillary (Jibsheet class) type rocks; blue=bright drift soil). **(Bottom)** Spectra of materials mapped out in the fraction image composite image. *R** is the radiance factor normalized by the solar elevation angle (Bell *et al.,* 2006b).

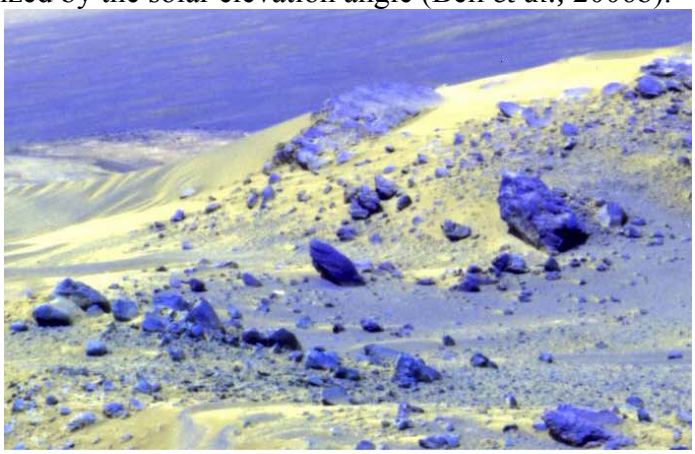

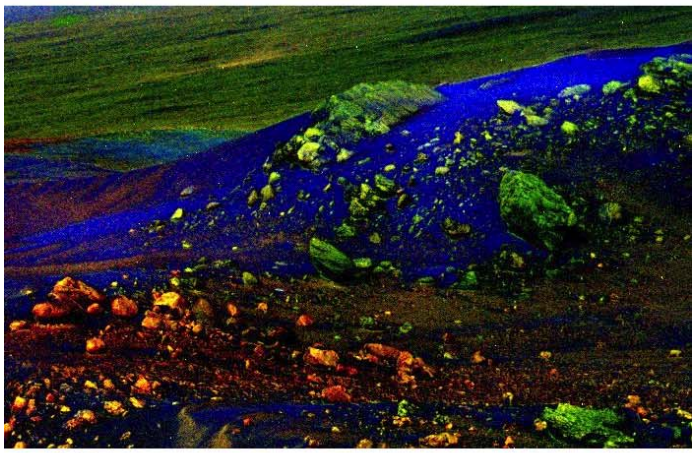

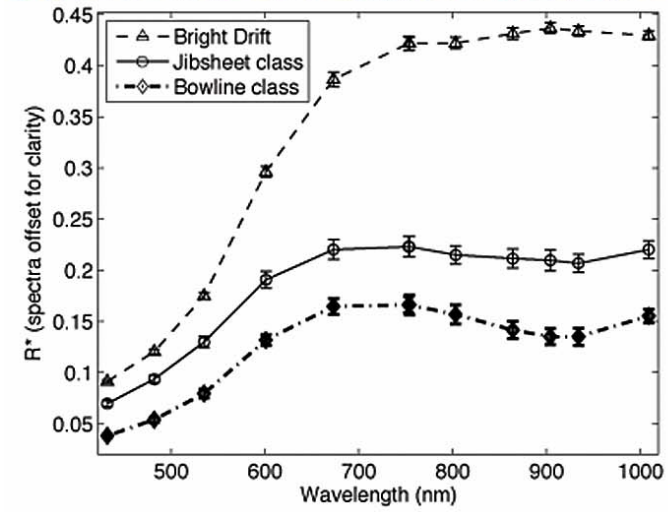

Figure 13.4. A. (top) Representative spectra of rock spectral classes described by Farrand *et al.* (2006). Peace class is not shown, but dark clasts from the Peace RAT grind were spectrally similar to the basalt spectral class. **B**. (bottom) Representative spectra of rock spectral classes observed after sol 419. Although observed at Husband Hill summit, the Bowline spectra is similar to rocks observed at the Methuselah outcrop. *R** is the radiance factor normalized by the solar elevation angle (Bell *et al.*, 2006b).

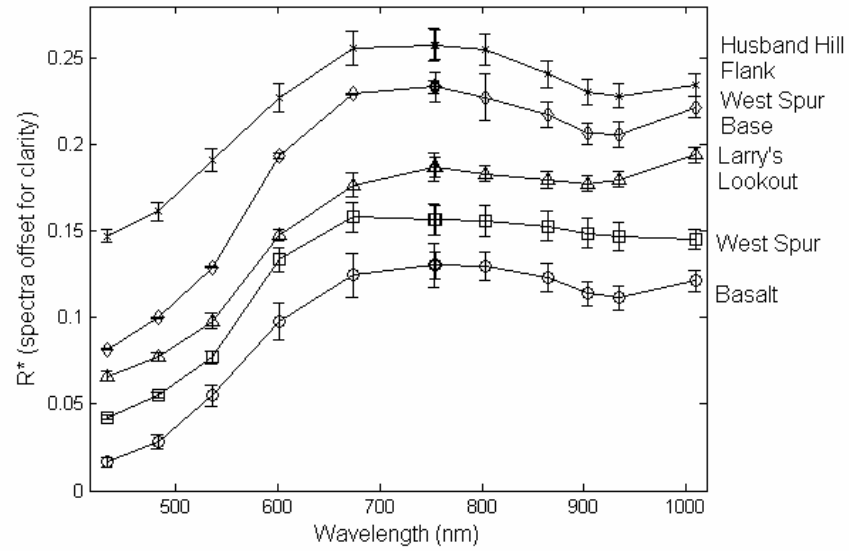

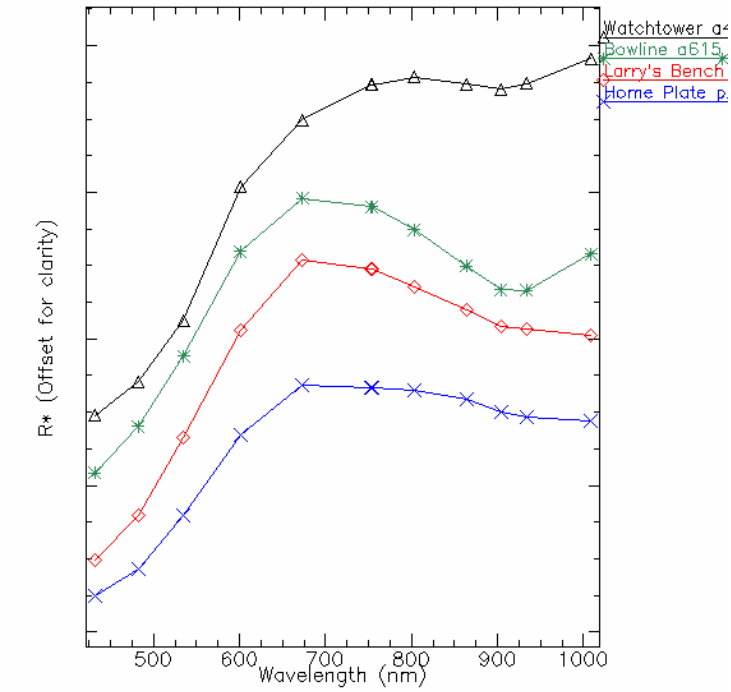

Figure 13.5. Plot of Fe^{3+} / Fe_{Total} as measured by Spirit's Mössbauer spectrometer (MB) versus 535 nm band depth for areas in the Columbia Hills that were subjected to *in situ* examinations.

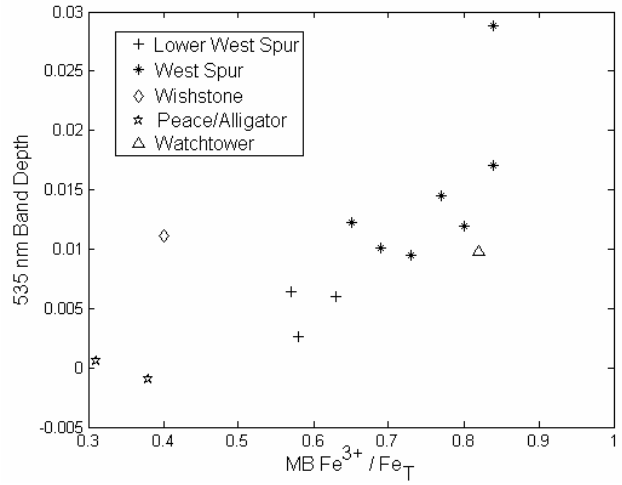

Figure 13.6. Pancam false-color images acquired using 753 nm (L2), 535 nm (L5), and 432 (L7) filters, and spectra of Home Plate outcrops: (*a*) James "Cool Papa" Bell, showing RAT brush locations Stars and Crawfords, acquired on Sol 764 at 11:48 Local True Solar Time (LTST) (P2859); (*b*) Hilton Smith acquired on Sol 770 at 12:21 LTST (P2591); (*c*) spectra derived from color-coded locations shown in (*a*); (*d*) spectra derived from color-coded locations shown in (*b*). *R** is the radiance factor normalized by the solar elevation angle (Bell *et al.*, 2006b).

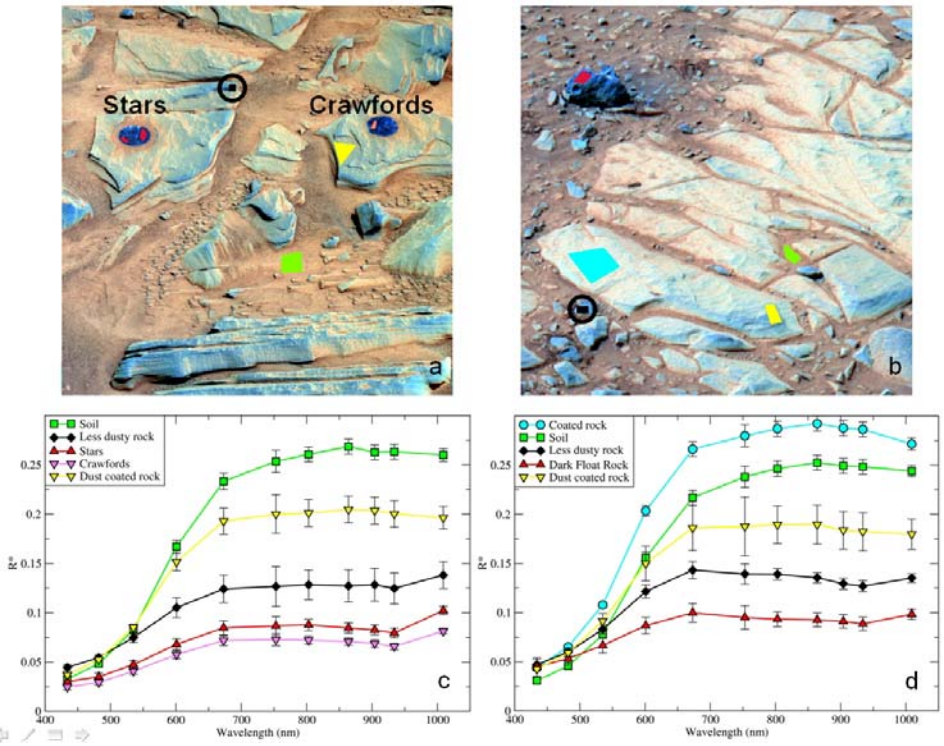

Figure 13.7. Pancam images showing examples of subsurface color variations in soil at Gusev crater. (a) Sol 72 sequence P2352 false color view of a rover wheel scuff mark into an aeolian bedform near the rim of Bonneville crater. Field of view is ~72 cm; (b) Sol 332 sequence P2440 false color view of rover tracks in West Spur soils. Field of view is ~85 cm; (c) Sol 498 sequence P2541 false color view of rover wheel scuff into an aeolian drift deposit along the "Larry's Lookout" outcrop, visited while ascending Husband Hill. Field of view is ~79 cm; (d) Sol 711 sequences P2535 and P2536 false color mosaic of rover wheel trench dug into the "El Dorado" dune field on the southern flanks of Husband Hill. Different color units appear to have been excavated by the interaction of the rover wheels and the dune sands. Field of view is ~83 cm. See also Figures 3, 11, 13, 14, and 15 for additional morphologic examples of fine-grained materials at Gusev.

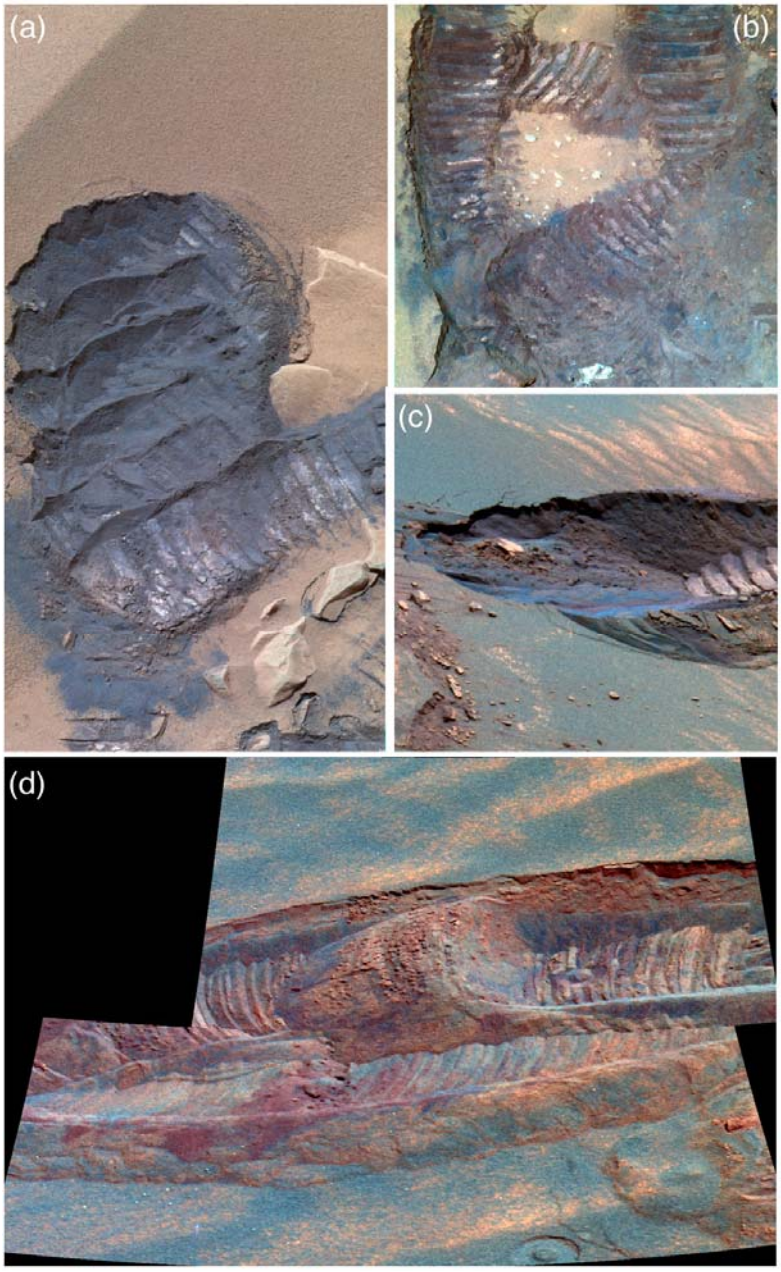

Figure 13.8. (a) Left: Representative Pancam spectra from a variety of materials in Gusev crater, and (b) Right: Meridiani Planum. These are compared to classical telescopic bright and dark region spectra (Bell *et al.*, 1990; Bell and Mustard, 1994), and to Mars Pathfinder Bright I and dark Disturbed spectra of Bell *et al.*, 2000. "Sol 68B Dark Rock" is Bounce Rock.

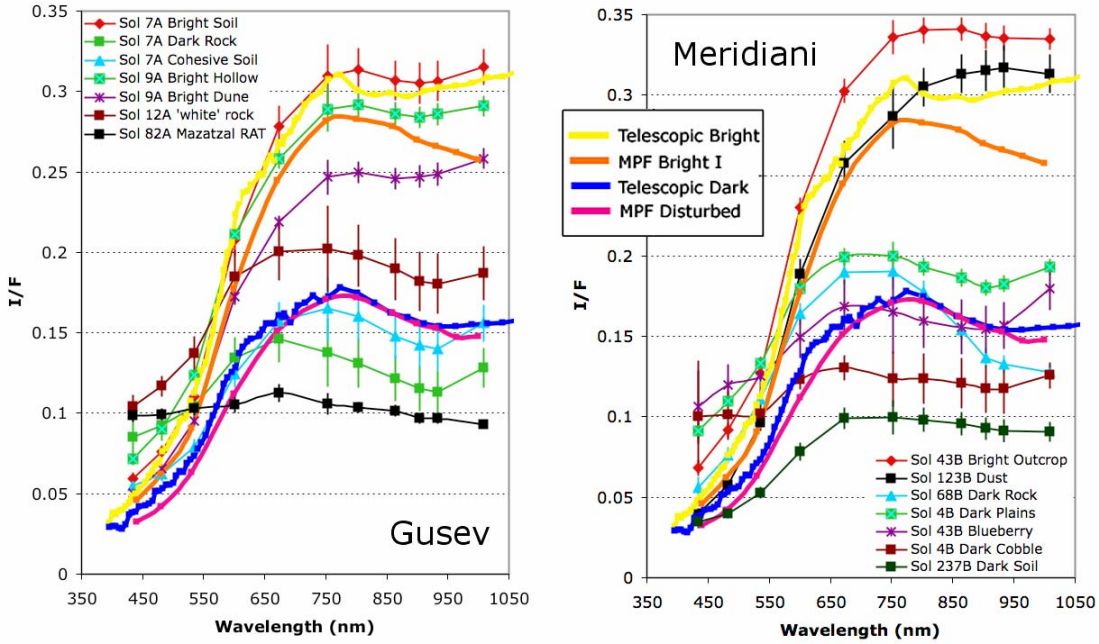

Figure 13.9. Model-derived visible to near-IR spectra of airfall dust on the Pancam calibration targets compared to Martian dust spectra from other sources (telescopic: Mustard and Bell, 1994; Mars Pathfinder bright soil MPF-23_2: Bell *et al.*, 2000; MER bright soils: Bell *et al.*, 2004a,b). Modeling and analysis described in detail in Kinch *et al.*, 2006.

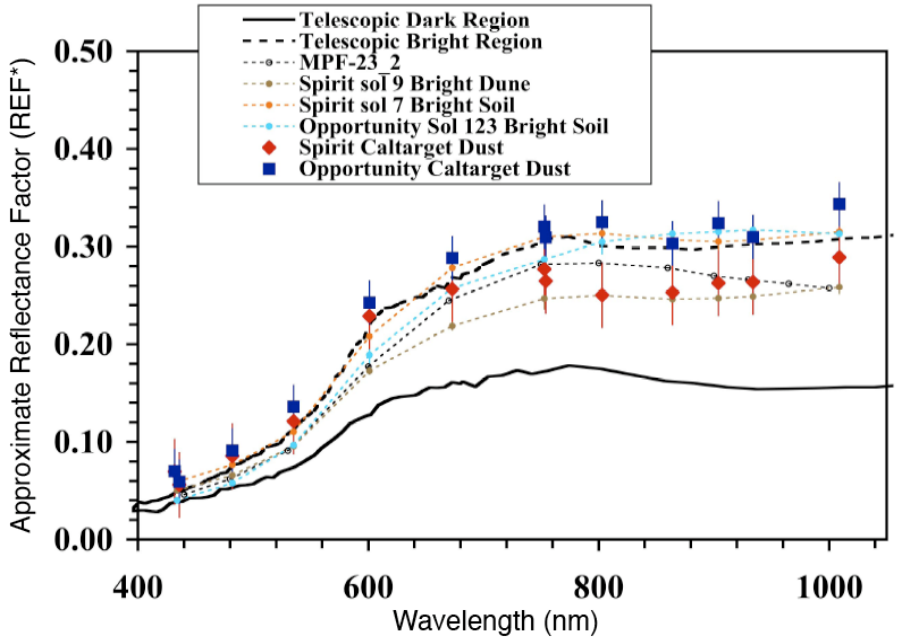

Figure 13.10. (a) Pancam spectra of grinding debris and dark, "pristine" inner rock surfaces exposed by the RAT on the Gusev plains rocks Adirondack, Humphrey, and Mazatzal. (b) Ratios of the spectra in (a) compared to laboratory-derived spectral parameterizations of olivines, pyroxenes, martian meteorites, and pyroxene-palagonite mixtures studied by Cloutis and Bell (2003). The Gusev rock spectra appear consistent with an olivine- or high-Ca-pyroxene dominated basaltic composition. Figure after McSween *et al.* (2006b).

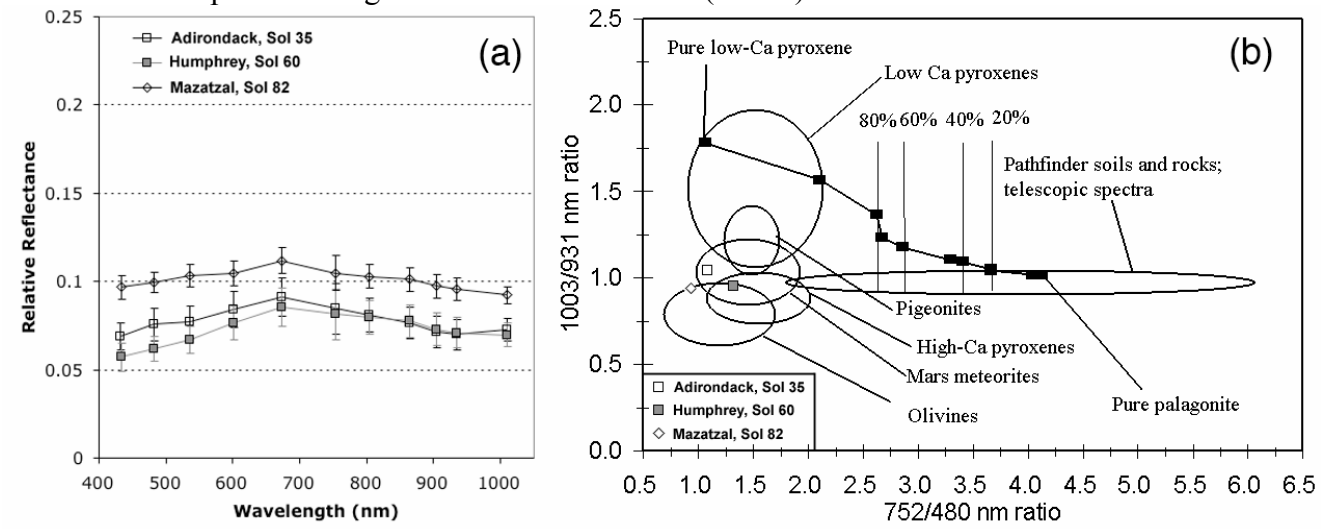

Figure 13.11. False-color (432 nm, 535 nm, 754 nm) images of (*a*) Paso Robles (Sol 400, P2551); (*b*) Arad (Sol 721, P2538); and (*c*) Tyrone (Sol 790, P2531) showing locations from which spectra were acquired. Paso Robles: red = "gray" soil, cyan = "white" soil, green = background soil. Arad: red = "white" soil, cyan = "yellow" soil, green = basaltic soil. Tyrone: red = "white" soil, cyan = "yellow" soil. From Johnson *et al.* (2007).

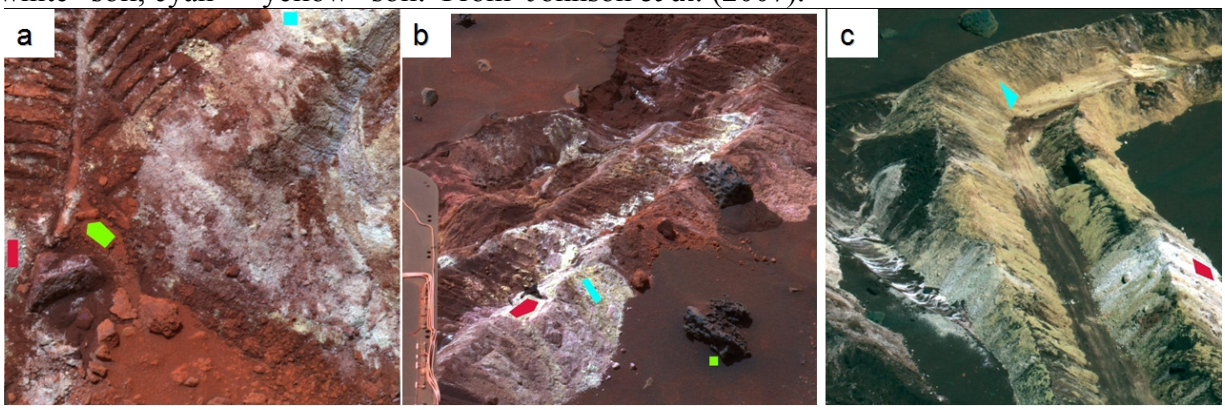

Figure 13.12. Pancam spectra (dark lines) extracted from regions of interest (ROI) shown in Figure 1; error bars are standard deviations of pixels selected for each ROI. MESMA model results (gray lines) overlain. See Table 13.2 for model results. From Johnson *et al.* (2007).

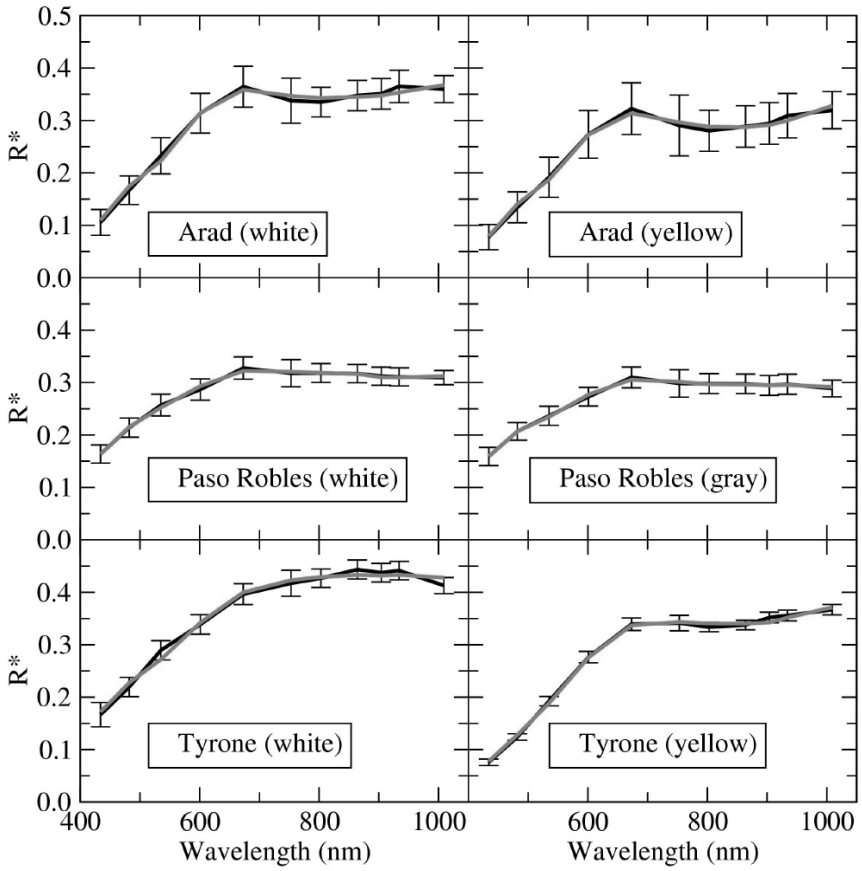

Figure 13.13. Part of the Spirit "Legacy" panorama, showing the large albedo and color contrast between the rover's tracks (albedo around 0.20) and the surrounding bright, dusty soils (albedo around 0.30) along the traverse from the landing site to the rim of Bonneville crater. This is an approximate true color rendering generated using Pancam's 753 nm, 535 nm, and 480 nm filters from *Spirit* sols 59-61 Pancam sequences P2211 through P2216.

Figure 13.14. Pancam mosaic of "Big Hole Trench", an approximately 50 cm wide by 9 cm deep furrow excavated by one of the rover's wheels in Gusev crater plains materials between Bonneville crater and the Columbia Hills. This is an approximate true color rendering generated using Pancam's 753 nm, 535 nm, and 480 nm filters from *Spirit* sol 116 Pancam sequence P2404.

Figure 13.15. (a) False color Pancam mosaic of disturbed soil and wheel tracks and crushed, "shiny" soils exposed while *Spirit* was scrambling up the West Spur of Husband Hill in a region known as Hank's Hollow. False color rendering generated using Pancam's 753 nm, 535 nm, and 480 nm filters from *Spirit* sol 170 Pancam sequence P2379. (b) Sol 483 sequence P2594 Pancam view of clasts, wind tails, and rover tracks near the summit of Husband Hill. In general, wheel tracks in the Columbia Hills exhibit less contrast with the surrounding undisturbed soils that wheel tracks in the Gusev plains. (c) Part of the sols 410 to 413 "Lookout" Pancam panorama, showing a natural color view of rover tracks during the traverse from the West Spur to the flanks of Husband Hill. The increased brightness of the tracks in views like this probably represents a photometric effect resulting from compaction of the surface and thus increased specular reflection when viewing the scene in a forward scattering (into the Sun) geometry such as this.

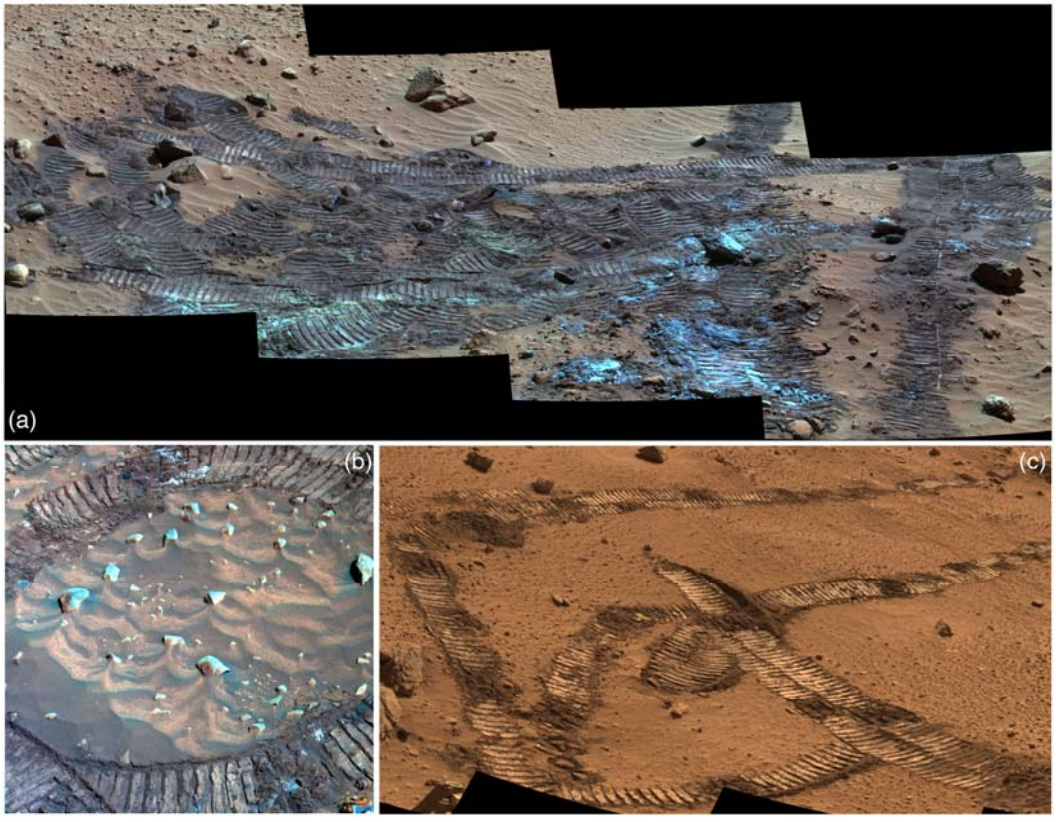

Figure 13.16. Opportunity's traverse in Meridiani Planum as of sol 810 (May 5, 2006). Base map from MGS/MOC (NASA/JPL/MSSS). Traverse mapping by T. Parker, R. Li, and the MER/Athena Science Team.

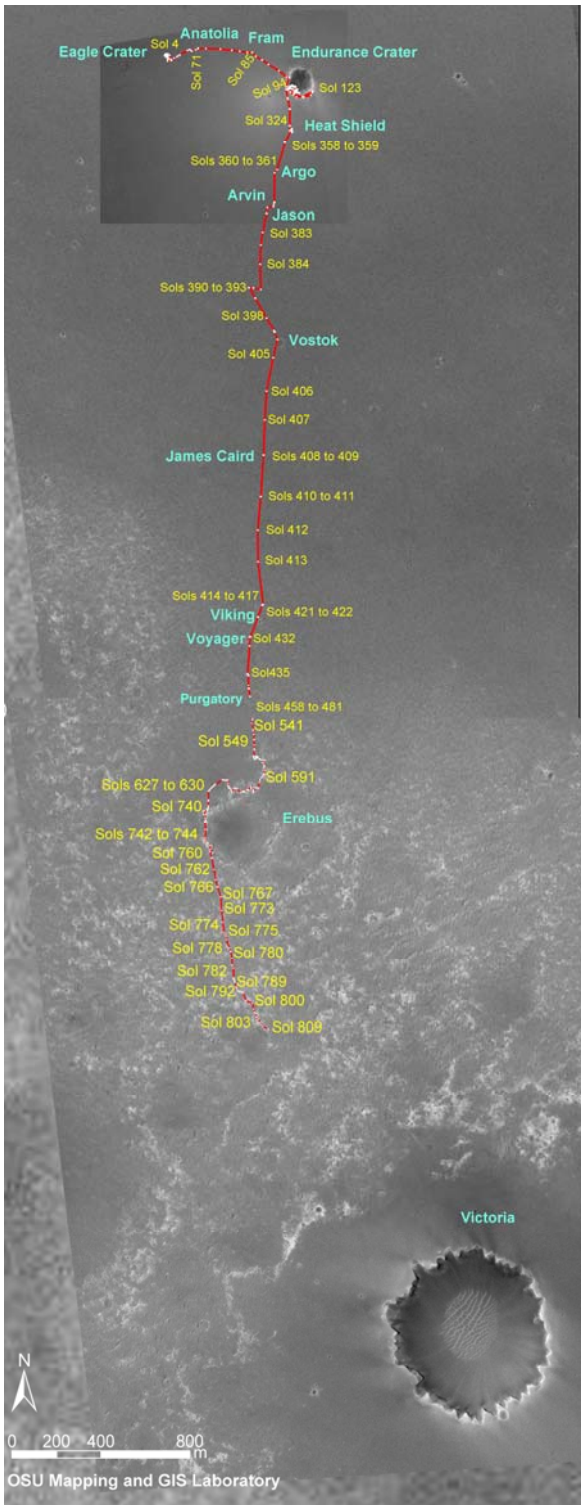

Figure 13.17. Examples showing high-resolution imaging to examine outcrop layering and sedimentary features such as lamination and crossbedding. (a) Sol 43B P2555 R1; (b) Sol 49B P2400 L7; (c) Sol 288B P2544 Super-res L6; (d) Sol 289B P2549 L7; (e) Sol 666B P2589 L7 (16:19 LTST); (f) Sol 690B P2564 L7.

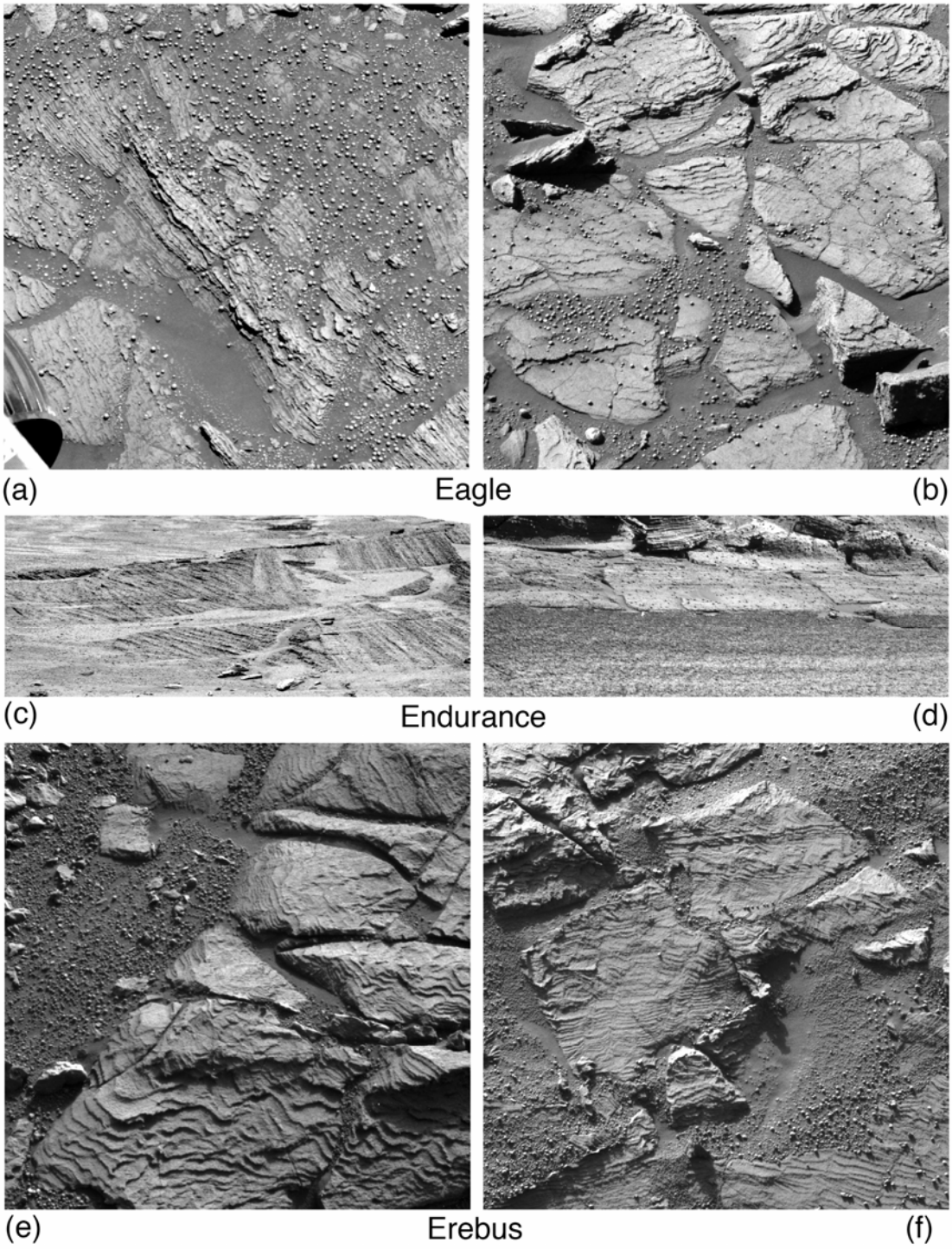

Figure 13.18. Examples of polygonal textures in rock surfaces in Endurance crater. (a) Polygonal desiccation features resembling mud cracks in the rock dubbed "Escher"; Sol 208B P2423 L2; (b) Polygonal texture resembling "septarian" fracture network possibly caused by shrinkage accompanying desiccation in rock dubbed "Wopmay"; Sol 49B P2400 L2.

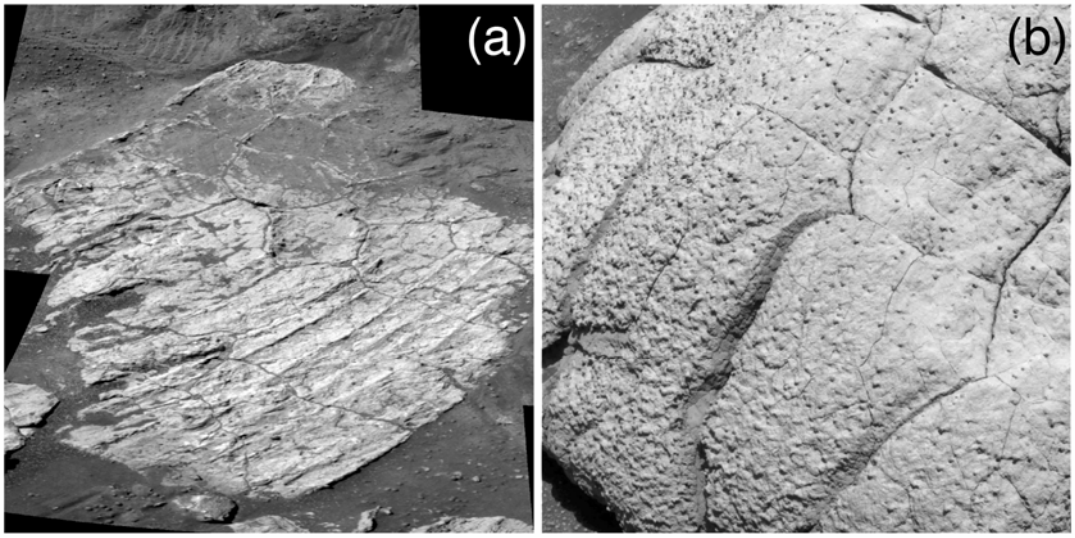

Figure 13.19. (a) Example of a fracture-lining deposit within Endurance crater rock "Razorbacks"; Sol 170B P2598 L7; (b) Example of thick rind developed on the outcrop surface of "Lemon Rind"; Sol 561B P2591 L7. In (b), the upper RAT hole is in the rind whereas the lower RAT hole is in the underlying rock.

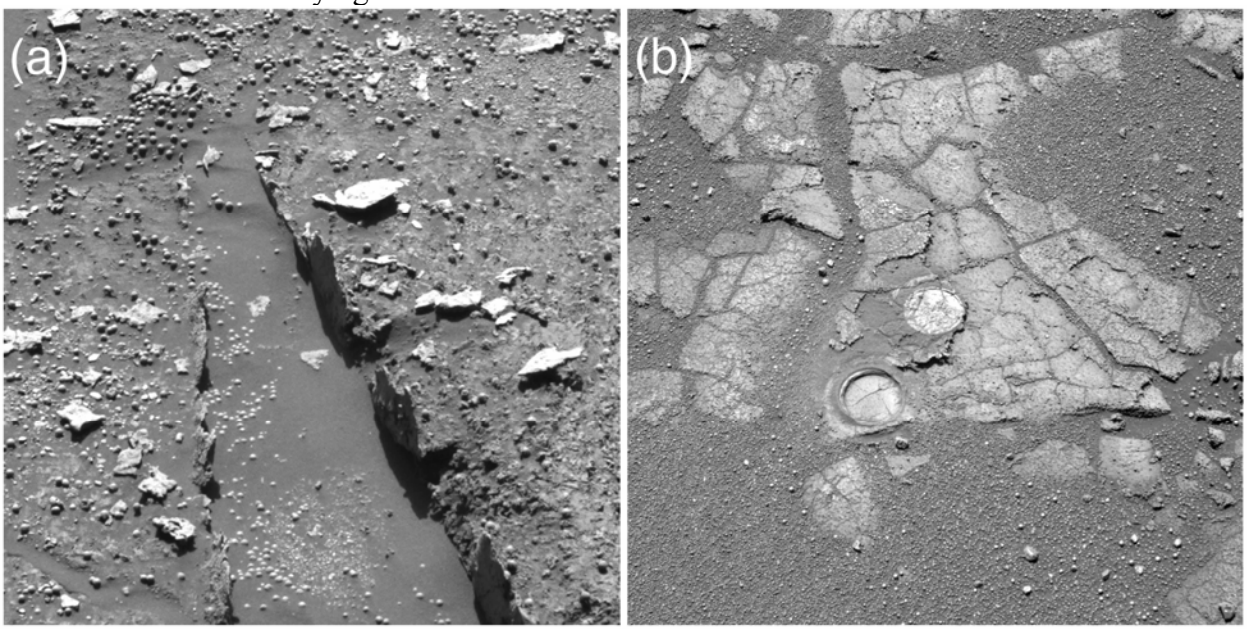

Figure 13.20. **(a)** Pancam False color RGB composite from filters L3, L5, and L7 (Table 13.1) from *Opportunity* Sol 33 P2589 image sequence on "Cathedral Dome" in Eagle crater.**(b)** Decorrelation stretch (DCS; see text) version of (a). As described in the text, the purple-colored, massive appearing section is an example of the LFS spectral class. The yellow to buff-colored lower angle portions of outcrop below and above the massive appearing section are examples of the HFS spectral class. **(c)** Approximate true color rendering of this scene (*e.g.*, Bell *et al.*, 2006b) showing that the color differences exaggerated by the false color and DCS methods in (a) and (b) would be extremely subtle to the unaided human eye. **(d)** Spectra from Eagle crater of the HFS ("buff colored") and LFS ("purple colored") spectral classes. LFS spectrum is from a rock surface in the P2575 image sequence on sol 50. HFS spectrum is from a rock surface in the P2532 image sequence on sol 37.

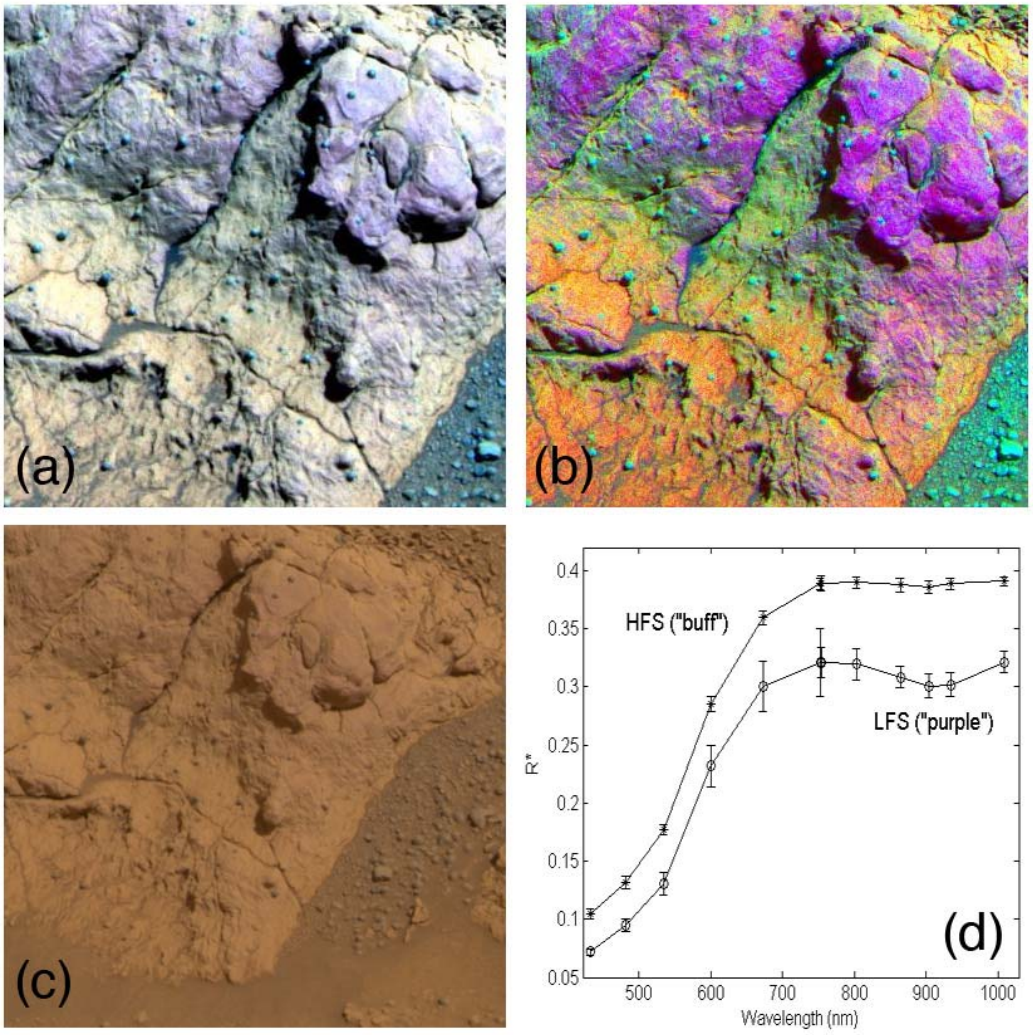

Figure 13.21. Spectra from the interiors of the Guadalupe and McKittrick RAT holes showing inherent spectral differences of different levels of the outcrop at Eagle crater. From Farrand *et al.* (2006).

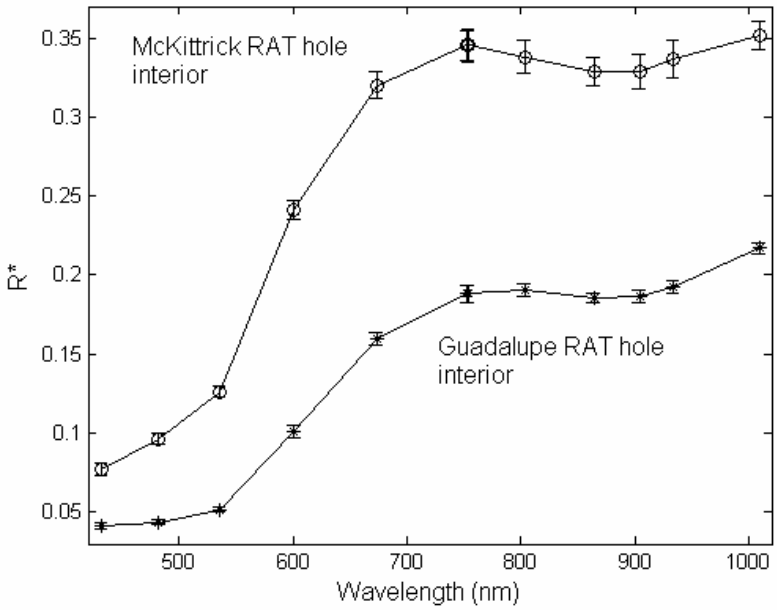

Figure 13.22. **A**. L357 composite of the RAT grind into the Guadalupe target in Eagle crater. Note the red blanket of RAT cuttings. **B**. Comparison of a laboratory spectrum of red hematite, convolved to Pancam bandpasses, and the Guadalupe RAT cuttings.

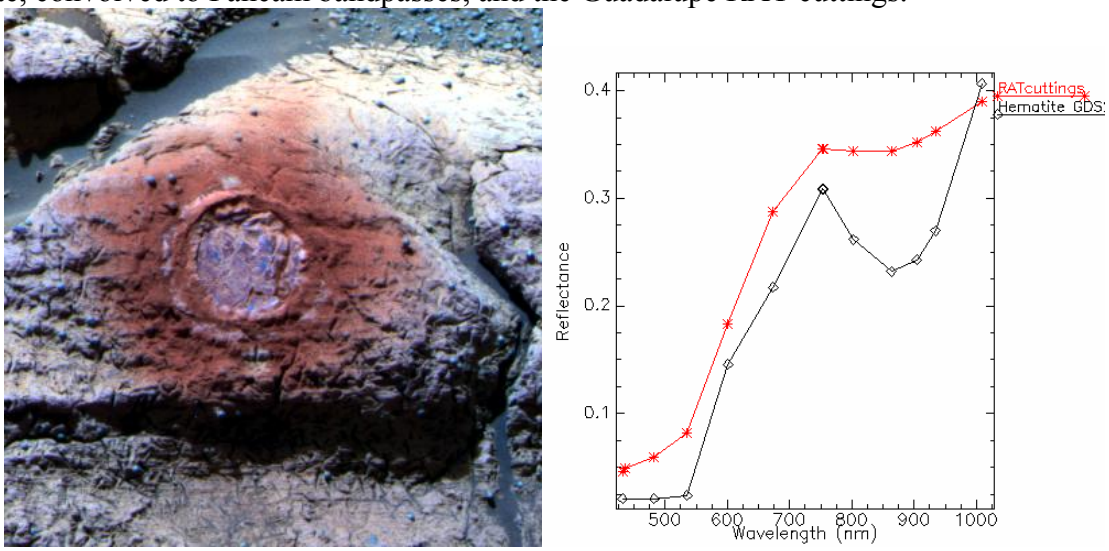

Figure 13.23. Pancam spectra of the Tennessee RAT hole and surrounding materials (Sol 140, P2500). R* is the radiance factor normalized by the solar elevation angle (Bell *et al.,* 2006). Inset is Microscopic Imager mosaic (Sol 139) showing 4.2 mm diameter spherule cut into by the RAT, whose Pancam spectrum is nearly identical to that of undisturbed spherules on the nearby soil surface. Also shown are spectra of undisturbed outcrop rock, abraded and brushed surface of the RAT hole, and tailings from the RAT grind.

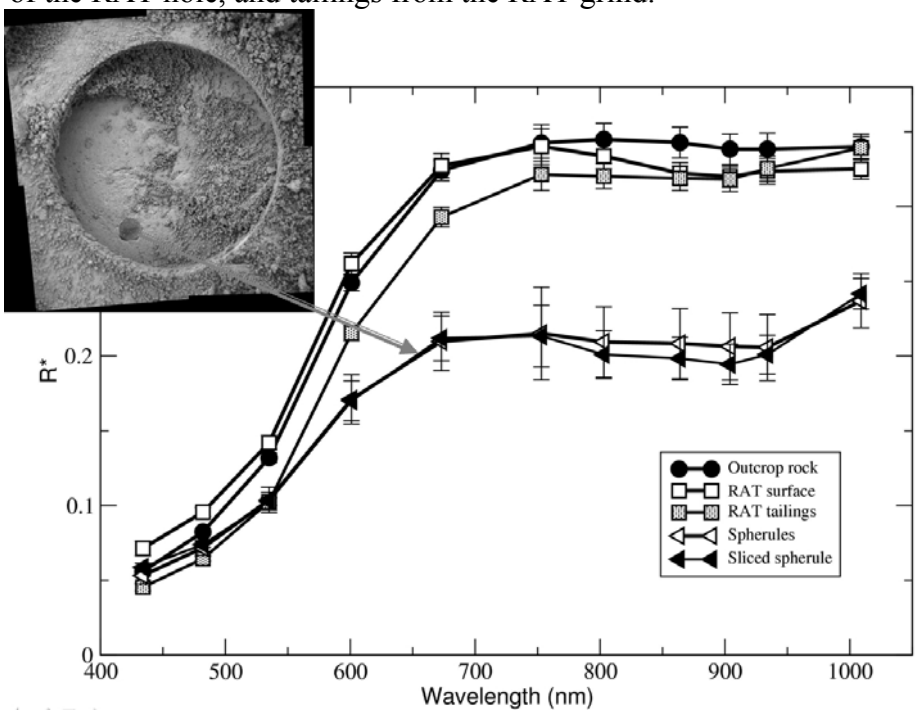

Figure 13.24. Sol 174B P2401 L257F "Backroads" observation (Farrand *et al.*, 2006). This image looks back up the pathway just inside the crater rim on the route taken by Opportunity into Endurance crater. RAT hole investigations (bright reddish circular holes here) were made into each of the distinctive strata identified with Pancam color images.

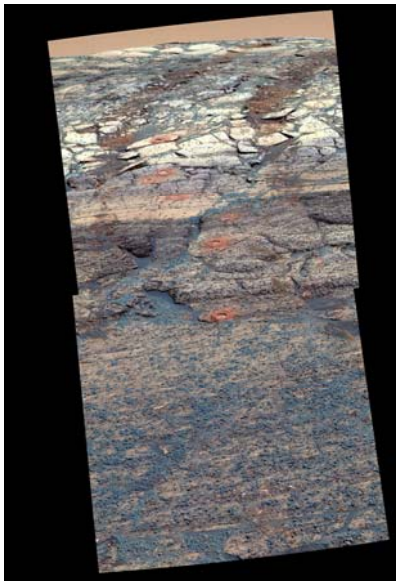

Figure 13.25. (Panel 1). Example outcrop material in approximate true color to demonstrate the exposure of sedimentary laminations. Image from sol 648 Pancam sequence P2574. Panels 2 and 3 are denoted by white frames. **(Panel 2).** Closer view of rock fragment in Panel 1 displayed here in the blue filter image (L7, 432 nm). The colors of the spectrum profiles plotted correspond to the colors of the selected pixels on the image. Error bars represent standard deviations of pixels in selected regions of interest. **(Panel 3).** Closer view of rock fragment in Panel 1 displayed here in the blue filter image (L7, 432 nm). The colors of the spectrum profiles plotted correspond to the colors of the selected pixels on the image. The dark green spectrum is a layer like the others but has a slope sign change from 673 to 753 nm unlike the other lamination plots. The two red shallow profiles are of soil and rind materials near the base of the rock; note the strong positive slope in the longer wavelength region. Error bars represent standard deviations of pixels in selected regions of interest.

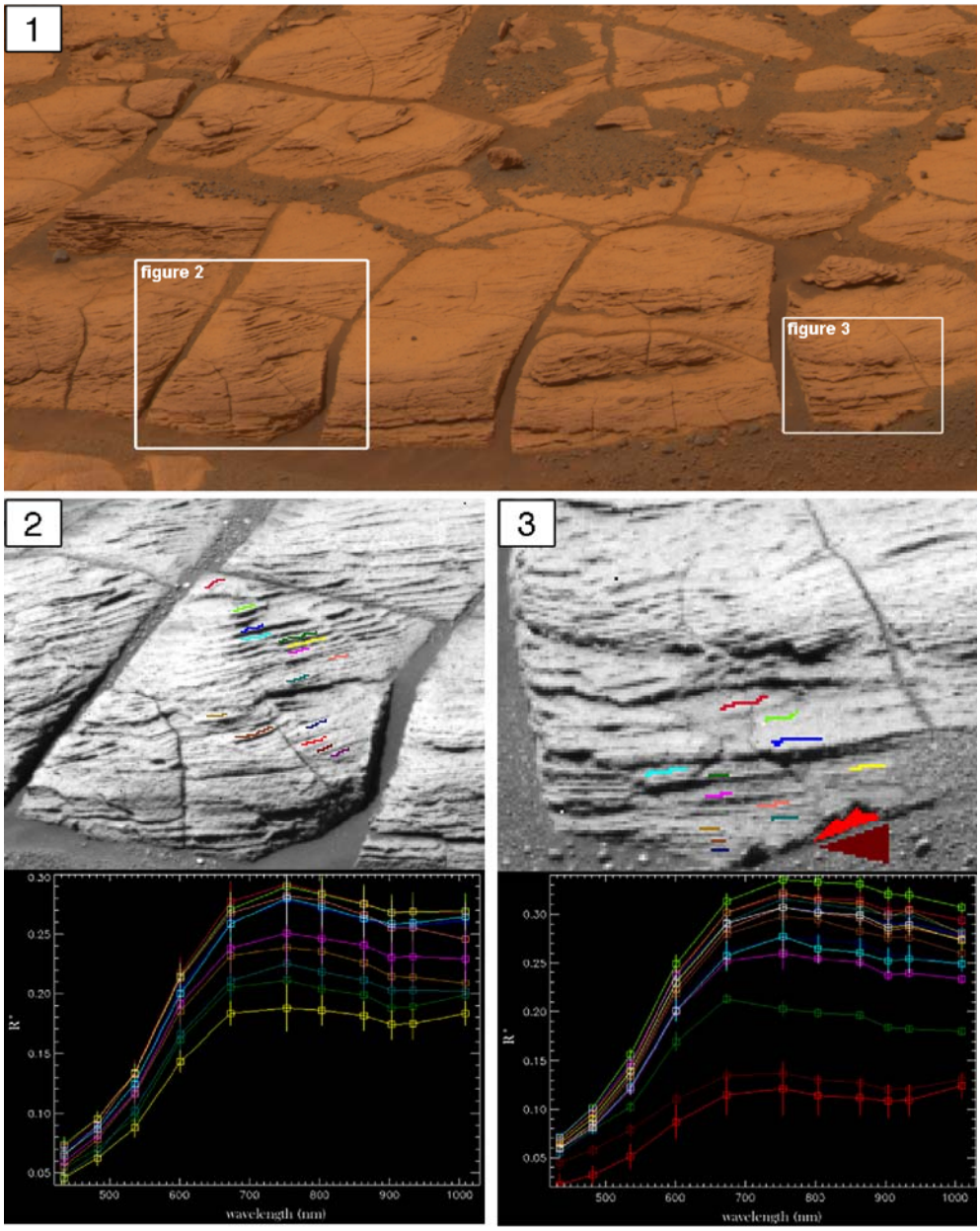

Figure 13.26. Plot of 535 nm band depth vs. 601 nm band depth for Meridiani Planum surface materials. Based on Farrand *et al.* (2006).

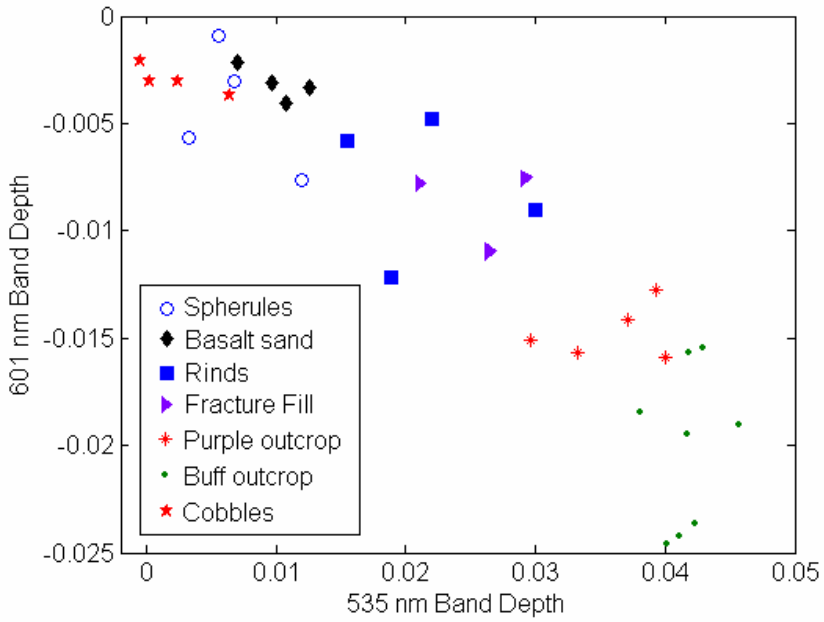

Figure 13.27. Spectra of coating/fracture fill materials from Endurance crater. An example of the "red rind" material from the Shoemakers Patio area at Eagle crater is also provided. The Sol 237 P2588 Barbeau 2 material spectrum is offset upwards by 0.02.

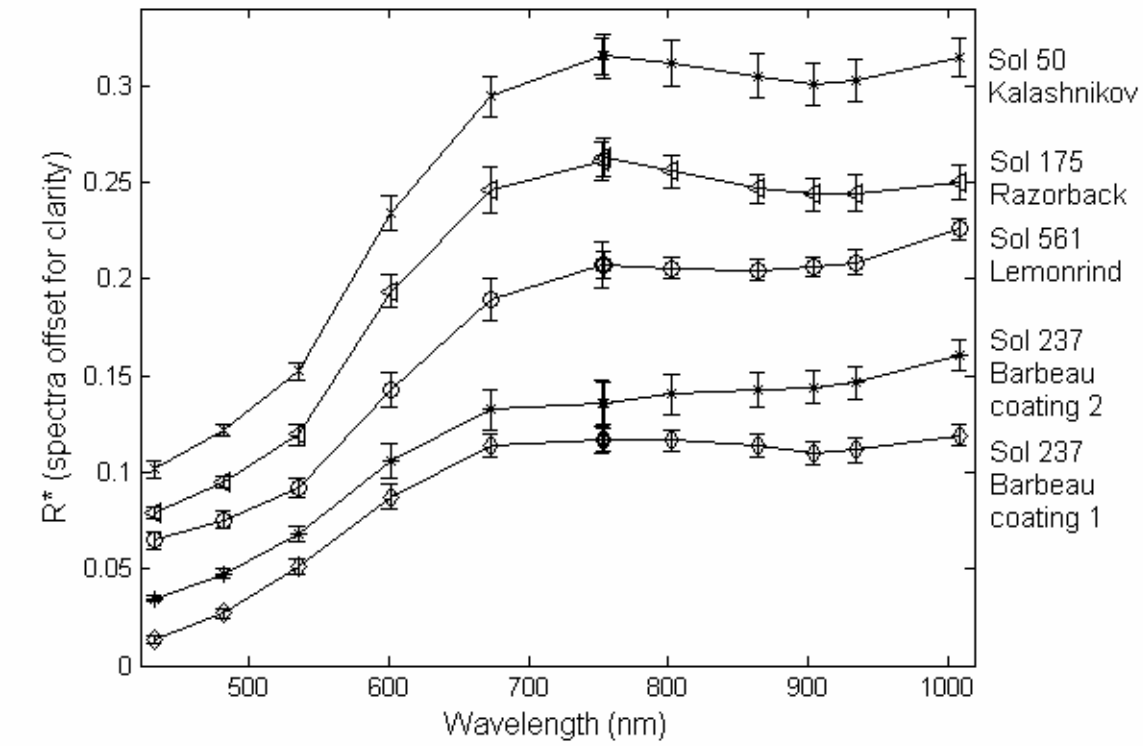

Figure 13.28. (*left*) Portion of Pancam panorama of Burns Cliff region along southern rim of Endurance Crater showing false-color composite (left) created from 754 nm, 535 nm and 432 nm images, compared to decorrelation stretch (*right*) from the same images. Yellow arrows point to fracture-fill materials observed here and along the edges of other broken outcrop blocks.

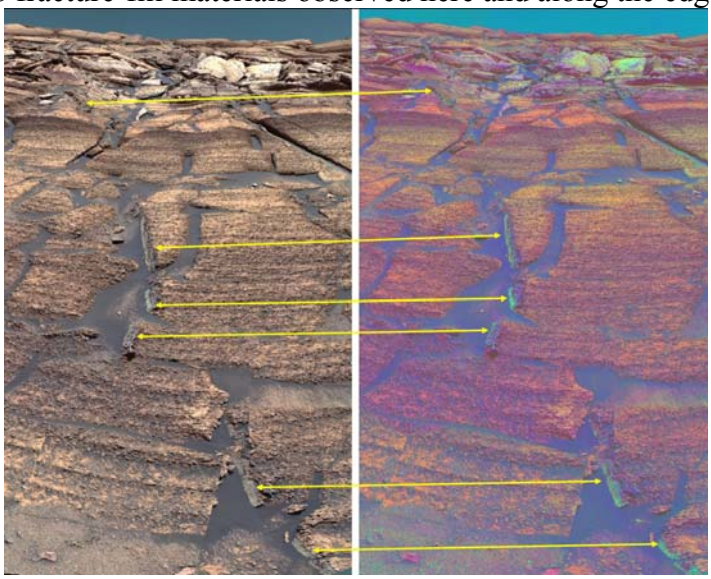

Figure 13.29. (a) Mosaic of 3 MI images (1M129426379, 1M129426503, 1M129426904) from the target "Superwit", merged with false color Pancam sol 14 sequence P2549 image derived from an RGB composite of the R2 (750 nm), R7 (1009 nm), and R1 (423 nm) filters; (b) Portion of the sol 14 Pancam Superwit observation. Pancam sequence P2549, using the same R2, R7, R1 color scheme as (a). Red box corresponds to location of MI image in part (a). Figure after Weitz *et al.* (2006).

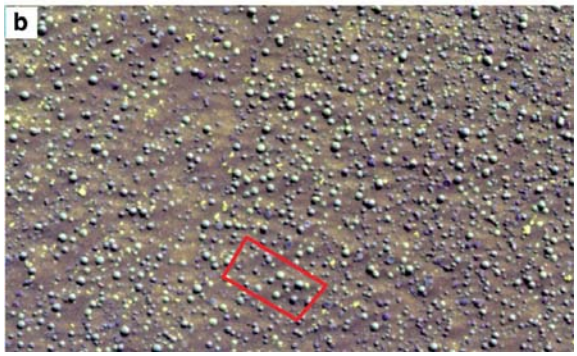

Figure 13.30. Visible to near-IR Pancam spectra of features seen in target Superwit (Figure 29). The spectrum of Ratted Spherules represents an average of two spectra from spherules that were still embedded in the Eagle crater outcrop and had been cut in half by the RAT.

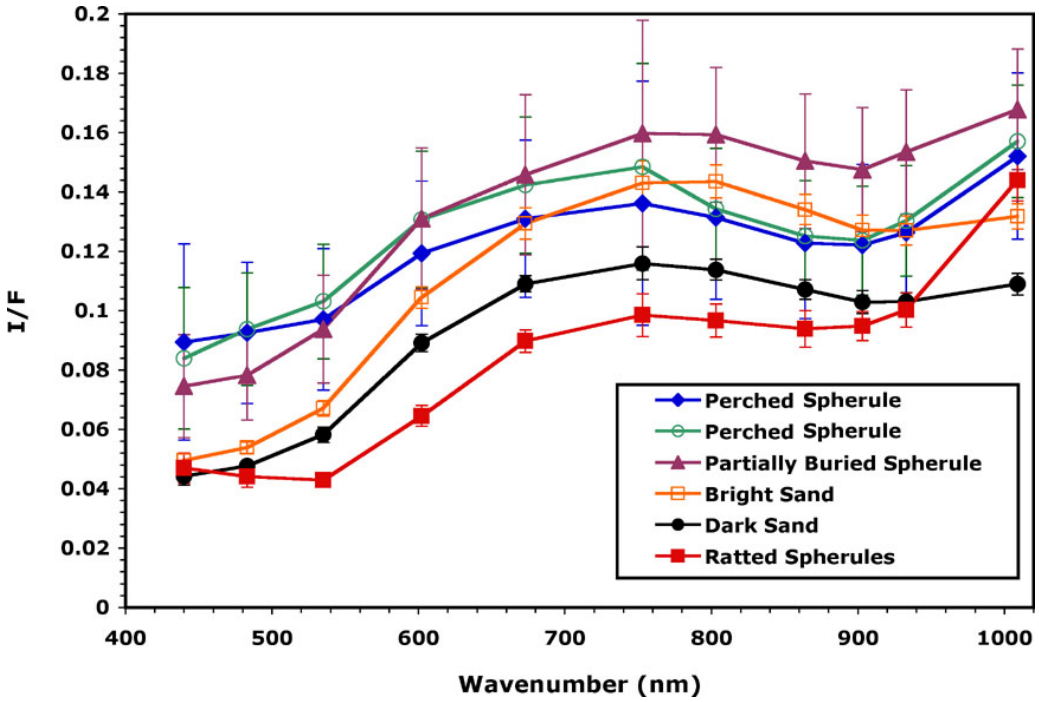

Figure13. 31. Examples of "erratics" at Meridiani Planum: (a) "Bounce Rock" – a pyroxene-rich basaltic rock thrown to its location near Eagle crater by a large impact elsewhere; Sol 65B P2574 L6; (b) "Heat Shield Rock" – an iron meteorite; Sol 346B P2591 R1.

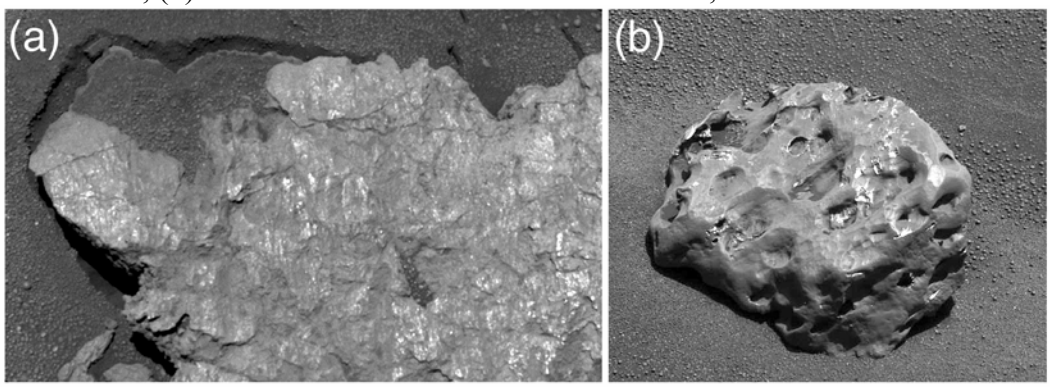

Figure 13.32. Pancam decorrelation stretch using the Right 754 nm, 934 nm, and 1009 nm filters in Red, Green, Blue, respectively. The rocks Arkansas and Perseverance are circled in yellow. The outcrop appears light-blue and light-green in color compared to the brown and red colors of the rock fragments. The top surfaces of several of the rock fragments appear green, consistent with outcrop spectral properties that could indicate a coating of fine dust derived from erosion of the outcrop. Sol 550 Pancam sequence P2579.

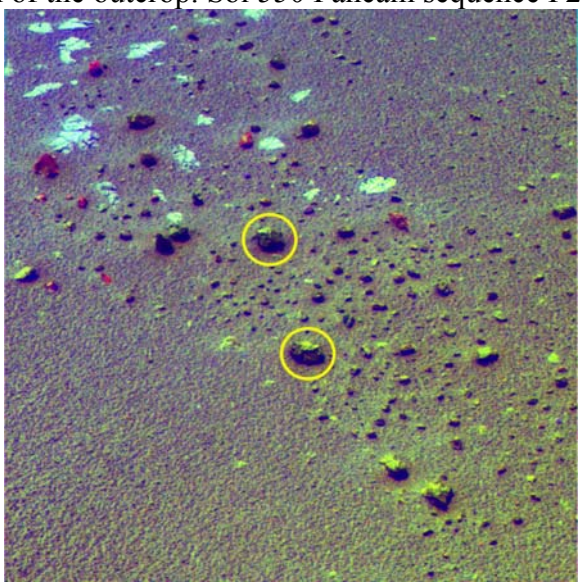

Figure 13.33. Microscopic Imager image from Sol 554 showing Perseverance cobble, with light-toned and dark-toned regions interpreted either as breccia clasts and matrix or as coated and uncoated portions of the cobble, respectively. Pancam spectra of the lighter-toned material appears similar to spectra of nearby outcrop rocks, whereas spectra of darker-toned portions appears more similar to spectra of other basaltic rocks.

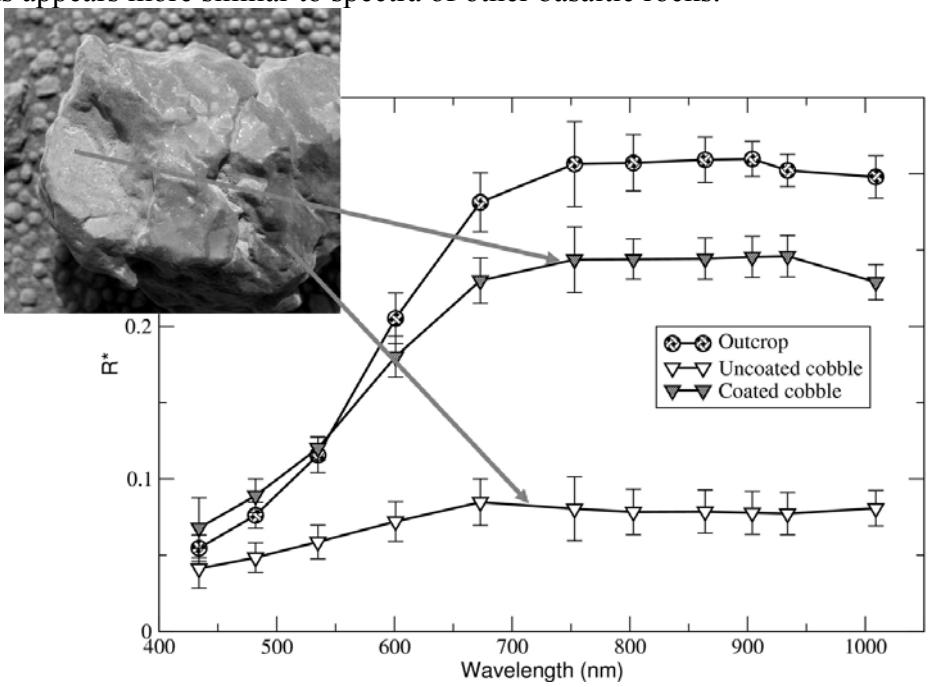

Figure 13.34. (*a*) Pancam false-color image (sol 352, P2596) of Heat Shield rock created from 753 nm, 535 nm and 432 nm images. White box outlines region of Microscopic Imager mosaic acquired after RAT brush (sol 349), shown in (*b*) with color overlain from the same Pancam false-color images as in (a). (Bright streaks are caused by saturation in MI mosaic.) Colored regions in (*a*) are regions of interest from which Pancam spectra were extracted as shown in (*c*). Canyon Diablo laboratory spectrum (RELAB MI-CMP-008, spectrum 001) is vertically offset -0.1.

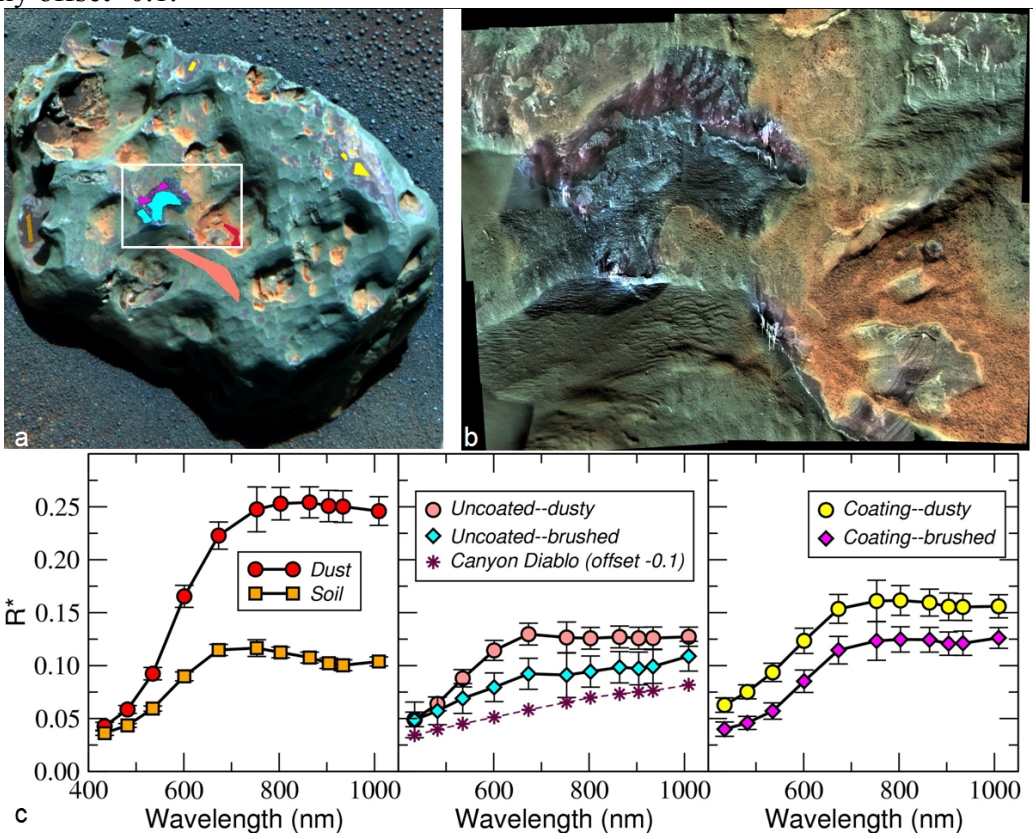

Figure 13.35. Pancam images sampling a range of representative soil morphologies at Meridiani Planum. (a) Sol 20 sequence P2564 natural color view of "clean" and "dusty" blueberries, clasts, outcrop fragments, and soil in the rover's work volume. Field of view is ~34 cm; (b) Sol 26 sequence P2385 false color image of trench in Eagle crater. Field of view is ~65 cm; (c) Sol 54 sequence P2540 false color view of sandy ripples and aeolian dust near the center of Eagle crater. Field of view is ~54 cm; (d) Sol 61 sequence P2559 false color view of dust, sand, and blueberries within the bright wind streak on the rim of Eagle crater. Field of view is ~59 cm; (e) Sol 73 sequence P2589 false color view of ripple crests (covered with very small berries) and troughs (scattered with larger berries) on the plains between Eagle and Endurance craters. Field of view is ~52 cm; (f) Sol 81 sequence P2422 false color view of sandy drift and outcrop deposits within a rift/crack in the plains between Eagle and Endurance craters. Field of view is ~192 cm; (g) Sol 211 sequence P2424 false color view of sand dune field in the center of Endurance crater. For scale, the dune field is about 50 m wide; (h) Sol 237 sequence P2588 false color view of dark sand drift next to outcrop blocks within Endurance crater. Field of view is ~58 cm; (i) Sol 414 sequence P2583 false color view of cobble-rich, berry-poor surface in the plains north of Viking crater. Field of view is ~45 cm; (j) Part of sols 456-464 sequences P2260 to P2270 natural color mosaic of plains ripples from "Purgatory" near the darker/lighter plains boundary north of Erebus crater. The wheel treads are ~120 cm apart; (k) Sol 749 sequence P2546 false color view showing air fall dust lingering in the lees of plains ripples just inside the rim of Erebus crater. Field of view is ~210 cm; (l) Sol 798 sequence P2393 false color view of banded ripple structure in the brighter plains materials northwest of Victoria crater. Field of view is ~3 m. See also Figures 29, 31, 32, 36, and 39 for additional morphologic examples of fine-grained materials at Meridiani.

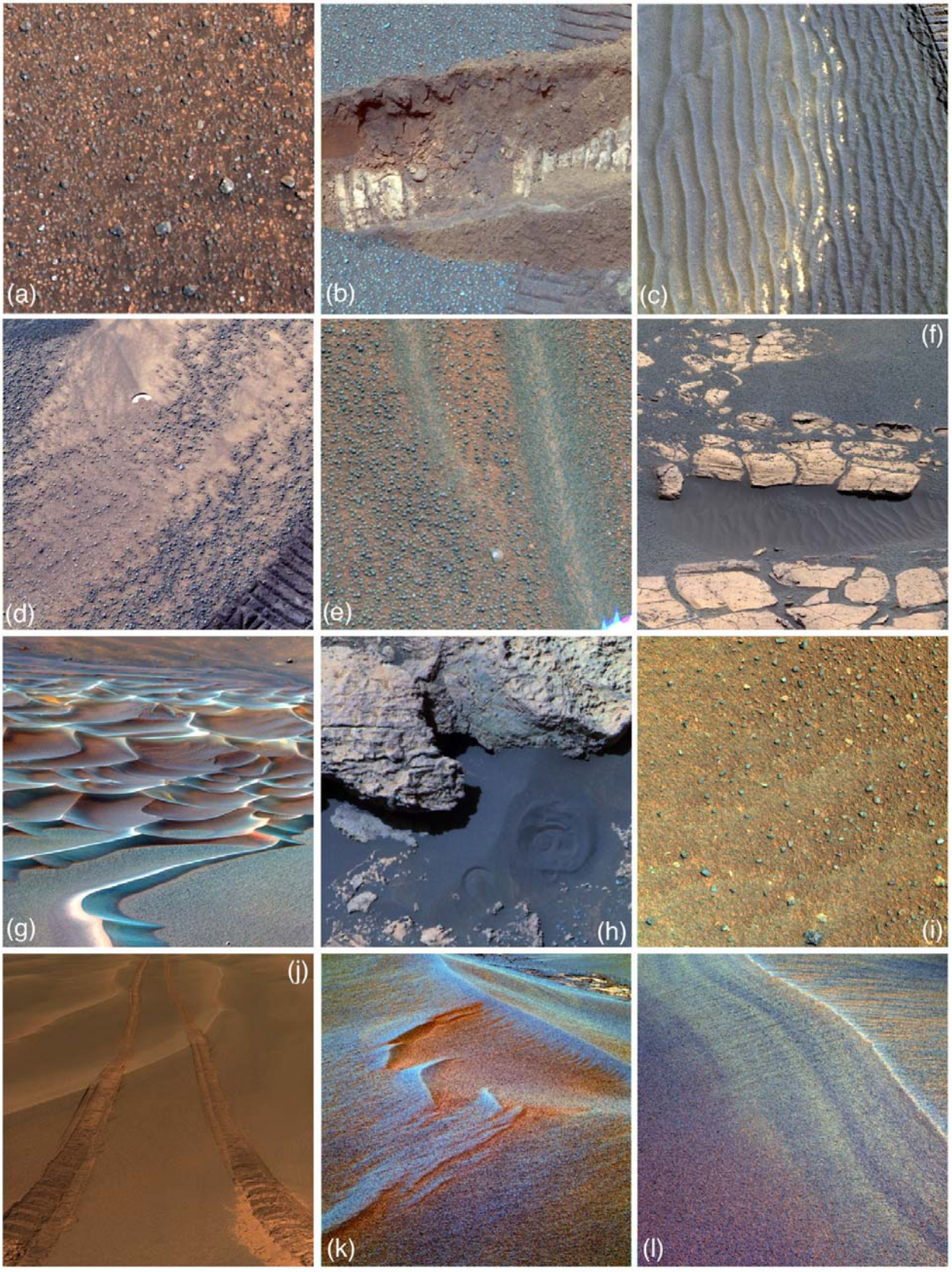
(a)
(b)
(c)
(d)
(e)
(f)
(g)
(h)
(i)
(j)
(k)
(l)

Figure 13.36. Target Panama Canal taken on sol 727. MI image 1M192737103 merged with Pancam sol 729 P2532 R271. The spherules are generally smaller in size than those seen further to north and in Eagle and Endurance craters. The largest blue grains are more irregular and less rounded in shape compared to typical spherules. The yellow elongate grain near the center of the image is likely a piece of outcrop. Image is 3.2 cm across.

Figure 13.37. Average Pancam spectra from bright (dusty) and dark (sandy) regions in Gusev crater and Meridiani Planum. Modified from Yen *et al.* (2005).

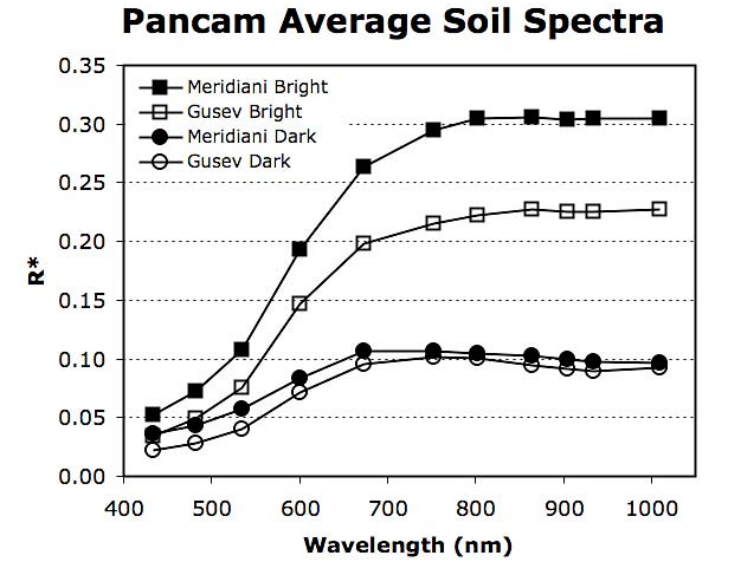

Figure 13.38. Mini-TES signatures of "buff" and "purple" outcrop that show increased hematite in Pancam spectral observations. Upper curves, El Capitan and Bellemont Purple show increased hematite band strength at 550 and 450 cm^{-1}, lower curves, Upper Wellington and Bellemont Buff do not show hematite. The solid line is the signature of hematite seen by TES in orbit.

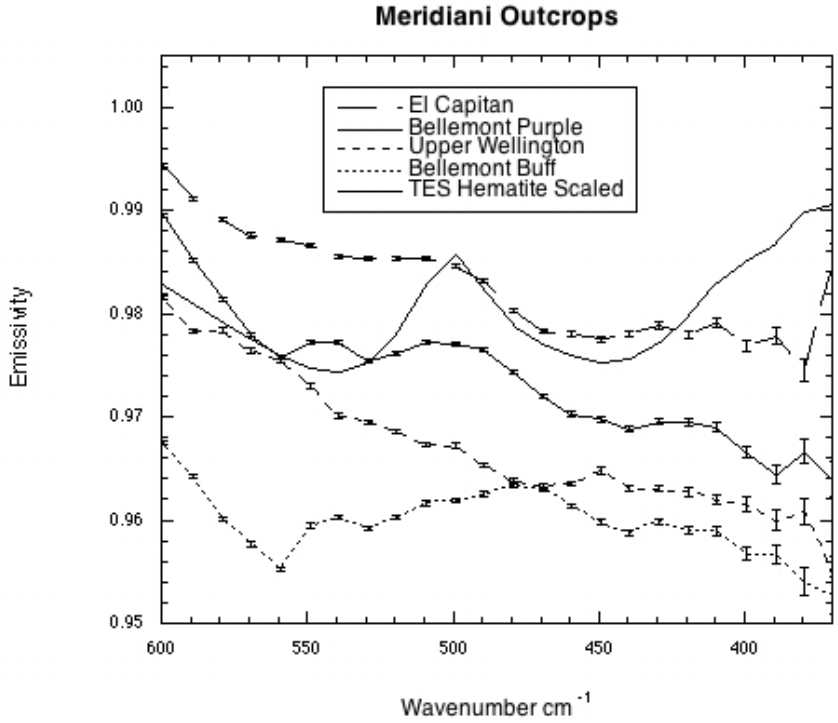

Figure 13.39. (a) Example Pancam images of high (left) and low (right) spherule cover. Left image is from Sol 795 (1P198759080IOF6900P2577) and right is from Sol 797 (1P198936159IOF6912P2578) and in both cases the image is an RGB composite of bands L2 (753nm), L5 (535nm), and L7 (432nm). **(b)** Example Mini-TES spectra showing high and low hematite index. The weaker index (dot-dash line) is from Sol 103 (1T137330168EMR2121P3716N0A1.QUB), the stronger (solid line) is from Sol 82 (1T135460592EMR1100P3715N0A1.QUB). The index is derived using a continuum near 750 cm^{-1} and band depth near 550 cm^{-1}, as illustrated by the horizontal lines. Vertical lines show the region obscured by atmospheric CO_2 absorption.

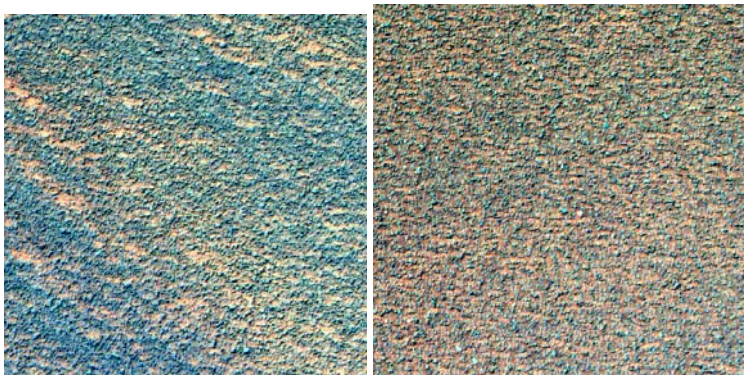

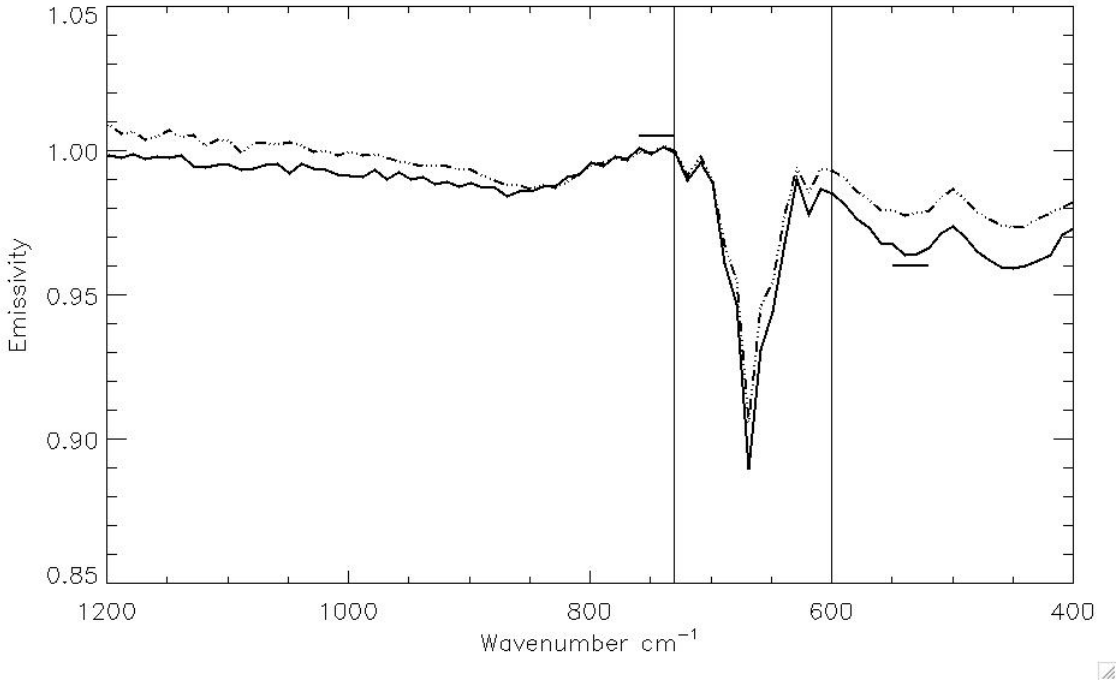

Figure 13.40. Pancam berry cover and Mini-TES hematite index with Sol.